ELECTRICAL CONDUCTION AND MAGNETORESISTANCE OF SILVER-STANNIC OXIDE COMPOSITE NANOTUBES

A Dissertation

by

ISABEL SCHULTZ

Submitted to the Office of Graduate and Professional Studies of
Texas A&M University
in partial fulfillment of the requirements for the degree of

DOCTOR OF PHILOSOPHY

Chair of Committee,	Wenhao Wu
Committee Members,	Philip Hemmer
	Winfried Teizer
	Joseph Ross
Head of Department,	George Welch

December 2015

Major Subject: Applied Physics

ABSTRACT

Mesoscopic materials typically have different properties compared to bulk materials because their dimensions can be smaller than certain characteristic lengths. Transport measurements on mesoscopic-sized disordered materials allow us to study quantum corrections to conductivity. In this study, silver-stannic oxide composite nanotubes of different diameters and lengths have been fabricated. Their resistances have been measured from 300 K down to 1.8 K in magnetic fields up to 5 T, applied either parallel or perpendicular to the nanotube axis. At temperatures below 10 K, the resistance has a linear dependence on the natural logarithm of temperature. Applying a range of magnetic fields both parallel and perpendicular to the nanotube axis results in an isotropic and positive magnetoresistance. An analysis of the data rules out weak localization as the dominant conduction mechanism, and it supports the existence of strong electron-electron interactions as the dominant conduction mechanism at low temperatures. Hopping transport mechanisms have also been considered, but they result in unrealistic physical parameters.

DEDICATION

Soli Deo Gloria

Glory to God alone

ACKNOWLEDGEMENTS

First and foremost, I would like to thank God for the amazing opportunity to be able to attend graduate school and complete my degree. I want to thank God for giving me the strength to keep going when I felt like giving up. There is no way I would have made it without His help and guidance. May everything I do bring Him honor and glory.

Secondly, I would like to thank my husband, Jesse, for his unfailing support, constant encouragement and unconditional love. Thank you for keeping me sane during the stressful times. Your optimism always shines brightly!

I would also like to thank my parents for teaching me about what was really important in life, and to all my family for their continued prayers. Your prayers always came at just the right time and helped to lift my spirits during the tough times. I really was blessed with the most amazing family in the world. I love you all. A special thanks to my sister Becky, just for being herself. Thank you for always being there for me.

Thank you to all my committee members for taking the time to meet with me and offering invaluable insight and advice. Thank you for serving on my committee and helping me through the process. Thank you to my committee chair, Dr. Wenhao Wu for his financial support and guidance.

Lastly, thank you to the administrators of the fellowships I was awarded, specifically the Diversity Fellowship, GAANN Fellowship, and IGERT Fellowship.

NOMENCLATURE

EBL	Electron Beam Lithography
EDS	Energy Dispersive X-ray Spectroscopy
FIB	Focused Ion Beam
PPMS	Physical Property Measurement System
RRR	Residual Resistance Ratio
SEM	Scanning Electron Microscope
TEM	Transmission Electron Microscope

TABLE OF CONTENTS

Page

LIST OF FIGURES

FIGURE Page

1. INTRODUCTION

1.1. Electrical Conduction

1.1.1 Electric Current

In general, electric current is the movement of charges form one region to another. Metals contain free electrons which are able to move within the conducting material, but cannot escape due to their attraction to the positive ions which make up the material. Although the free electrons move at great speed, their motion is completely random, and since there is no net flow of charge in any direction, no current is present.

If, however, an electric field $\boldsymbol{E}$ is established within the conductor then the free electrons feel a force given by[1]

$$\boldsymbol{F} = q\boldsymbol{E}. \tag{1}$$

Although frequent collisions do occur with the ions that make up the material, a net motion of charge also occurs in the direction of the electric force. This slow drift of charged particles is known as the drift velocity $\boldsymbol{v}_d$ and results in a net current within the conductor.

By definition, current is the net charge dQ which flows through an area A during a time dt. During this time particles with velocity $\boldsymbol{v}_d$ will move a distance $\boldsymbol{v}_d dt$. If the conductor has a cylindrical shape with cross sectional area A, and a concentration of particles n, then the volume of the cylinder is $A\boldsymbol{v}_d dt$, and the number of particles within it is $nA\boldsymbol{v}_d dt$. If each particle has charge q, the current is

$$I = n|q|v_d A, \tag{2}$$

and the current density, which is current per unit cross-sectional area,[1] is

$$J = n|q|v_d. \tag{3}$$

1.1.2 Resistance and Ohm's Law

If a potential difference is maintained across the conductor, an electric field and current density are established in the conductor. In the limit of a small electric field the current density is proportional to the electric field.[1] The proportionality constant σ is the conductivity of the conductor and the equation known as Ohm's Law is written as[1]

$$\boldsymbol{J} = \sigma \boldsymbol{E}. \tag{4}$$

We now consider the conductor to be a cylindrical wire with cross-sectional area A and length l, and maintain a potential difference of

$$\Delta V = V_b - V_a \tag{5}$$

across it. Using the definition of potential difference

$$V_b - V_a = -\int_a^b \boldsymbol{E} \cdot d\boldsymbol{s} = E \int_0^l dx = El, \tag{6}$$

we can now rewrite the current density as

$$J = \sigma E = \sigma \frac{\Delta V}{l}. \tag{7}$$

If we replace the current density with the current per unit cross-sectional area then we have

$$\frac{I}{A} = \sigma \frac{\Delta V}{l}, \tag{8}$$

which we can rewrite as

$$\Delta V = \left(\frac{l}{\sigma A}\right) I. \tag{9}$$

The resistance R of the conductor is equal to the quantity

$$R = \left(\frac{l}{\sigma A}\right), \tag{10}$$

and is defined as the ratio of the potential difference across a conductor to the current through the conductor,

$$R = \frac{\Delta V}{I}. \tag{11}$$

Since the resistivity ρ of a material is the inverse of its conductivity,[1]

$$\rho = \frac{1}{\sigma}, \tag{12}$$

then for a uniform block of material

$$R = \rho \frac{l}{A}, \tag{13}$$

The equation shows that the resistance of a sample depends on the geometry of the sample as well as on its resistivity. All materials that follow Ohm's Law have a characteristic resistivity that depends on the properties of the material and on temperature. Plotting current versus potential difference for ohmic materials results in a straight line with slope $1/R$.

1.1.3 Drude Model of Electrical Conduction in Metals

Paul Drude introduced a classical model of electrical conduction in metals. The Drude model is valuable because it introduces concepts that are applicable in more elaborate situations, but it does have limitations. Charges in an electric field feel a force given by

$$F = qE, \tag{14}$$

and Newton's second law says

$$F = ma, \tag{15}$$

so we can now write

$$a = \frac{qE}{m}. \tag{16}$$

A particle's mean free path l is the average distance traveled between collisions. The average velocity of the particle is given by the drift velocity v_d. The average time between collisions is given by τ. Assuming that the drift velocity is lost following each collision event, each collision event results in an acceleration of

$$a = -\frac{v_d}{\tau}. \tag{17}$$

In a steady-state,

$$\frac{qE}{m} - \frac{v_d}{\tau} = 0. \tag{18}$$

Therefore, we have

$$v_d = \frac{qE}{m}\tau. \tag{19}$$

Plugging into

$$J = nqv_d, \tag{20}$$

we get

$$J = nq\left(\frac{q\boldsymbol{E}}{m}\tau\right) = \frac{nq^2E}{m}\tau. \tag{21}$$

Lastly, since[1]

$$J = \sigma E \tag{22}$$

we can write

$$\sigma = \frac{nq^2\tau}{m}, \tag{23}$$

which is known as the Drude model of conductivity.

1.1.4 Electrical Resistivity of Metals

For a pure metal that has no defects, its resistivity, known as its intrinsic resistivity (ρ_i), is the result of the charge carriers (electrons or holes) colliding with the phonon vibrations and with each other.[2] According to the Bloch-Gruneisen formula[3,4], as the temperature goes down to 0 K, the resistivity also approaches zero as some power law of T. The Bloch-Gruneisen formula provides the theoretical expression for the intrinsic resistivity of a metal due to electron-phonon interactions and is given by[4]

$$\rho_i(T) = \alpha_{el-ph}\left(\frac{T}{\theta}\right)^5 \int_0^{\theta/T} \frac{x^5}{(e^x-1)(1-e^{-x})}\,dx, \tag{24}$$

where α_{el-ph} is the electron-phonon coupling parameter, and θ is the Debye temperature. In the limit that $T \to 0$, $\rho_i(T) \propto T^5$. In the limit that $T \to \infty$, $\rho_i(T) \propto T$.

If there are any impurities present, the impurities will also scatter the charge carriers, resulting in an increased resistivity.[2] Each different type of impurity will make independent contributions to the resistivity which are proportional to the concentration c of that type of impurity.[2] The residual resistivity ρ_0 is the resistivity at 0 K due to impurities.[2] Assuming that the resistivity due to impurities does not depend on temperature and is additive, then we can write

$$\rho = \rho_0(c) + \rho_i(T), \tag{25}$$

which is known as the Matthiessen Rule.[2] As the temperature approaches zero, the phonon vibrations freeze out. The residual resistivity of the sample at low temperature provides a good indicator of the level of impurity in the sample. We can calculate the residual resistance ratio (RRR), $RRR = \rho_{300\,K}/\rho_{1.8\,K} = R_{300\,K}/R_{1.8\,K}$,

$$RRR = \frac{\rho_{300\,K}}{\rho_{1.8\,K}} = \frac{[\rho_0(c) + \rho_i(T)]}{\rho_0(c)} = 1 + \frac{\rho_i(T)}{\rho_0(c)}, \tag{26}$$

and use it as a good indicator of the level of impurity in the sample.

1.2. Quantum Corrections to Conductivity

The theory of metals begins with the Bloch theorem which discusses the behavior of electrons in an ideal periodic lattice.[5] What happens for deviations in periodicity? Anytime interference due to electrons being scattered by impurities or phonons occurs quantum corrections to conductivity are introduced.[6] It is important to note that there are two types of scattering events. The elastic mean free path is the average distance an electron travels between two elastic collisions.[7] Elastic collisions occur at surfaces, dislocations, or impurity atoms, which are all lattice defects.[7] During elastic collisions, an electron preserves its energy[8] and the phase of the wave function is simply shifted by a fixed amount.[9] The average time between elastic collisions is τ and the elastic mean free path is given by $l = v_F\tau$, where v_F is the Fermi velocity.[10] The second type of collisions is inelastic scatterings. The inelastic mean free path is the average distance an electron travels between two inelastic collisions.[7] Inelastic collisions are dominated by the electron-phonon interactions, but also include electron-electron interactions.[7] Inelastic collisions cause the electron to change its energy[8] and lose its phase memory.[9] The average time[8] between inelastic collisions is τ_φ, and the inelastic mean free path[10] is given by $l_{in} = v_F\tau_\varphi$. The materials in which the highest frequency collisions are elastic scattering events ($\tau_\varphi \gg \tau$) are sometimes referred to as disordered or dirty metals.[8,11] Basically, the increased disorder results in conduction pathways that diminish the charge transport.

1.2.1 Weak Localization

In disordered metals, we can treat the motion of electrons semi-classically due to their diffusive motion.[9] Electrons travel as nearly plane waves and collide elastically with the randomly located impurities resulting in a random walk among the impurity sites.[9] As in Figure 1, we can consider all the possible trajectories that form a closed loop starting and ending at the same position designated $r = 0$. Weak localization arises from the self-intersecting paths in which electrons travel around the closed loop in opposite directions. In classical physics, the probability of a particle being found at its starting position is simply the sum of the probabilities[12] of its arrival along these two different paths $|A_1|^2 + |A_2|^2 = 2A^2$.

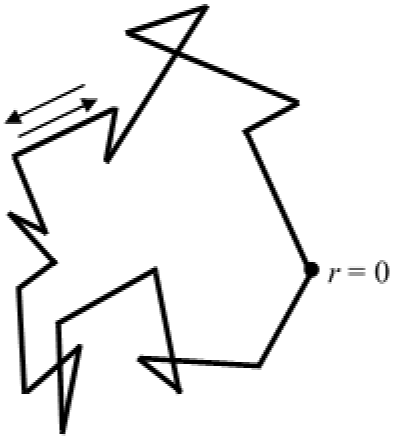

Figure 1. Closed loop of self-intersecting path and its time-reversal path leading to weak localization.

In quantum mechanics the probability of finding the electron at the position $r = 0$ is twice as large as the classical case. Here the probability of finding the particle[12] at the starting position is the sum of the amplitudes squared[13] and is given by $|A_1 + A_2|^2 = |A_1|^2 + |A_2|^2 + 2|A_1||A_2| = 4A^2$. Since the probability of finding an electron at the point $r = 0$ is higher, the electron spends more time at that point which is what leads to the corrections to conductivity.[8]

It is important to remember that in order for an electron to participate in interference it must return to the starting point before it loses its phase memory.[8] The phase coherence length is defined as the distance a particle travels before losing its phase memory. The phase coherence length and inelastic mean free path are sometimes thought to be interchangeable, but they are not.[10] That is because there are some scattering events which are considered to be elastic and phase-breaking at the same time, such as spin-flip scatterings.[14] The phase coherence length is given by[15]

$$L_\varphi = \sqrt{D\tau_\varphi}\,, \tag{27}$$

where D is the diffusion coefficient given by

$$D = v_F^2\tau/d. \tag{28}$$

The variable d is equal to the dimension of the sample (1, 2, or 3).[10] The time between inelastic scatterings, τ_φ, increases with decreasing temperature. Therefore, the conductivity decreases (resistivity increases) as the temperature decreases.[8] We know $\tau_\varphi \sim T^{-p}$, where p is a value on the order of 1 and depends on the scattering mechanism and dimensionality.[15] Also, as the dimension of the sample increases, the interference effect becomes weaker.[8]

The corrections to the conductivity were introduced by Anderson et al.[6] and Gorkov[16] et al. in 1979. In three dimensions the change in conductivity of a sample due to weak localization is given by[8]

$$\Delta\sigma_3 \approx -constant + \left(\frac{e^2}{\hbar}\right) L_\varphi^{-1}. \tag{29}$$

In two dimensions the change in conductivity of a sample due to weak localization is given by[8]

$$\Delta\sigma_2 \approx -\left(\frac{e^2}{\hbar}\right)\ln\left(\frac{\tau_\varphi}{\tau}\right) \approx -2\left(\frac{e^2}{\hbar}\right)\ln\left(\frac{L_\varphi}{l}\right). \quad (30)$$

In one dimension the change in conductivity of a sample due to weak localization is given by[8]

$$\Delta\sigma_1 \approx -\left(\frac{e^2}{\hbar}\right)L_\varphi. \quad (31)$$

The scale, $e^2/\hbar$, where e is electron charge and $\hbar$ is the reduced Planck constant, shows up in all the corrections to conductivity.[8] After the theory was developed, several research groups[17] began to study the resistance as a function of temperature in thin disordered films, and their experimental results seemed to serve as experimental proof of weak localization. However, some of those results were later attributed to electron-electron interaction which we will discuss next.[18]

Figure 2 shows the resistance versus temperature results of amorphous indium oxide thin films by Ovadyahu and Imry.[19] These thin films are considered to be two-dimensional and they display the linear relationship between the resistance and the logarithm of the temperature.

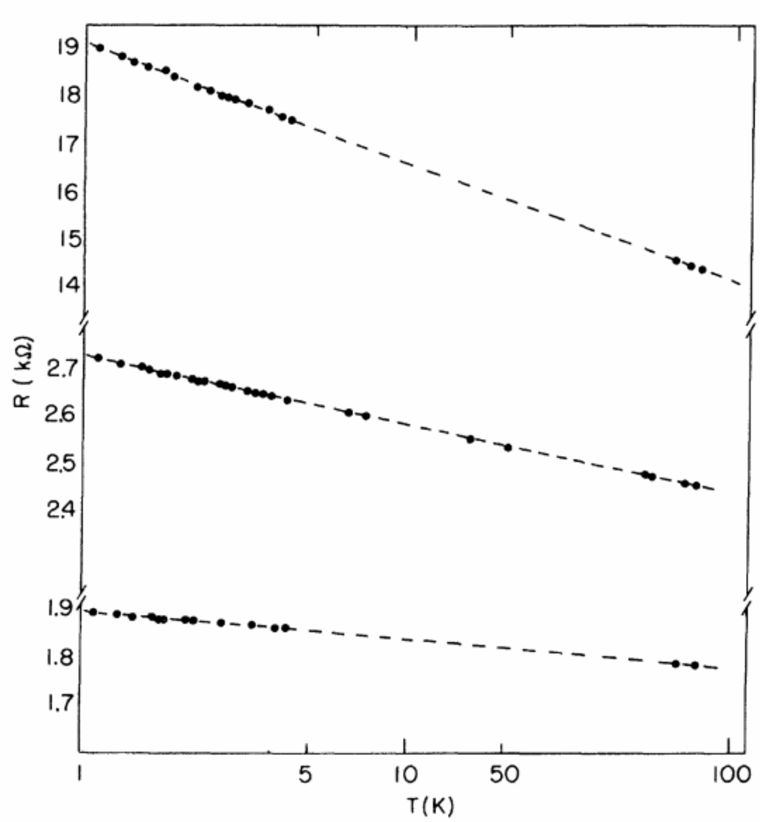

Figure 2. Resistance versus temperature plot for amorphous indium oxide films from Ovadyahu and Imry for three samples. R = 640 Ω (bottom), R = 1000 Ω (middle), and R = 4000 Ω (top).[19] (Used with permission Z. Ovadyahu and Y. Imry, Copyright © 1981, American Physical Society, http://dx.doi.org/10.1103/PhysRevB.24.7439)

1.2.2 Effect of Magnetic Field on Weak Localization

An electron traveling in a magnetic field experiences a force $\boldsymbol{F} = q\boldsymbol{v} \times \boldsymbol{B}$. This means that two electrons which are traveling towards each other will be deflected by the field in opposite directions. The cyclotron radius is r and the cyclotron frequency is given by $\omega = qB/m$. In dirty metals, τ is not that high so in a moderate field $\omega\tau \ll 1$ and we can ignore the difference between the scattering angles in comparison to the other more pronounced effects.[8] We know that in a magnetic field the momentum, $\boldsymbol{p}$, in the Hamiltonian-operator is replaced by $\boldsymbol{p} - e\boldsymbol{A}$, which takes into account the vector potential of the magnetic field.[20] Then the original wave function, when no magnetic field is present,

$$\Psi_0 \propto e^{\frac{i(\boldsymbol{p}\cdot\boldsymbol{r}-Et)}{\hbar}}, \tag{32}$$

must be modified to[20]

$$\Psi \propto e^{\frac{i\left((\boldsymbol{p}-e\boldsymbol{A})\cdot\boldsymbol{r}-Et\right)}{\hbar}} = e^{-i\left(\frac{e}{\hbar}\boldsymbol{A}\cdot\boldsymbol{r}\right)} e^{\frac{i(\boldsymbol{p}\cdot\boldsymbol{r}-Et)}{\hbar}} = \Psi_0 e^{-i\left(\frac{e}{\hbar}\boldsymbol{A}\cdot\boldsymbol{r}\right)}. \tag{33}$$

The term

$$e^{-i(\frac{e}{\hbar}\boldsymbol{A}\cdot\boldsymbol{r})} \tag{34}$$

illustrates that the electron wave function acquires a phase

$$\frac{e}{\hbar}\boldsymbol{A}\cdot\boldsymbol{r} \tag{35}$$

in the presence of a vector potential **A**.[20] As the electrons travel along a given path $\boldsymbol{l}$, this phase cumulates as

$$\frac{e}{\hbar}\int \boldsymbol{A}\cdot d\boldsymbol{l}, \tag{36}$$

so that[20]

$$\Psi \propto \Psi_0 e^{-i\left(\frac{e}{\hbar}\int \boldsymbol{A}\cdot d\boldsymbol{l}\right)}, \tag{37}$$

and it is easy to see that the old and new solution differs only by a phase factor. We also know that the magnetic flux, Φ_B, through a surface, $\boldsymbol{S}$, is

$$\Phi_B = \int \boldsymbol{B}\cdot d\boldsymbol{S} = BS, \tag{38}$$

when the plane of the loop and the direction of the magnetic field are perpendicular to each other. However, using Stokes' theorem, we know this is equivalent to

$$\Phi_B = \int \boldsymbol{B} \cdot d\boldsymbol{S} = \oint \boldsymbol{A} \cdot d\boldsymbol{l} \tag{39}$$

where $\boldsymbol{l}$, is the loop that bounds the surface $\boldsymbol{S}$. So now we can say

$$\Psi \propto \Psi_0 \exp\left(-i\frac{e}{\hbar}\Phi_B\right). \tag{40}$$

Then we can say

$$\Psi \propto \Psi_0 \exp(-i2\pi\Phi_B/\Phi_0), \tag{41}$$

where $\Phi_0 = h/e$ is the flux quantum.[21] The electron waves move along the loop in opposite directions, so when they get back to the origin, the two parts of the wave function have a phase difference[8] of $\varphi = 2\pi(\Phi_B/\Phi_0)$. This phase difference implies that the probability of finding a particle at $r = 0$, should now be considered to be[21] $|A_1 + A_2|^2 = |A_1|^2 + |A_2|^2 + 2|A_1||A_2|\cos\varphi = 2A^2(1 + \cos\varphi)$. Since the average value of $\cos\varphi = 0$, we know that the magnetic field destroys the interference.[8] Since the magnetic field suppresses the localization effect, the magnetoresistance turns out to be negative.[22] Figure 3 shows the magnetoresistance versus magnetic field for a silicon metal-oxide-semiconductor field effect transistor by Bishop et al.[23] From the figure we can see that the weak localization effect leads to a negative magnetoresistance.[24]

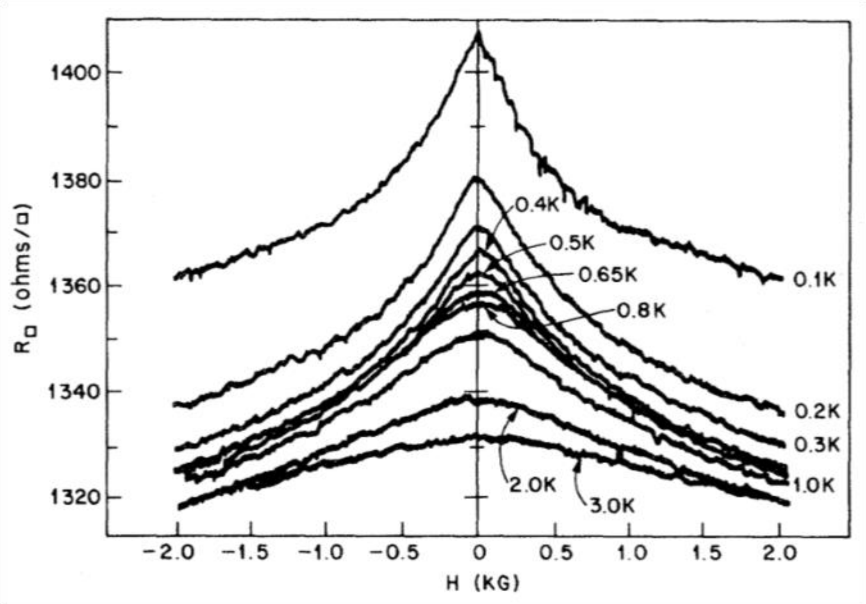

Figure 3. Magnetoresistance for a Si metal-oxide-semiconductor field effect transistor by Bishop et al. showing the destruction of weak localization due to a magnetic field.[23] (Used with permission D. J. Bishop, R. C. Dynes, and D. C. Tsui, Copyright © 1982, American Physical Society, http://dx.doi.org/10.1063/1.3475771)

1.2.3 Electron-Electron Interaction

At around the same time as the theory of weak localization was developed, Altshuler, Aronov, and Lee showed that there was another effect which also leads to an natural logarithm correction to the conductivity.[25] Although weak localization is due to self-intersecting paths, interference between wave functions of different electrons is also possible.[8] In a metal free from defects, two electrons that happened to be close together at time $t = 0$ move apart quickly[8] at the Fermi velocity v_F. This means that the distance between the two electrons would increase linearly[8] with time such that $r{\sim}v_F t$. Due to the diffusive motion of electrons in metals with defects however, the average distance between the electrons increases[8] at a much slower rate, $r{\sim}l(t/\tau)^{1/2}{\sim}v_F(t\tau)^{1/2}$. This means diffusion changes the conditions of electron interactions because it keeps the electrons close.[8]

In the diffusive regime, the electron-electron interactions lead to a dip in the density of states on the Fermi level.[26] When the electron-electron interactions are taken into account, a new characteristic length appears.[26] This new phase coherence length or the length of the interference region,

$$L_{ee} = \sqrt{\frac{D\hbar}{\varepsilon}} \sim \sqrt{\frac{D\hbar}{T}}, \tag{42}$$

determines the crossover to lower dimensions.[26] If the thickness of a thin film is less than L_{ee}, then it is considered to be 2-dimensional.[26] The variable ε represents the energy of the electron.

Unlike the weak localization case in which the inelastic collisions determine the phase coherence time, in electron-electron interaction the difference in the energies $\Delta\varepsilon$ is important.[8] The average difference in the energies of two electrons[27] is given by $\Delta\varepsilon \sim T$, where T is the temperature. For electron-electron interactions the phase coherence time[8] is approximately $\tau_{ee} \doteq \hbar/T$ following the uncertainty relation.

The correction to the conductivity due to electron-electron interactions in three dimensions is[8]

$$\Delta\sigma_3 \approx -constant + \left(\frac{e^2}{\hbar}\right)\tau_{ee}^{-1}. \tag{43}$$

In two dimensions, the change in conductivity of a sample due to electron-electron interactions is given by[8]

$$\Delta\sigma_2 \approx -\left(\frac{e^2}{\hbar}\right)\ln\left(\frac{\tau_{ee}}{\tau}\right) \approx -2\left(\frac{e^2}{\hbar}\right)\ln\left(\frac{L_{ee}}{l}\right). \tag{44}$$

In one dimension, the change in conductivity of a sample due to electron-electron interactions is given by[8]

$$\Delta\sigma_1 \approx -\left(\frac{e^2}{\hbar}\right)L_{ee}. \tag{45}$$

Since the corrections to the conductivity are similar for weak localization and electron-electron interactions, it would not be possible to distinguish between the two by analyzing the resistance versus temperature data alone. In order to distinguish between weak localization and electron-electron interaction we could analyze the magnetoresistance. In a magnetic field the spin up and spin down bands are split and each one has its own energy.[22] Basically, as the magnetic field is increased the electron spins want to align with the field. Due to the exclusion principle, however, there can only be one electron per state. As a result, the electron-electron interaction decreases the effective tunneling density of states.[8] The magnetoresistance for a thin film due to electron-electron interaction is isotropic and positive for spin splitting.[15,22] Unlike weak localization, the magnetoresistance due to electron-electron interactions is still evident at higher fields.[24]

1.3. Hopping Conductivity

1.3.1 Localized States

As described by Kramer and MacKinnon, localization is a property of the states in random quantum mechanical systems which shows up in the transport properties of condensed matter systems.[21] Localized states are defined as states whose wave functions are mainly concentrated in a confined region and decay exponentially outside this region. In other words, the envelope of the wave function decays exponentially away from the localization point.[15] In general

$$\psi \to f(r)e^{-r/\xi}, \tag{46}$$

where ξ is the localization length and is given by

$$\xi = \frac{\hbar}{\sqrt{2m|E|}}, \tag{47}$$

where E is the position of the electron level measured from the upper edge of the well.[8]

At finite temperatures, localized states will contribute to transport processes as carriers hop from occupied to free states.[8] An important assumption of hopping conductivity is that two states with equal energies would be infinitely far from each other.[8] To compensate for the differences in energy, hopping is accompanied by the emission or absorption of phonons.[21] The statistics of the excitations and the distribution of the localized states (both in energy and space) result in a unique temperature behavior of the transport coefficients.[21]

1.3.2 Nearest-Neighbor Hopping

Even if the electrons are all in localized states they can be excited by phonons so that they hop to other nearby localized states. Electrical conduction then occurs as a result of a series of hops. Hopping between nearest neighbors is the simplest form of hopping conductivity.[8]

In the nearest-neighbor hopping regime, the hopping probability can be written as

$$P_{hop} \sim \exp\left(-\frac{2r}{\xi} - \frac{\Delta E_{NNH}}{k_B T}\right), \tag{48}$$

where k_B is the Boltzmann's constant, ΔE_{NNH} is the energy separation between the final and initial states, T is the temperature, and r is the hopping distance.[28] From this equation, we can see that at relatively high temperatures the hopping conductivity is primarily determined by nearest-neighbor hopping. As the temperature decreases, the second term becomes larger and larger until eventually freezing out nearest-neighbor hopping. The resistivity as a function of temperature for nearest-neighbor hopping is given by[28]

$$\rho(T) = \rho_{NNH} \exp\left(\frac{\Delta E_{NNH}}{k_B T}\right). \tag{49}$$

In the equation above ρ_{NNH} is a temperature independent pre-exponential factor.

1.3.3 Mott Variable-Range Hopping

In order for nearest-neighbor hopping to occur there must be a localized state nearby that is empty. Decreasing the temperature makes nearest-neighbor hopping energetically unfavorable, as these states may have large energy separations. Therefore, at lower temperatures an electron is more likely to hop a longer distance in order to find an empty state that is closer in energy.[29] This then increases the importance of hopping between the centers with energies in the vicinity of the Fermi level where empty sites are known to exist.[8] Figure 4 shows a schematic diagram of the two hopping models, nearest-neighbor hopping and variable-range hopping. At higher temperatures, when phonons are readily available to provide the difference in energy, electrons can hop to a nearest-neighbor empty state. However, at lower temperatures, the phonons freeze out and electrons are more likely to hop a further distance in order to find an empty state that is closer in energy. In the figure below, the dashed line represents the Fermi energy.

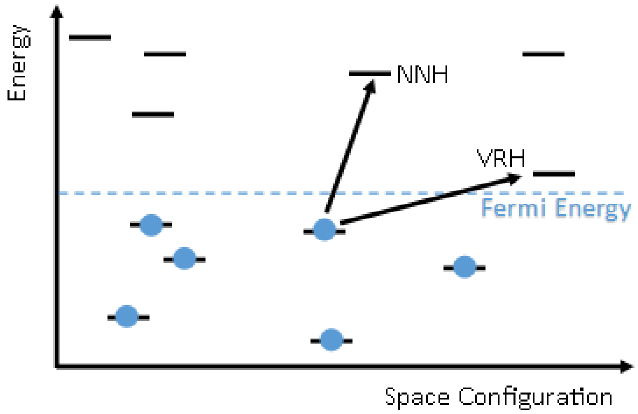

Figure 4. Schematic diagram showing both nearest-neighbor hopping (NNH) and variable-range hopping (VRH) models.

In 1968 N. F. Mott derived the temperature dependent resistivity due to variable-range hopping.[30] For 3-dimensional hopping, the average hopping distance for Mott variable-range hopping is given by[31]

$$\bar{R}_{Mott} = \frac{3}{8}\xi\left(\frac{T_{Mott}}{T}\right)^{1/4}. \tag{50}$$

As seen from this equation, the average hopping distance depends on the temperature and therefore as the temperature changes so does the average hopping length, hence the term variable-range hopping. The average hopping energy in 3-dimensional Mott variable-range hopping is given by[31]

$$\bar{\Delta}_{Mott} = \frac{1}{4}k_B T\left(\frac{T_{Mott}}{T}\right)^{1/4}, \tag{51}$$

where the characteristic temperature coefficient, T_{Mott} is given by[30]

$$T_{Mott} = \frac{18}{k_B N(\varepsilon)\xi^3}. \tag{52}$$

For Mott variable-range hopping, the temperature dependent resistivity follows the form

$$\rho(T) = \rho_{Mott}\exp\left[\left(\frac{T_{Mott}}{T}\right)^{\frac{1}{1+n}}\right], \tag{53}$$

where $n = 1, 2,$ or 3 refers to one, two, or three-dimensional variable-range hopping.[30] The variable ρ_{Mott} is a temperature independent pre-exponential factor.

Figure 5 shows the experimental results by Yildiz et al. showing the temperature dependence of the conductivity plotted as $\ln(\sigma)$ versus $T^{-1/4}$ for a titanium dioxide thin film.[32] The solid line in the figure corresponds to the three-dimensional Mott variable-range hopping line fit for their data.[32]

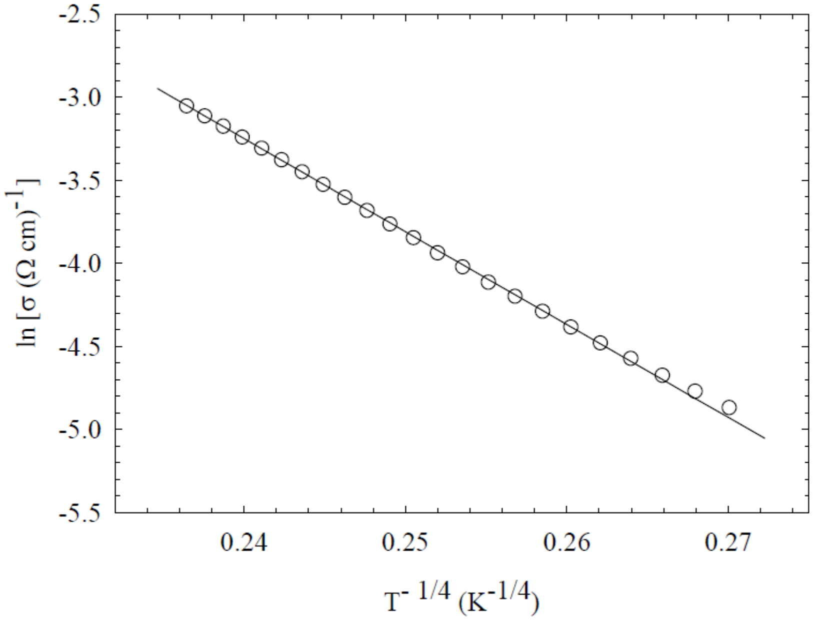

Figure 5. Yildiz et al. results[32] for a thin TiO_2 thin film showing the temperature dependence of the conductivity plotted as ln(σ) versus $T^{-1/4}$. (Used with permission A. Yildiz, S. B. Lisesivdin, M. Kasap, and D. Mardare, 2007)

1.3.4 Efros-Shklovskii Variable-Range Hopping

It is important to note that Mott variable-range hopping is only applicable when Coulomb interactions between the localized electrons are negligible. In 1970 M. Pollack pointed out that electron-electron interactions actually reduce the density of states near the Fermi energy.[33] A soft Coulomb gap opens up when long-range Coulomb interactions become significant.[33] In the presence of a Coulomb gap, the number of states in the vicinity of the Fermi level is no longer constant.[34] Figure 6 shows a schematic illustration of a Coulomb gap in the density of states near the Fermi level.

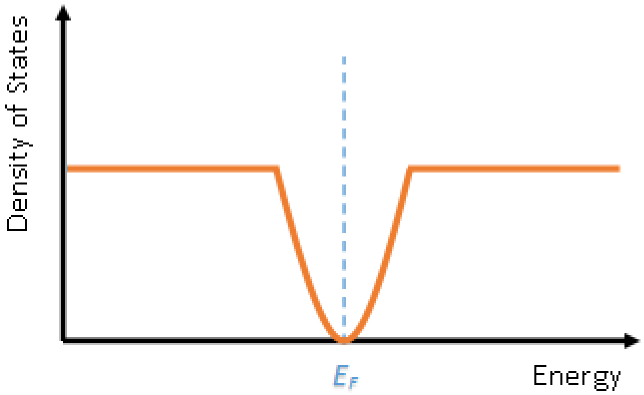

Figure 6. Schematic illustration of a Coulomb gap in the density of states.

In 1975 Efros and Shklovskii pointed out that at low enough temperatures, the density of states is not constant near the Fermi energy due to electron-electron interactions and proposed new conductivity equations.[35] The average hopping distance for 3-dimensional Efros-Shklovskii variable-range hopping is given by[31]

$$\bar{R}_{ES} = \frac{1}{4}\xi\left(\frac{T_{ES}}{T}\right)^{1/2}. \tag{54}$$

The average hopping energy for 3-dimensional Efros-Shklovskii hopping is given by[31]

$$\bar{\Delta}_{ES} = \frac{1}{2}k_B T\left(\frac{T_{ES}}{T}\right)^{1/2}, \tag{55}$$

and the characteristic temperature T_{ES} is given by[35]

$$T_{ES} = \frac{2.8e^2}{\kappa\xi k_B}, \tag{56}$$

where κ is the permittivity. The temperature dependent resistivity equation for Efros-Shklovskii hopping is given by

$$\rho(T) = \rho_{ES} \exp\left[\left(\frac{T_{ES}}{T}\right)^{\frac{3}{3+n}}\right], \tag{57}$$

where again $n = 1, 2,$ or 3 refers to one, two, or three-dimensional variable-range hopping.[36] Here ρ_{ES} is a temperature independent pre-exponential factor.

In 1991 Rosenbaum proposed a theoretical crossover temperature between Mott variable-range hopping and Efros-Shklovskii variable-range hopping.[37] Since then the crossover temperature has also been confirmed experimentally[38] on a number of occasions.[39] The crossover temperature from Mott variable-range hopping conduction to Efros-Shklovskii variable-range hopping conductivity occurs at the temperature[37]

$$T_{Crossover} = 16\,\frac{T_{ES}^2}{T_{Mott}}. \tag{58}$$

Figure 7 shows the resistivity as a function of temperature for three-dimensional Mott variable-range hopping and three-dimensional Efros-Shklovskii variable-range hopping from Viana et al.[36] The plot also points out the crossover temperature which occurs at 16 K in their SnO_2 nanobelt sample.[36]

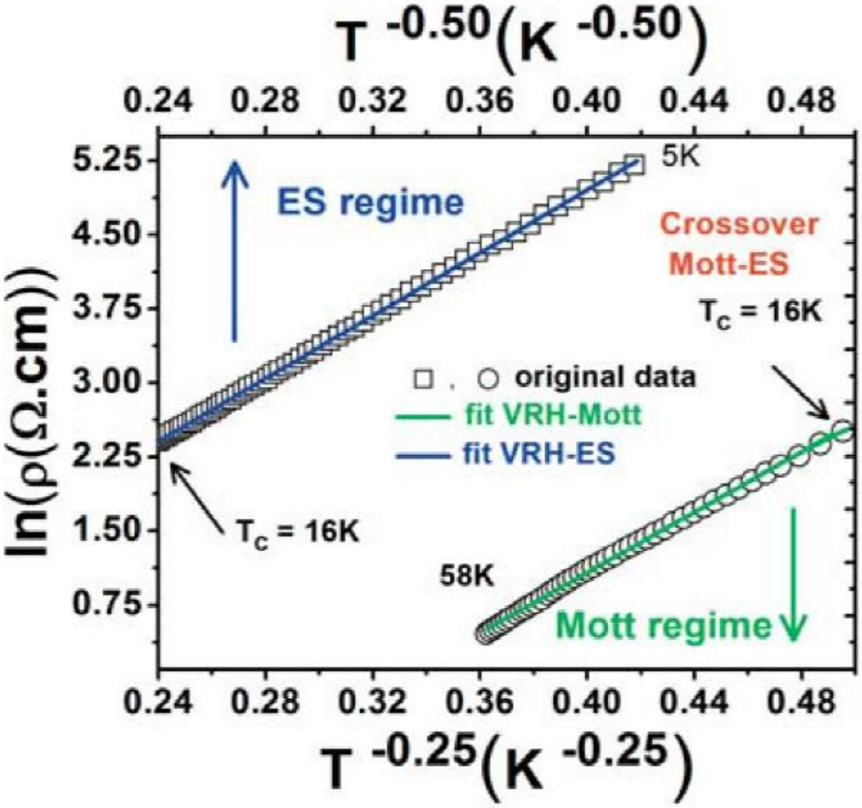

Figure 7. Results by Viana et al. for resistivity as a function of temperature for three-dimensional Mott variable-range hopping and three-dimensional Efros-Shklovskii variable-range hopping.[36] The crossover from Mott to Efros-Shklovskii variable-range hopping occurs at 16 K for the SnO_2 nanobelt sample.[36] (Used with permission E. R. Viana, J. C. Gonzalez, G. M. Ribeiro, and A. G. de Oliveira 2012)

1.4. Mesoscopic Materials

The electrical, magnetic, optical and mechanical properties of a solid can change if the dimensions of the solid become smaller than a critical length associated with the properties.[40] In general, making the dimensions of a solid comparable to the wavelength of an electron could affect the electrical, and magnetic properties of the solid.[40] The small dimensions could lead to electron confinement and quantized states, as well as giant magnetoresistance.[40] Extensive research has been done on the electrical and magnetoresistance properties of thin films, so nanowires and nanotubes are the next class of experimentally interesting materials. There are still quite a bit of difficulties present in trying to measure the transport properties of single nanowires and nanotubes, but experimental data is needed as we continue to try to understand the transport properties of mesoscopic materials. Since there are quite a few interesting transport behaviors that occur at low temperatures, my goal was to measure the electrical and magnetoresistance properties of disordered conducting nanotubes.

A granular or composite material is one that consists of grains or granules which are a mixture of metallic and insulating regions.[29] In composite materials, the variable x represents the fraction of the total volume occupied by metallic grains.[8] The electrical properties of composite materials depend on the composition. In the dielectric regime, electrical conduction has been found to occur as a result of hopping transport mechanisms in thin films.[41,42] Once the relative volume of the metal reaches a certain stage, conductivity is activated.[8,29] The system undergoes a metal-insulator transition once connected metallic pathways through the sample are established.[29] For composite thin films in the metallic regime, typical dirty metal behavior has been observed.[43]

Transport measurements on gold-aluminum oxide,[42] nickel-stannic oxide,[42] and silver-stannic oxide thin films have been previously analyzed.[43] As one of the newer contact materials for relays, silver-stannic oxide is of particular interest. As the dimensions of electrical components decrease, it is important to understand the electrical transport properties that result. My goal was to study the electrical conduction and magnetoresistance properties of silver-stannic oxide composite nanotubes.

2. SAMPLE FABRICATION

2.1. Nanotube Templates

In recent years, research groups have developed a significant number of template based nanotube and nanowire fabrication methods. The two main types of templates used are anodized aluminum oxide templates and track-etched polycarbonate templates. Anodized aluminum oxide templates are sometimes preferred due to a higher pore density when compared to polycarbonate templates. In other cases, polycarbonate templates are preferred due to their hydrophilic properties. In the cases where I needed polycarbonate templates, I simply used the commercially available ones. In my journey to try to fabricate long, ultrathin, conducting nanotubes I have in some cases used homemade anodized alumina templates, which offer greater pore ordering (honeycomb array) and smoother surfaces when compared to their commercially available counterparts.

Anodizing is an electrochemical process that forms an oxide layer on various metals. Using an electrolyte which is able to partially dissolve the oxide layer produces a porous oxide layer. In 1941, J. D. Edwards and F. Keller described the hexagonal pore structure of the anodized aluminum oxide coatings.[44] By 1953, F. Keller, M. S. Hunter and D. L. Robinson had described the structural features of various anodized aluminum oxide coatings.[45] They showed how changing the electrolyte and anodizing voltage affected the dimensions of the pores.[45] Therefore, a range of aluminum oxide template pore sizes is possible by changing the acid and/or the anodizing voltage. Some groups use multiple anodizing steps and low temperature to improve the ordering of pore structures.[46] To make an anodized aluminum oxide template like the one seen in Figure 8, I first electro-polished high purity aluminum sheets at 1 A for two minutes, using a 4:1 ethanol to perchloric acid solution, and a piece of platinum foil as the counter electrode.

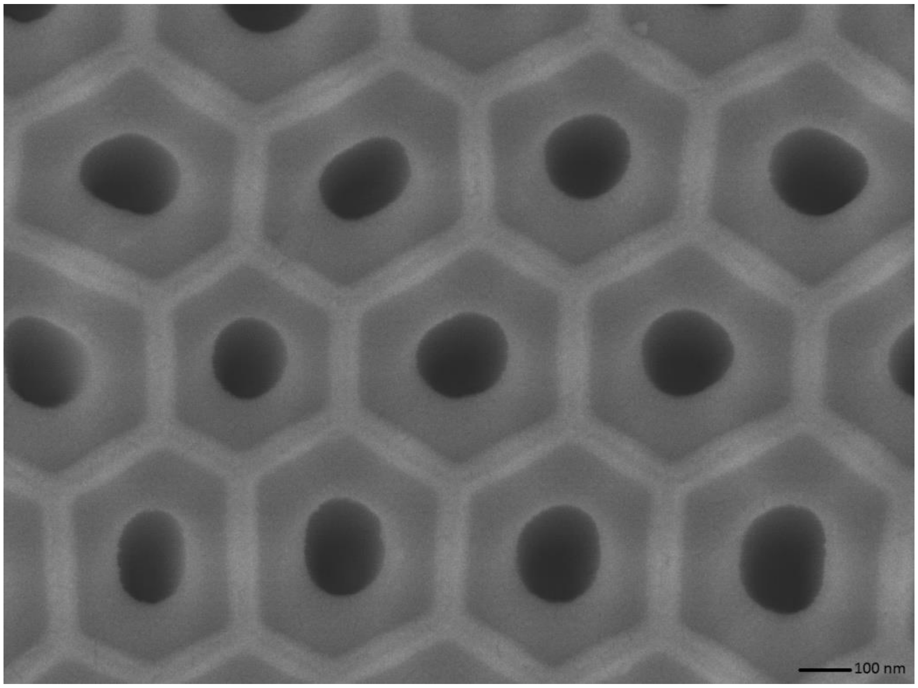

Figure 8. SEM micrograph which shows the bottom side of an anodized aluminum oxide template with approximately 190 nm pore diameter.

During the anodizing process, a direct current passes through an electrolytic solution where the aluminum sheet is the anode. Due to the current, hydrogen is released at the cathode (a piece of platinum foil in my case) and oxygen is released at the surface of the aluminum anode. The oxidation rate balances the dissolution of the aluminum oxide by the acidic solution, which results in a coating with microscopic pores. For the template showed in the figure, I used a 0.5 % H_3PO_4 electrolytic bath. For the first anodizing step, I slowly increased the voltage to 195 V and let the process continue for about 3 hours. Then I placed the anodized alumina into a 5 % H_3PO_4 solution at 60 ℃ until I completely etched away the first oxide layer. What is left is a piece of aluminum that has small indentations where the previous pores were grown. This helps increase the pore ordering for the second anodizing step. I performed the second anodizing step under the same growth conditions, but left it for a much longer time (typically 12 hours). A longer anodizing time results in longer pores. Once the second anodizing process was complete, I attached one side to a glass slide using crystal bond to protect that side. Then I removed the oppositely anodized side with the 5 % H_3PO_4 solution at 60 ℃ . I also removed the remaining aluminum layer using a PCB etchant. Lastly, I used the 5 % H_3PO_4 solution at 30 ℃ for about one hour to open the back side of the pores. The resulting templates have a pore diameter of about 190 nm. Since the other side of the pores was covered, no pore widening occurred on that side. Homemade aluminum oxide templates offer quite a few benefits when compared to the commercially available templates and are significantly more cost effective, but I do note that in some cases due to time constraints, I simply used commercially available aluminum oxide templates.

2.2. Nanotube Fabrication

There are also two main template deposition methods for nanotube and nanowire fabrication. These processes can produce crystalline or amorphous structures, depending on parameters such as deposition settings, temperature, and chemical bath concentrations. Although what I needed for my measurements was a silver-stannic oxide nanotube, as I attempted to learn more about the electroless and electroplating processes, I was able to fabricate successfully a variety of nanotubes, not all of which I will discuss here.

2.2.1 Titanium Dioxide Nanotubes

The first nanotubes I was able to make were titanium dioxide nanotubes, using the sol-gel method described by H. Imai, Y. Takei, K. Shimizu, M. Matsuda, and H. Hirashima in their *Journal of Materials Chemistry* publication,[47] using anodized aluminum oxide templates (Figure 9).

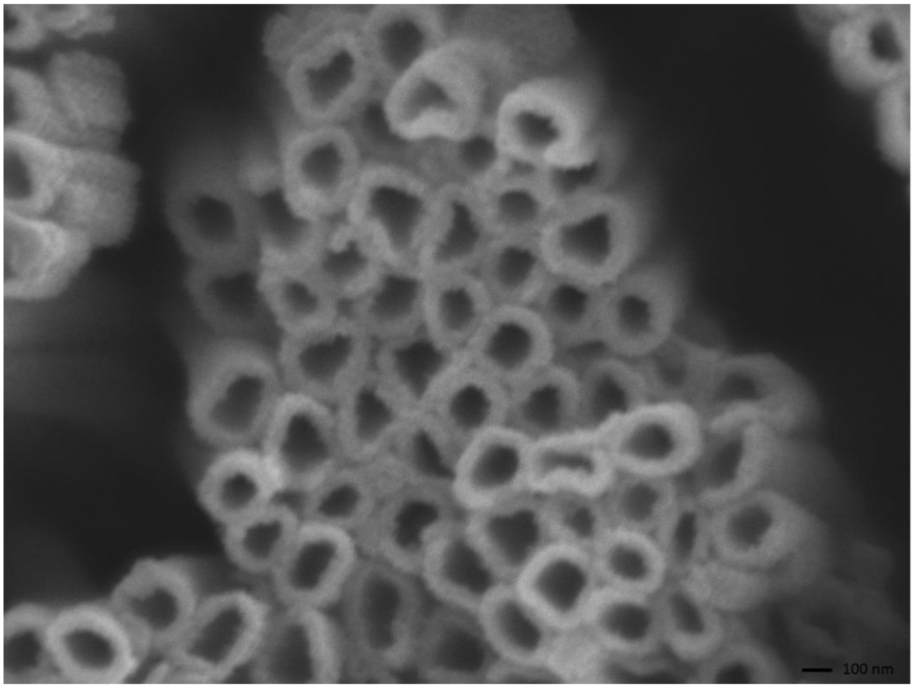

Figure 9. Two hundred nanometer diameter titanium dioxide nanotubes fabricated using a sol-gel method in anodized aluminum oxide templates.

This nanotube fabrication method is rather straightforward; I heated the 0.04 M TiF_4 solution to 60 ℃ and then immersed the anodized aluminum oxide templates (nominal pore size: 200 nm) in the solution for varying periods of time. Then I heated the template to 225 ℃ for 2 hours. To obtain the SEM micrograph, I attached the sample to a silicon wafer and used sodium hydroxide to dissolve partially the anodized aluminum oxide template. Figure 10 shows how increasing the deposition time uniformly increases the nanotube thickness. In those SEM micrographs, the titanium dioxide nanotubes are still in the anodized aluminum oxide template.

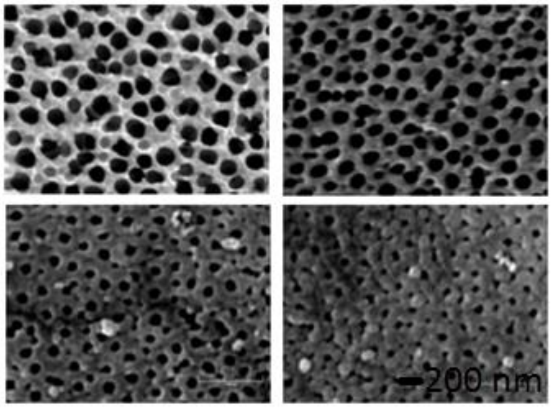

Figure 10. Titanium dioxide nanotubes in anodized aluminum oxide templates. Top left: empty template, no titanium dioxide. Top right: 1 minute deposition. Bottom left: 3 minute deposition. Bottom right: 5 minute deposition.

These nanotubes are worth mentioning due to their potential use in tuning the anodized aluminum oxide template parameters. During the anodizing process, the voltage determines the pore spacing and pore diameter of the template. Subsequent etching could enlarge the pore diameters, but otherwise, it is difficult to tune the pore spacing and diameter separately. Since an increase in deposition time leads to a uniform increase in wall thickness, titanium dioxide nanotubes could potentially be used to minimize the pore diameter without changing the pore spacing, in applications where specific pore spacing and diameters are required. To show this is a viable option, we were able to fill the titanium dioxide pores with cobalt nanowires, but I do not include those results here.

2.2.2 Gold Nanotubes

Next, I tried an electroplating technique similar to the one proposed by W. Lee, R. Scholz, K. Nielsch, and U. Gosele in which they suggest depositing silver nanoparticles on the anodized aluminum oxide template surfaces.[48] Their method is based on the preferential growth of a metal along the pore walls due to the presence of metallic nanoparticles.[48] In order to immobilize the silver nanoparticles on the pore surfaces, I first immersed the anodized aluminum oxide template (nominal pore size: 200 nm) into a tin solution containing 0.02 M $SnCl_2$ and 0.01 M HCl for 2 minutes. I rinsed the template with de-ionized water, then with acetone, and dried the template on a 70 ℃ hot plate for one minute. Next, I immersed the template into the 0.02 M $AgNO_3$ solution for two minutes. I again rinsed and dried the sample as before. One tin and one silver solution immersion made up one cycle, and I did 10 cycles. Even with ten cycles, the silver nanoparticles on the pore surface did not form a continuous layer. After the immobilization of silver nanoparticles in the pores, I sputtered a 10 nm, conductive, platinum/palladium layer on one template surface. Although the platinum/palladium layer was conductive, it was not thick enough to cover the back pore openings, and served as the cathode in the electro-deposition process. For the electro-deposition, the electrolyte was Auruna 5000, which is a commercially available gold plating solution, and I used a piece of platinum foil to serve as the anode. I electroplated at a current density of 3.4 mA/cm^2 for 30 minutes. Figure 11 shows my typical results. Each time, the sample started out as a nanotube, but after a short distance morphed into a nanowire.

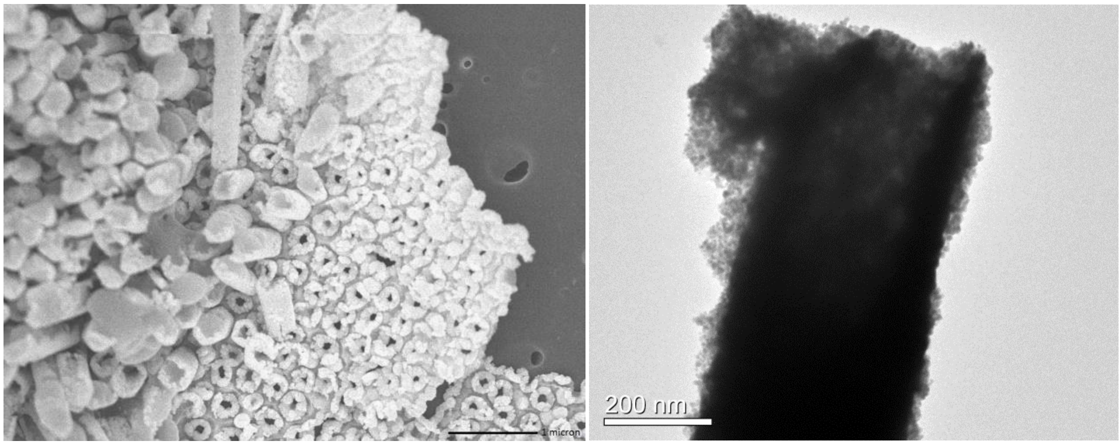

Figure 11. SEM micrograph (left) and TEM micrograph (right) which shows how they start out as nanotubes then morph into nanowires.

For the SEM micrograph, I attached the template to a silicon wafer and then partially dissolved the template using sodium hydroxide. For the TEM micrograph, I put the template into a sodium hydroxide solution until the template dissolved completely. Then I used a centrifuge and removed the sodium hydroxide solution from the nanotubes. I rinsed the nanotubes with de-ionized water three times and then put them in isopropyl alcohol to end up with a suspension of gold nanotubes in isopropyl alcohol.

2.2.3 Copper Nanotubes

To fabricate copper nanotubes I used a process like the one described by B. Bercu, I. Enculescu, and R. Spohr,[49] although I did make some minor modifications. Here I used an electroless deposition technique with polycarbonate membrane filters of nominal pore size 220 nm. These commercially available templates have a layer of poly(vinylpyrrolidone) added during production, which makes them hydrophilic. First, I sensitized the polycarbonate template by immersing the sample in a tin solution containing 0.02 M $SnCl_2$ and 0.01 M HCl for 6 minutes. As described by V. P. Menon and C. R. Martin,[50] the poly(vinylpyrrolidone) coating contains “metal-ion complexing amino and carbonyl groups” which serve as “molecular anchors that bond the Sn^{2+} to the surfaces of the template.” Then I rinsed the templates with de-ionized water and dried them. Next, I activated the Sn^{2+} surfaces using a palladium solution that consisted of 0.1 wt. % $PdCl_2$ and 1.0 wt. % HCl for 4 minutes. I then rinsed and dried the templates again. Then I placed the templates into a 200 ml copper deposition bath which contained 1 g $CuSO_4 \cdot 5H_2O$, 5 g potassium sodium L-tartate tetra-hydrate, 1.4 g NaOH, and 2 ml formaldehyde for 10 minutes at room temperature. I rinsed and dried the samples one last time. In order to analyze the copper templates, I attached the polycarbonate template to a piece of silicon wafer and then partially dissolved the template using dichloromethane. Figure 12 shows the results.

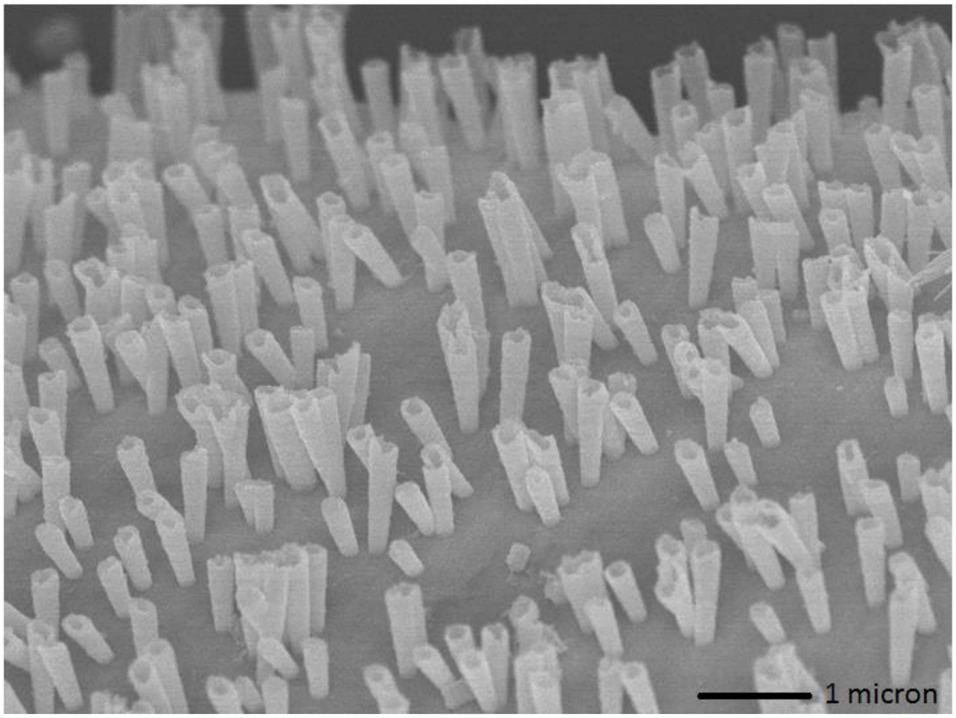

Figure 12. Copper nanotubes still in a partially dissolved polycarbonate template.

One of the problems in fabricating the copper nanotubes was due to the chemical reactions involved in making the final copper metal. This reaction produces quite a few bubbles at the surface. Because the pore diameters are in the 200 – 300 nm range, the bubbles expel the solution from the pores, which hinders the growth of copper within the pores.

2.2.4 Silver-Stannic Oxide Composite Nanotubes

Eventually I was able to obtain nanotubes of a measurable length (approximately 10-micron) using various components of different electroless deposition processes. For these nanotubes, I again used nominal pore size 220 nm polycarbonate templates, but slightly modified the sensitization and activation solutions from the copper method. This time the tin solution consisted of 10 g/l $SnCl_2$ and 10 ml/l HCl. I immersed the templates in the tin solution for 6 minutes and then rinsed with de-ionized water and dried them. The activation solution contained 0.1 g/l $PdCl_2$ and 10 ml/l HCl and I immersed the templates for 4 minutes then rinsed and dried them. I completed ten cycles of template sensitization and activation. After that, I placed the template in the silver solution for 45 minutes, resulting in a continuous layer. The silver solution consisted of two-parts, part A and part B. Part A included 2.3 g $AgNO_{3,}$ 1.9 ml NH_4OH, and 22.7 ml de-ionized water; while part B consisted of 10.68 g $KNaC_4H_4O_6 \cdot 4H_2O$, 0.57 g $MgSO_4$, and 18.2 ml de-ionized water. I mixed equal parts of part A and part B with 14.1 parts de-ionized water, and heated the solution to 35 ℃ before immersing the templates. Then I rinsed and dried the sample. Because this silver deposition process did not produce any bubbles, I was able to grow nanotubes that span the length of the template. Then I dissolved the template using dichloromethane. After I placed a drop of solution on the appropriate substrate, I rinsed the sample with methanol and water.

Some of the as prepared samples initially had a very high resistance so I annealed them at 200 ℃ for a few minutes. The annealing step was motivated by several factors. First of all, annealing is known to reduce disorder[51] and stabilize the resistance.[52] Secondly, silver is known to spontaneously oxidize[53] at temperatures below 195 ℃. The reaction[53] is stable at about 195 ℃ and reverses at temperatures above 195 ℃. Lastly, researchers have also found a decrease in the resistivity of stannic oxide films due to annealing.[54] The decrease in resistance when annealed to 200 °C is attributed to the formation of metal conducting chains of excess metal particles,[54] which is consistent with our results. I found that annealing the sample for as little as 2 minutes lowered and stabilized the resistance. Figure 13 shows a TEM micrograph of an annealed nanotube.

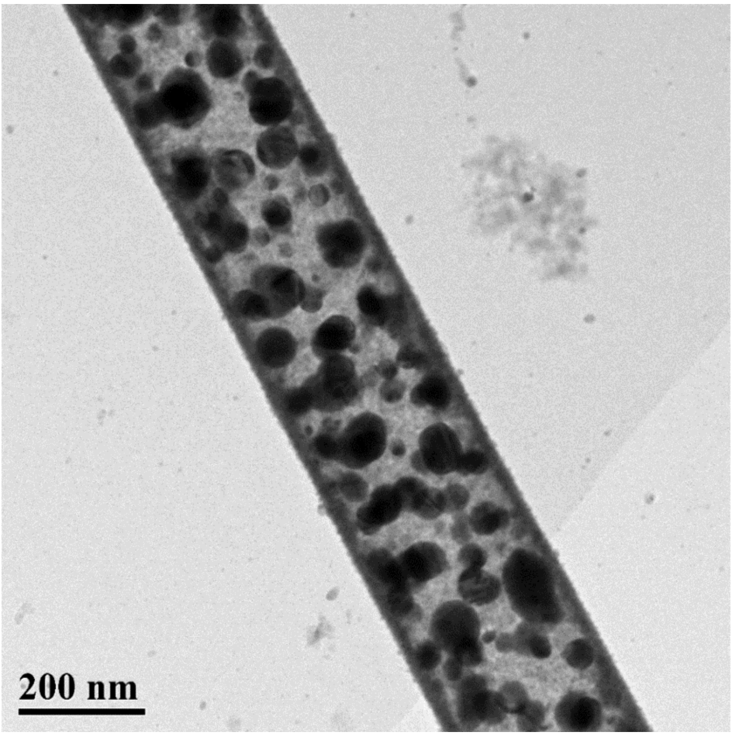

Figure 13. A TEM micrograph of a single silver-stannic oxide composite nanotube.

It is important to note that even though a commercially available polycarbonate template with a 220 nm nominal pore diameter was used, the nanotubes I obtained have an outer diameter ranging between 270 nm and 310 nm. This is due to the fact that these polycarbonate templates are actually membrane filters and even though one pore opening is close to 220 nm, the whole diameter of the pore is not entirely uniform. For the samples I chose for measurement, I specifically chose samples with a uniform diameter.

As a side note, in order to verify that the tin/palladium cycles did not form a continuous nanotube, I dissolved parts of the template prior to the silver deposition. All that was left each time were nanoparticles. I also did a two probe resistance measurement and got overload each time indicating that the particles were not conducting. After the silver deposition, the two probe measurements resulted in finite values.

2.3. Sample Contacts

2.3.1 Four-Point Probe

For all my resistance measurements, I employed a four-point probe contact method. A four-point probe is more accurate than the traditional two-probe measurement because it gets rid of the contact resistances and the impedance contribution of the wiring. The four-point probe measurement technique uses separate leads for current carrying and voltage sensing. Figure 14 shows a schematic diagram of the four-point probe setup. The outermost leads supply the current. This current generates a voltage drop across the nanotube, but also across the I_+ and I_- wires themselves. The measured resistance is between the two inner leads labeled V_+ and V_-

respectively. The technique’s accuracy is because almost no current flows through the inner leads.

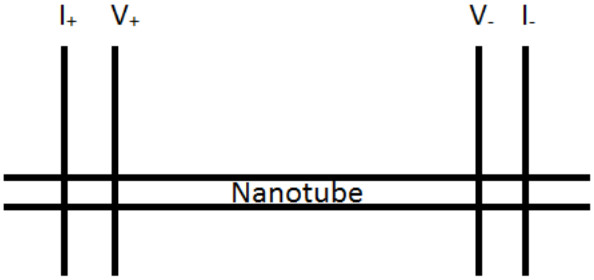

Figure 14. Schematic diagram of a four-point probe measurement method.

2.3.2 Connecting Nanotubes for Measurement

Once I had sufficiently long nanotubes I was able to start connecting the contact leads to my nanotubes. As a substrate I chose a silicon wafer with a silicon nitride isolation layer so that the top layer would be insulating. I used a diamond tip cutting tool to cut the wafers into approximately 1 cm by 1 cm squares. To clean the substrates I rinsed them with acetone, then methanol, then de-ionized water and dried them using nitrogen gas. For the large contact pads, I crossed four small diameter wires at the center of my small silicon wafers and used that as a mask during evaporation. I made sure to cover the edges of the wafers so that no evaporation would occur on the conducting part of the silicon wafer thereby shorting all of the leads. I evaporated a 5 nm layer of chromium followed by a 60 nm layer of silver to make large contact pads on the silicon wafers. After the evaporation, I placed a drop of nanotube suspension at the center cross section of the wafer. In order to view, design and pattern the platinum connections, I used the Tescan LYRA-3 Model GMH Focused Ion Beam (FIB) with a built in scanning electron microscope (SEM). The accelerating voltage for the FIB was set to 30 kV and the platinum lines I drew were 250 nm wide. Once I located a suitably long nanotube on the substrate, I used the FIB to deposit platinum and connect the nanotube to the large contact pads, as seen in Figure 15.

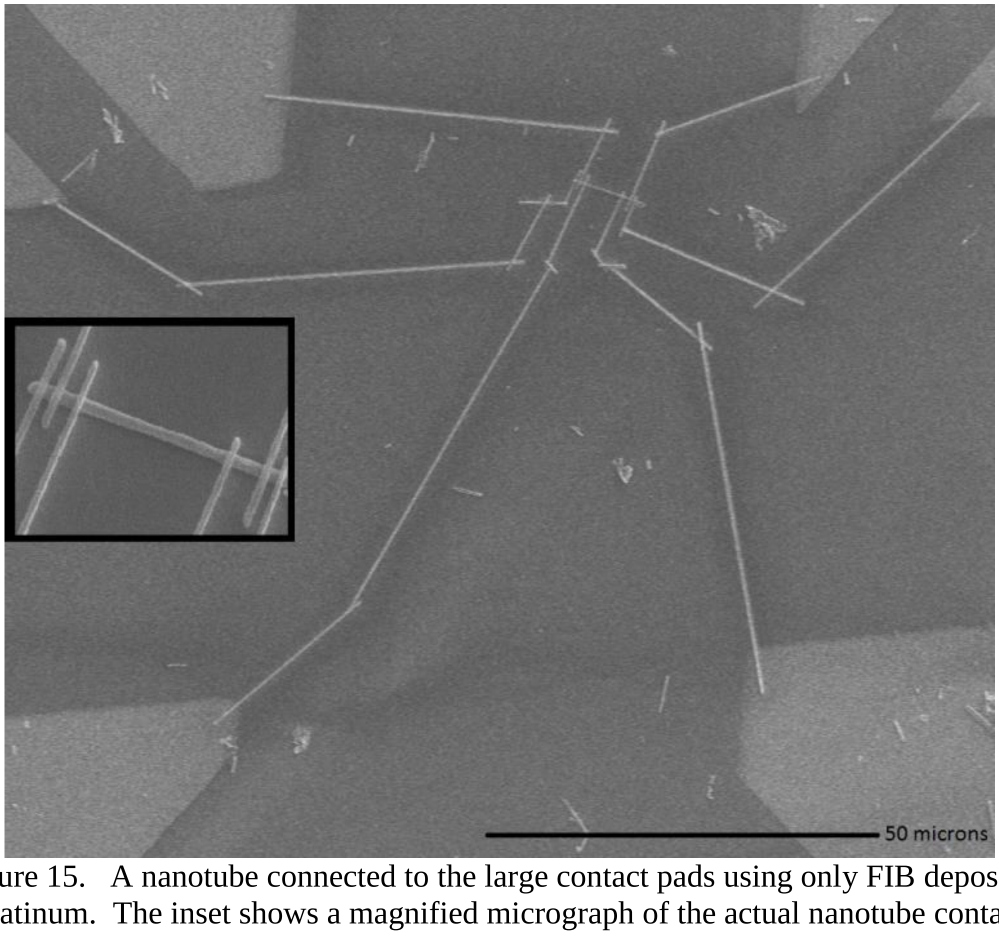

Figure 15. A nanotube connected to the large contact pads using only FIB deposited platinum. The inset shows a magnified micrograph of the actual nanotube contact pattern.

Unfortunately, the patterns made using only the FIB turned out to have too high of a resistance. The resistance of the platinum was high because the gas used for deposition has too many contaminants and is typically used as a protective layer for ion milling. The length of patterns needed also contributed to the high resistance. In order to minimize the length of the FIB patterns, Dr. Wenhao Wu drew an electron beam lithography (EBL) pattern connecting the large contact pads to the nanotube. After the EBL pattern was drawn, I evaporated a 5 nm layer of chromium followed by a 50 nm of silver. Then in order to ensure a good contact, I used the FIB to connect the nanotube to the EBL pattern. On some samples, I drew more than four contact connections because that enabled me to measure different sections and lengths on the same nanotube. Figure 16 shows a completed pattern, including the large silver pads, the EBL pattern and the platinum lines deposited using FIB which connect to the nanotube. It is important to note that the FIB pattern lines are short in order to decrease the contact resistance values and reduce damage to the nanotubes by the ion beam.

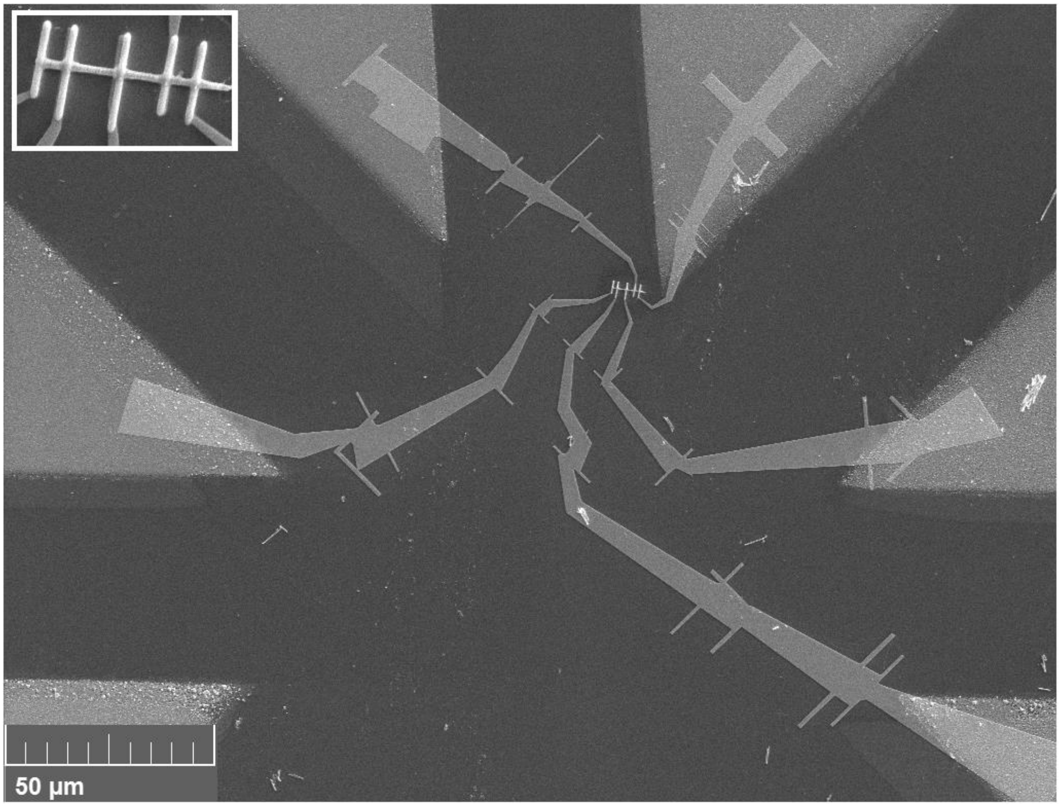

Figure 16. A nanotube connected to large contact pads using a combination of EBL and FIB. The inset shows a magnified micrograph of contacts across the nanotube.

The figure also shows other nanotubes randomly distributed on the surface and that is due to the fact that I am using a liquid suspension of nanotubes and cannot control where the nanotubes end up.

Table 1 shows a representative example of how annealing a nanotube for 2 minutes, reduces its resistance. This specific nanotube had five different leads, labeled 1 through 5. This was a simple two probe measurement where R_{12} represents the resistance between leads 1 and 2, R_{13} represents the resistance between leads 1 and 3, and so on.

Table 1. Two probe resistance measurements for a nanotube before and after annealing.

	No Annealing	Annealed 2 minutes
R_{12}	1.7 kΩ	400 Ω
R_{13}	85 kΩ	3.7 kΩ
R_{14}	111 kΩ	5.0 kΩ
R_{15}	114 kΩ	5.5 kΩ
R_{23}	83 kΩ	3.5 kΩ
R_{24}	110 kΩ	4.8 kΩ
R_{25}	112 kΩ	5.2 kΩ
R_{34}	27 kΩ	1.4 kΩ
R_{35}	29 kΩ	1.8 kΩ
R_{45}	2.4 kΩ	560 Ω

Using a four probe measurement, the post-annealing resistance between leads 2 and 3 was 3.2 kohms. This shows the contact resistance is low (0.3 kohms) compared to the sample resistance, and therefore this is a valid four-point probe measurement.

3. NANOTUBE CHARACTERIZATION

3.1. Scanning Electron Microscope (SEM)

I used the SEM built into the FIB to view and pattern the samples. Figure 17 shows the same nanotube (a) prior to and (b) after annealing for 30 minutes. The SEM accelerating voltage was 10 kV. For the micrograph of the nanotube prior to annealing the magnification was 36.6 kX and for the micrograph of the nanotube after annealing the magnification was 30.3 kX. It appears that the nanotube edge becomes smoother and that the nanotube is not quite as granular after annealing.

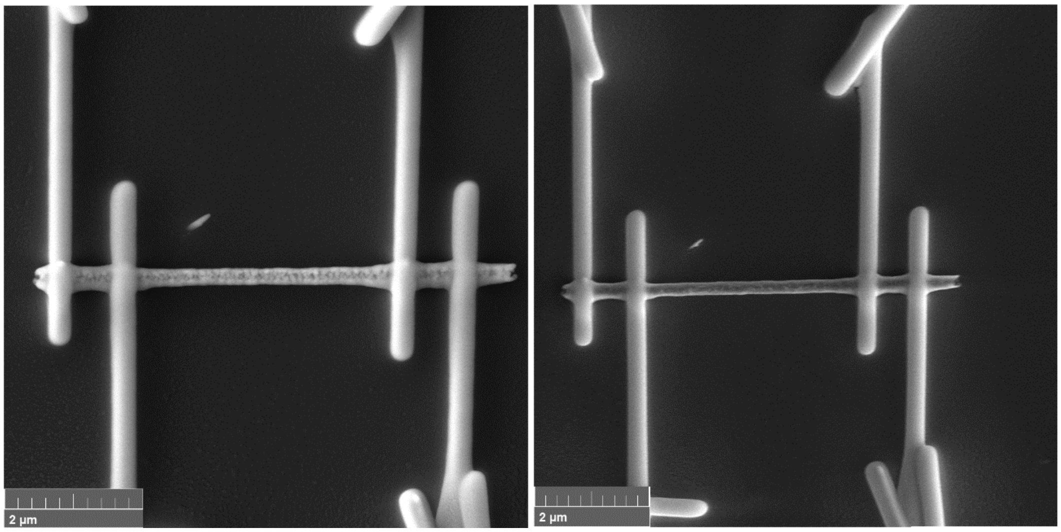

Figure 17. SEM of a nanotube (a) prior to and (b) after annealing for 30 minutes.

The figure shows that the deposited platinum lines slightly distort the shape of the nanotube at the contacts. It appears that the nanotube is slightly flattened by the platinum contacts.

3.2. Transmission Electron Microscope (TEM)

After dissolving the polycarbonate template in dichloromethane to release the silver-stannic oxide composite nanotubes, I placed a drop of solution on a TEM 400 mesh copper grid. These specific copper grids have a 5-6 nm thin film of pure carbon deposited on one side of the copper grid for additional support. Dr. Hansoo Kim, an associate research scientist at Texas A&M University's Microscopy and Imaging Center took some micrographs of the nanotubes, and analyzed the electron diffraction patterns and energy dispersive x-ray spectra of the nanotubes. Dr. Kim used the FE Tecnai G2 F20 ST TEM, and I compared nanotubes that had been annealed with those that had not been annealed.

Using the TEM we were able to observe a hollow inner section indicating a nanotube shape. As mentioned earlier, the outer diameter of the nanotube depends on which section along the template pore the nanotube was formed. In Figures 18 and 19, the micrographs also show that there are particles present within the inner nanotube wall. Keeping in mind that the nanotube is 3-dimensional and this is a 2-dimensional micrograph, it does not appear the particles are evenly distributed throughout the nanotube. For that reason, the particles within the pore edge were not used to calculate the wall thickness of the nanotube. Figure 18 shows a TEM micrograph of a nanotube that had not been annealed with an outer diameter of 282 ± 2 nm and wall thickness of 17 ± 2 nm.

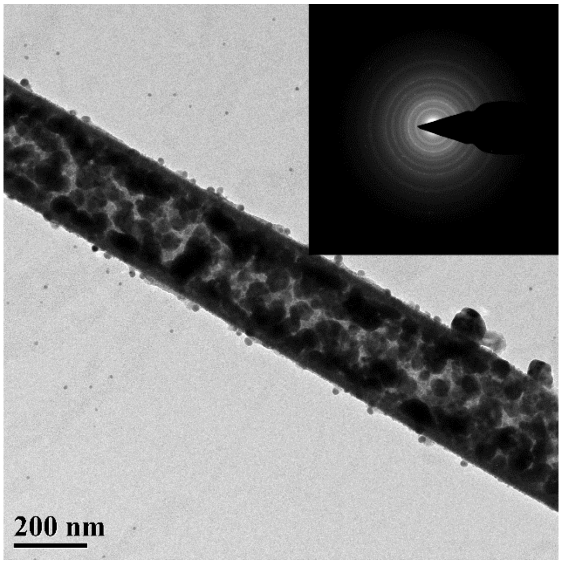

Figure 18. A TEM micrograph of a nanotube that had not been annealed and its corresponding electron diffraction pattern.

Figure 19 shows an annealed nanotube with outer diameter 272 ± 2 nm with a 17 ± 2 nm wall diameter.

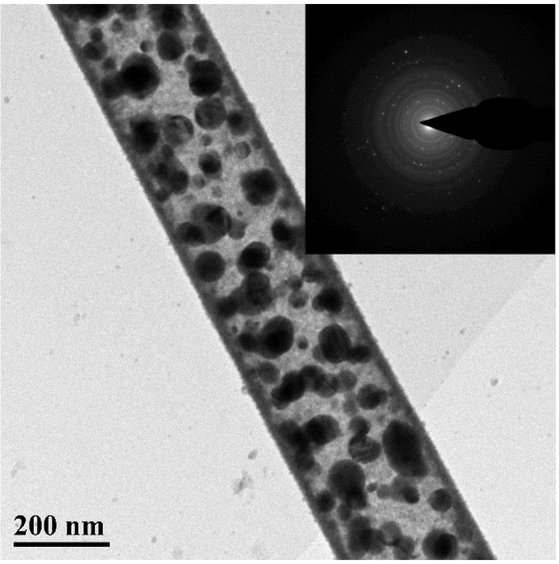

Figure 19. A TEM micrograph of a nanotube that had been annealed for 5 minutes and its corresponding electron diffraction pattern.

3.2.1 Electron Diffraction Pattern

Electron diffraction patterns are possible because of the electron’s wave nature. When a beam of electrons is directed toward a thin sample, the electrons interact with the sample structure and are diffracted. The ring structure pattern seen in the diffraction image is formed on the back focal plane of the TEM and is due to the constructive interference of the electron waves. For these diffraction patterns the acceleration voltage of the beam of electrons was 200 kV, and the camera length was 200 mm. Figure 20 shows the magnified diffraction pattern for the nanotube that had not been annealed (the same nanotube shown in Figure 18).

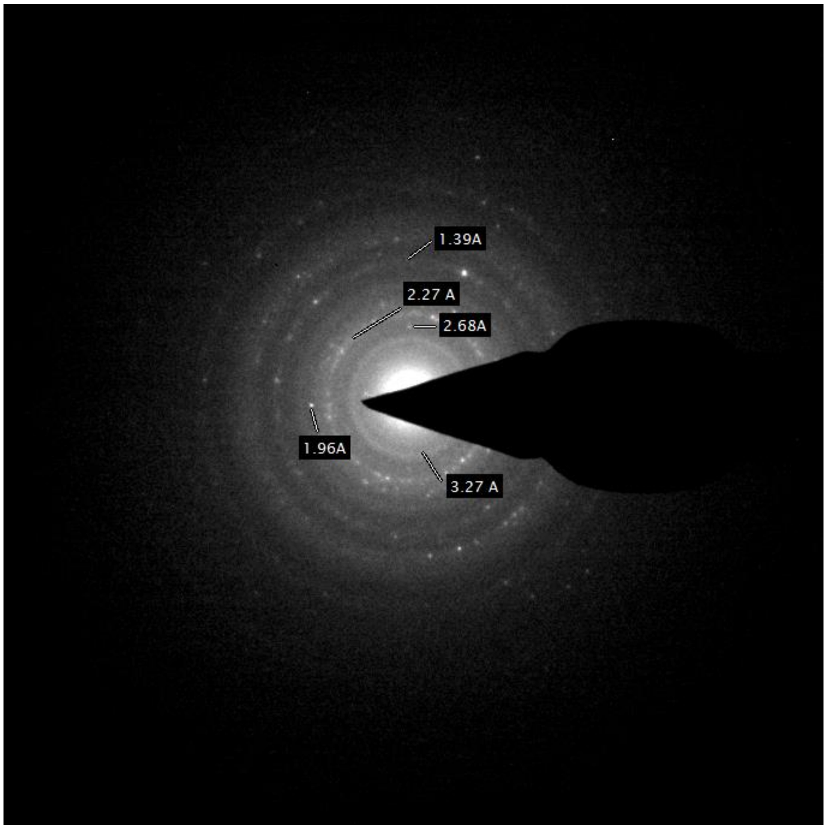

Figure 20. Magnified electron diffraction pattern of the nanotube shown in Figure 18 that had not been annealed.

From the diffraction pattern we measured the radii of each of the rings, then took the reciprocal since the diffraction pattern corresponds to reciprocal space. The reciprocal of each radii corresponds to the inter-planar spacing of the lattice structures. Using the obtained inter-planar spacing values we matched those values to the x-ray diffraction data provided by the International Centre for Diffraction Data (formerly Joint Committee on Powder Diffraction Standards) to determine which materials make up our sample. The diffraction pattern revealed the presence of both silver and stannic oxide. The stannic oxide is from the precursor steps.

Silver has a face centered cubic structure with lattice parameter $a = 4.08$ Å. For a cubic structure with lattice parameter a, the inter-planar spacing d, is given by

$$\frac{1}{d^2} = \frac{h^2+k^2+l^2}{a^2}. \qquad \textbf{(59)}$$

Here $h, k,$ and l represent the Miller indices and for a face centered cubic structure the only allowed reflections are from all even or all odd $h, k,$ and l. This means we expect to find the (111), (200), (220), and (311) planes which correspond to inter-planar spacing values of $d = 2.36, 2.04, 1.44,$ and 1.23 Å, respectively.

As seen from the magnified electron diffraction pattern, we have identified $d = 2.27$ Å which corresponds to (111) planes; $d = 1.96$ Å which corresponds to (200) planes; and $d = 1.39$ Å which corresponds to (220) planes. These results are in good agreement with previous research[55] and vary less than 4 % from the expected values which is a reasonable result. The values we are comparing to are the values for bulk materials. Even though we are using a 200 kV accelerating voltage for our beam of electrons, the accelerating voltage is not always exact leading to slight variations.

Stannic oxide has a tetragonal structure with $a = 4.738$ Å and $c = 3.187$ Å. For a tetragonal crystal the inter-planar spacing is given by

$$\frac{1}{d^2} = \frac{h^2+k^2}{a^2} + \frac{l^2}{c^2}. \qquad \textbf{(60)}$$

Based on our knowledge of the most pronounced peaks[56] and from previous research[57], we expect to see[58] $d = 3.35, 2.64,$ and 1.76 Å. On the electron diffraction pattern, we have identified $d = 3.27$ Å which corresponds to (110) planes; and $d = 2.68$ Å which corresponds to (101) planes. This time the percent difference is less than 3 %, which is again a reasonable result.

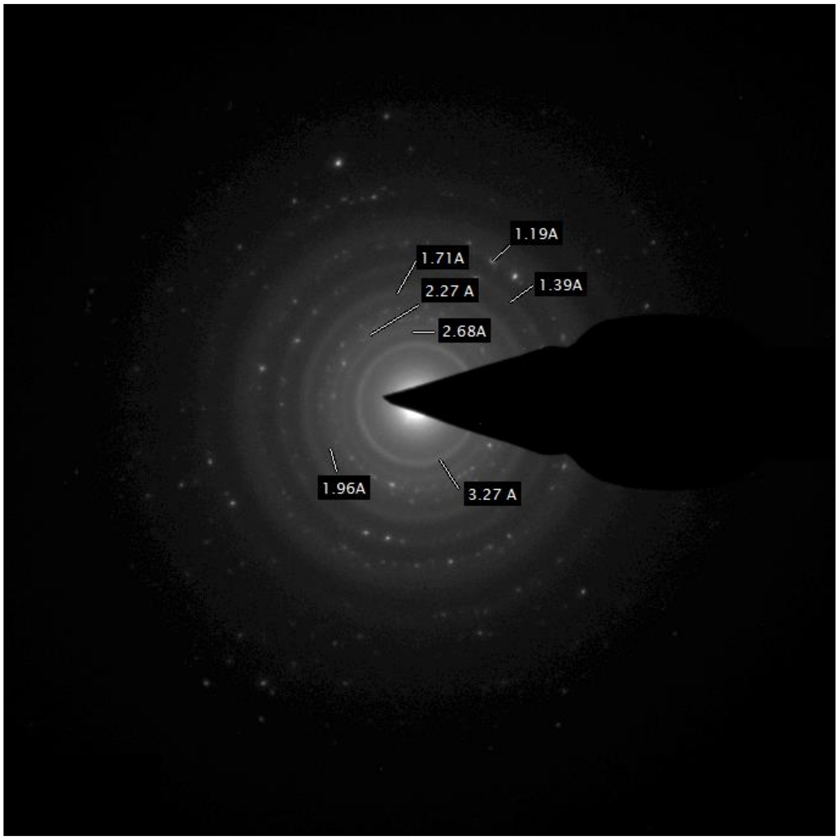

Figure 21. Magnified electron diffraction pattern of the nanotube shown in Figure 19 that had been annealed.

Figure 21 shows the magnified electron diffraction pattern for the nanotube that had been annealed (originally shown in Figure 19). In this figure we have identified silver with inter-planar spacing values of $d = 2.27$ Å which corresponds to (111) planes; $d = 1.96$ Å which corresponds to (200) planes; $d = 1.39$ Å which corresponds to (220) planes; and $d = 1.19$ Å which corresponds to (311) planes. We were also able to identify the stannic oxide planes (110) which corresponds to $d = 3.27$ Å; (101) which corresponds to $d = 2.68$ Å; and (211) which corresponds to $d = 1.71$ Å.

Typically a diffraction pattern made up of solid rings corresponds to amorphous structures, while a diffraction pattern made up of distinct spots corresponds to single crystalline structures. Both of the diffraction patterns are a mixture of faint rings and some spots and therefore correspond to a polycrystalline structure. We believe the grid supporting layer of amorphous carbon is also contributing to the faint ring patterns. Structural and/or compositional disorder are a significant feature of polycrystalline materials. Comparing the electron diffraction patterns before and after the annealing process shows that the faint ring patterns become less pronounced. I believe this is due to the fact that the annealing process helps to reduce the disorder in the nanotube

3.2.2 Energy Dispersive X-ray Spectroscopy (EDS)

In order to further analyze the nanotube structure we also analyzed the drift corrected energy dispersive x-ray spectrum. Figure 22 shows the line scan for a nanotube that had not been annealed. On the left side, the red line represents the location where the line scan was taken and the red square represents the section of nanotube used for drift correction.

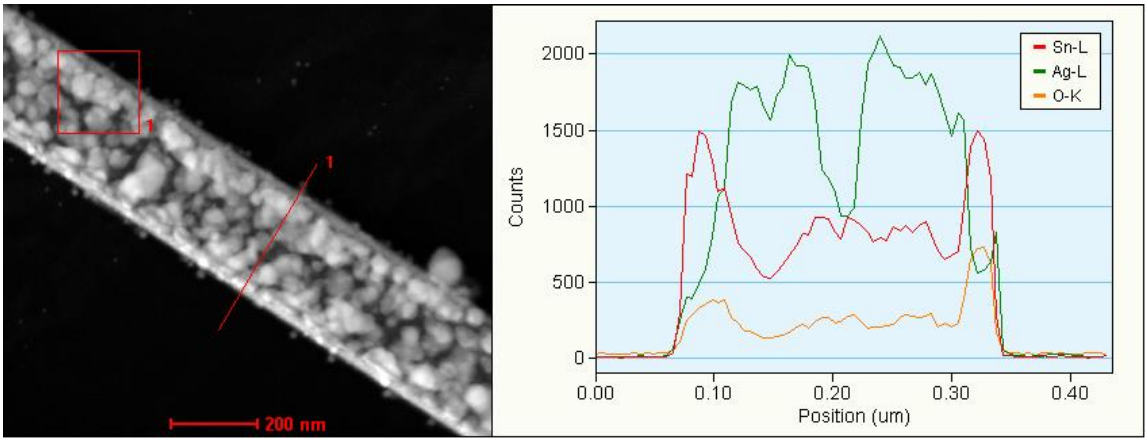

Figure 22. Drift corrected energy dispersive x-ray spectroscopy line scan for the nanotube that had not been annealed.

Since we used tin in one of the precursor steps, the stannic oxide is confined to the outer edge of the nanotube. It is important to note the presence of silver even at the very edge of the nanotube. This supports the idea that the nanotube is not simply a nanotube with two distinct layers, but is instead a mixture of stannic oxide and silver. There is a higher concentration of stannic oxide at the outer edge, but it appears the silver fills in the gaps between the stannic oxide and then starts to grow inward. This is consistent with the fact that when I dissolved the template prior to the silver deposition step all that was left was random nanoparticles and not nanotubes.

Figure 23 presents the full energy dispersive x-ray drift corrected spectrum profile for the nanotube that had not been annealed. From this spectrum one can see the silver, tin and oxygen peaks from the nanotube as well as the copper and carbon peaks from the copper grid with supporting carbon film. The variable x represents the fraction of the total volume occupied by metallic grains. From the EDS data of this specific nanotube that had not been annealed, I was able to find that the fraction of the total volume occupied by metal grains was $x = 0.62$.

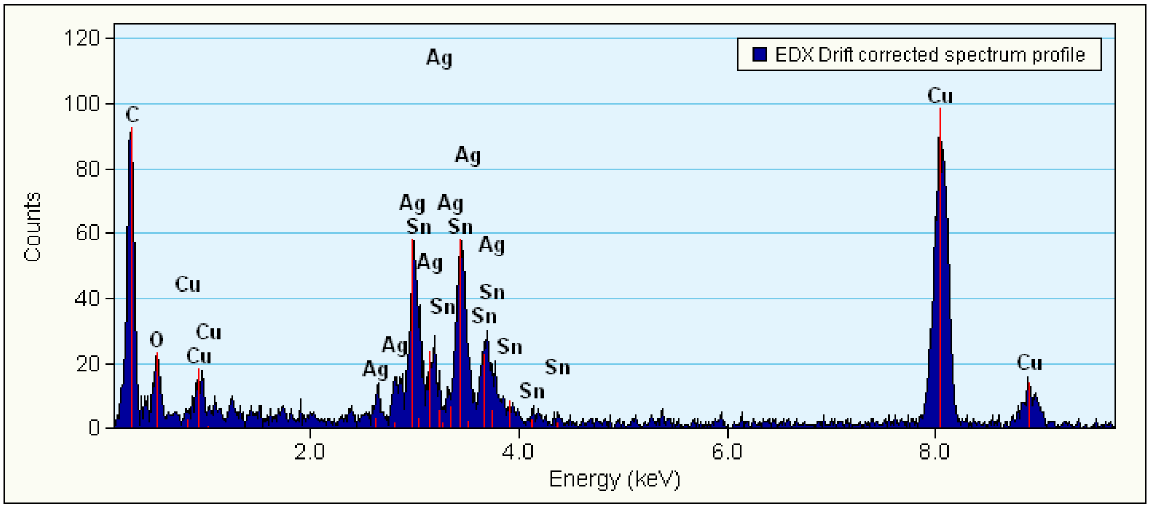

Figure 23. Energy dispersive x-ray drift corrected spectrum profile for the nanotube that had not been annealed.

We did a similar analysis on the nanotube that had been annealed for 5 minutes. On the left side of Figure 24, the red line again represents the location of the line scan and the red square represents the section of the nanotube used for drift correction. In this figure it is clear to see that the particles that have grown into the inner part of the nanotube are made up of silver. The big valley in the silver signal corresponds to a section across the line scan where there is no “large” particle present. The silver count however, still does not go to zero, indicating there is still a thin layer of silver in the outer edge of the nanotube.

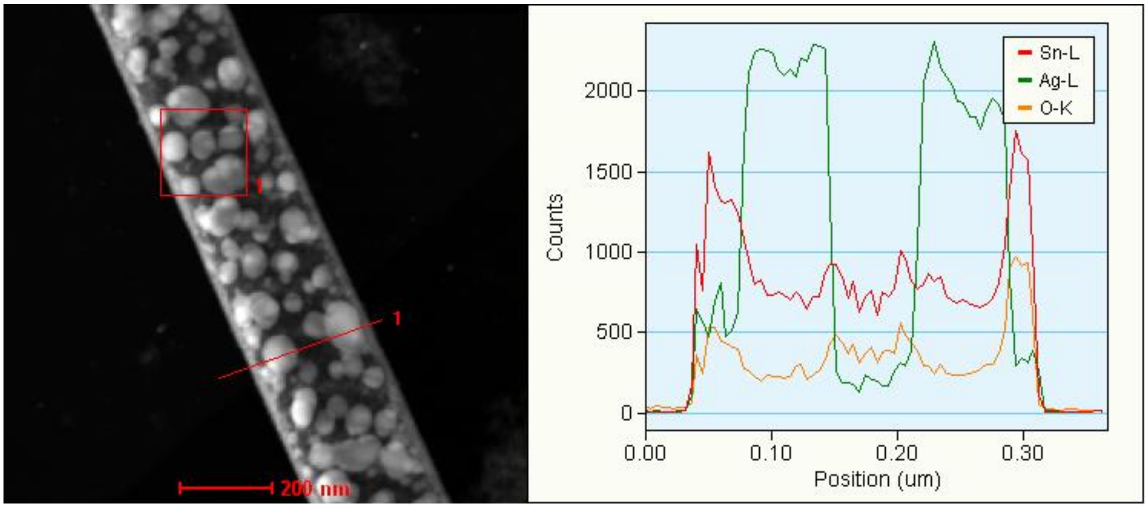

Figure 24. Drift corrected energy dispersive x-ray spectroscopy line scan for the nanotube that had been annealed for 5 minutes.

Figure 25 shows the complete energy dispersive x-ray drift corrected spectrum profile for the nanotube that had been annealed. The results are similar to the nanotube which had not been annealed. The silver, tin, and oxygen peaks from the nanotube are present, as well as the copper and carbon peaks from the TEM support grid.

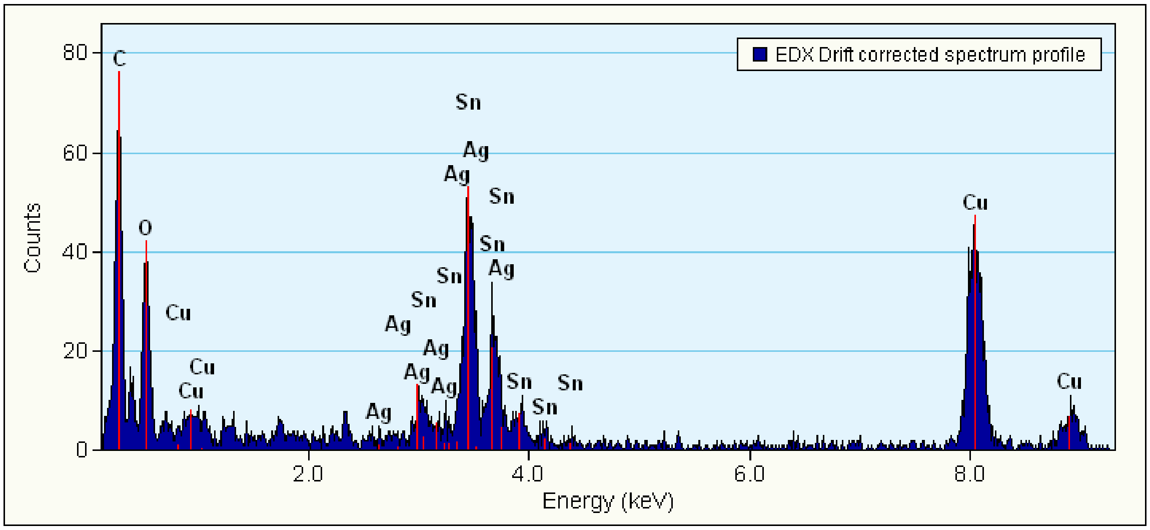

Figure 25. Energy dispersive x-ray drift corrected spectrum profile for the nanotube that had been annealed for 5 minutes.

From the energy dispersive x-ray data we were also able to determine the silver to stannic oxide composition ratio. From the EDS data of this specific nanotube that had been annealed, I was able to find that the fraction of space occupied by metal grains was $x = 0.58$. From the EDS data we are able to conclude that our nanotubes do not have the same values for x indicating that the fraction of space occupied by metal grains is likely to vary from nanotube to nanotube.

4. RESULTS AND DISCUSSION

After making contact with the nanotubes, I mounted the samples into the Quantum Design Model 6000 Physical Property Measurement System (PPMS). I used the rotating resistivity puck mount for measurements so that I was free to rotate the nanotube and align it as necessary. The resistivity puck comes with preset I_+, I_-, V_+, and V_- designations to which I connected the appropriate sections of the nanotube. For all of the following resistance versus temperature and magnetoresistance measurements, I used a 0.1 μA excitation current and the AC drive mode. According to the user's manual, in AC drive mode, the user bridge actually applies a DC excitation to the sample and measures the potential drop across the sample. Then the user bridge reverses the direction of the current and measures the potential drop across the sample again. It then averages the absolute values of the potential drops and from that calculates the resistance of the sample. Since the absolute values of the potential drops are averaged, the PPMS also provides a standard deviation for each data point. Using the standard deviation of each resistance measurement, I calculated the percent error for each data point. For all of the resistance measurements using PPMS, the percent error was less than 0.5 %. As a result, the lengths of the error bars are smaller than the data point designations and are therefore not shown.

Due to the fragility of the samples, only three of the samples actually survived all the measurements. In the proceeding sections, I will discuss each sample in great detail. All three samples were taken from the same batch and therefore were prepared under identical conditions. It was not possible to measure the specific wall thickness of each nanotube measured, but from the previous TEM micrographs of various nanotubes, I know the wall thickness is about 17 ± 2 nm regardless of the sample diameter. I measured the sample diameters after the platinum was deposited which caused a slight flattening of the nanotube. Sample A had a diameter of 351 ± 10 nm, a measureable length of 1.68 ± .01 μm and had not been annealed prior to measurements. By measurable length, I mean the distance between the V_+ and V_- leads. Sample B had a diameter of 354 ± 10 nm, a measureable length of 0.67 ± .01 μm and had been annealed for 7 minutes prior to measurements. Sample C had a diameter of 317 ± 10 nm, a measurable length of 1.89 ± .01 μm and had been annealed for 2 minutes prior to measurements.

4.1. Resistance versus Temperature

As mentioned earlier, all the resistance measurements from the PPMS have a percent error of less than 0.5 %. Since the error bars are smaller than the point designations, they are not shown in the following resistance versus temperature plots.

For the resistance versus temperature measurement of Sample A, the sample was cooled from 300 K down to 1.8 K. From 300 K to 50 K, data were recorded every 50 K; from 50 K to 10 K, data were recorded every 10 K; and from 10 K down to 1.8 K, data were recorded every 2.05 K. Figure 26 shows the resistance versus temperature plot for Sample A. As seen in the figure, as the temperature decreased, the resistance increased slowly. Then as the sample cooled past approximately 50 K, the resistance increased more rapidly. For Sample A at 300 K, the resistance was approximately 3.2 kohms, and at 1.8 K, the resistance was almost 11 kohms. From 300 K to 1.8 K, the resistance of Sample A increased by 3.3 times.

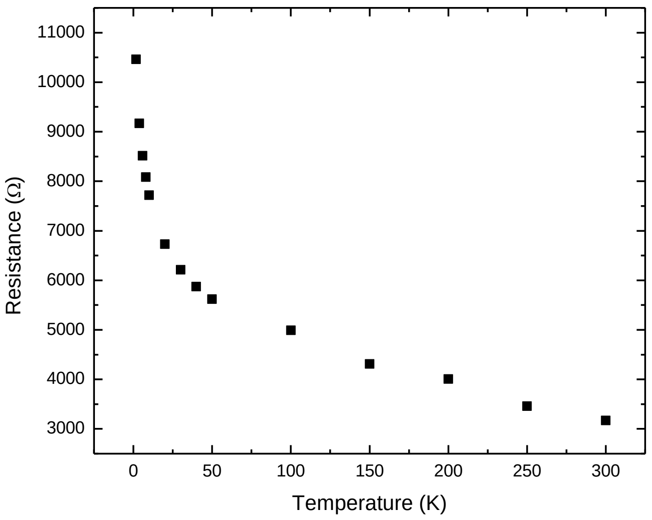

Figure 26. Resistance versus temperature plot for Sample A from 300 K to 1.8 K.

For the resistance versus temperature measurement of Sample B, from 300 K to 50 K, data were taken every 25 K; from 40 K to 10 K, data were taken every 5 K; and from 10 K to 1.8 K, data were taken every 1.025 K. Figure 27 shows the resulting resistance versus temperature plot. As seen in Figure 27, Sample B shows a pattern of behavior similar to Sample A, but the resistance is significantly lower. For Sample B, as temperature decreased, the resistance increased. Once the temperature cooled past 50 K, the resistance increased at a faster rate. At 300 K the resistance of Sample B was approximately120 ohms, and at 1.8 K the resistance was 150 ohms. For Sample B, the resistance increased to 1.3 times its initial value as it cooled from 300 K to 1.8 K.

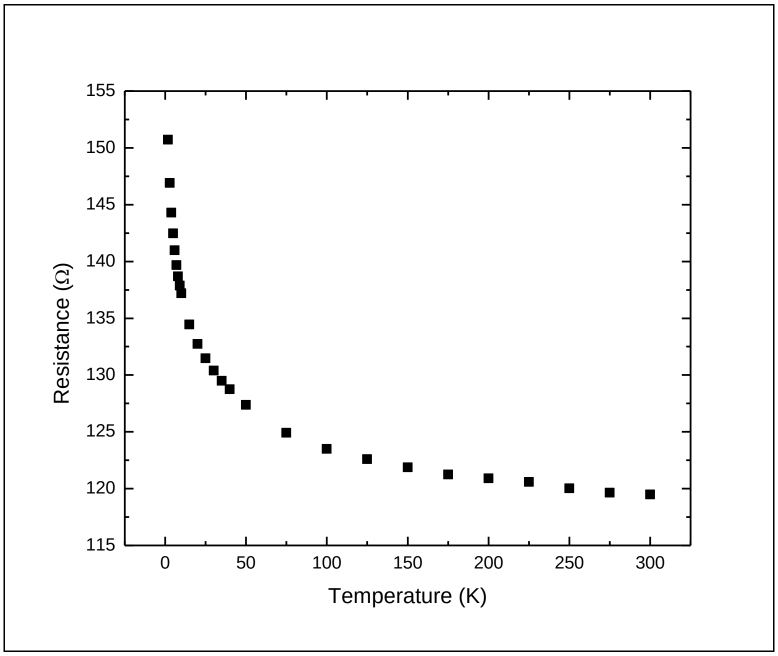

Figure 27. Resistance versus temperature plot for Sample B from 300 K to 1.8 K.

For the resistance versus temperature measurement of Sample C, the sample was cooled from 300 K down to 1.8 K. From 300 K to 50 K, data were recorded every 25 K; from 40 K to 10 K, data were recorded every 5 K; and from 9 K down to 1.8 K, data were recorded every 1.03 K. Figure 28 shows the completed resistance versus temperature plot for Sample C. Figure 28 shows that the behavior of Sample C is different from Samples A and B. At 300 K the resistance of Sample C was approximately 3.3 kohms, and at 1.8 K the resistance was 3.4 kohms. For Sample C, the resistance initially decreased as it cooled down, but then started to increase at around 50 K. Eventually the resistance rose to 1.02 times its initial value.

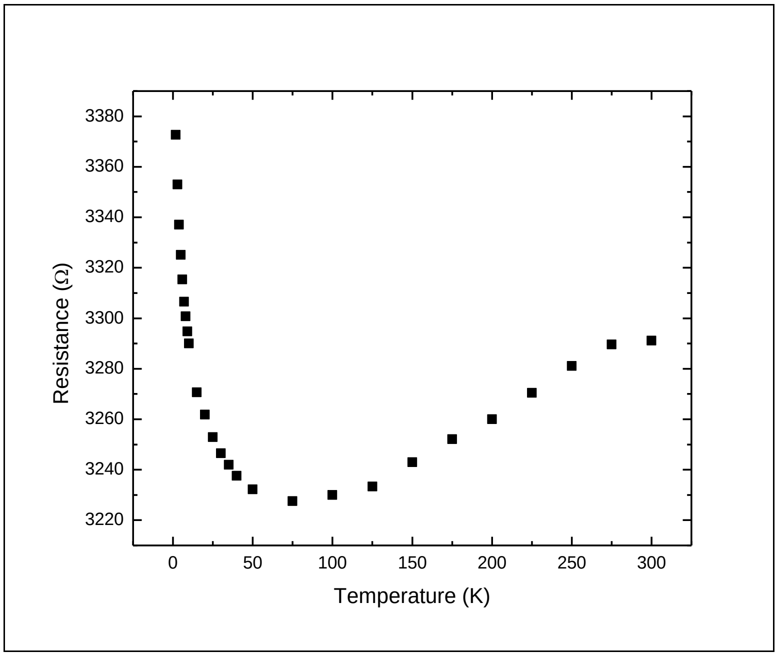

Figure 28. Resistance versus temperature plot for Sample C from 300 K to 1.8 K.

4.1.1 Resistivity

Using the measured dimensions of each sample, I calculated their resistivity at 300 K. The resistivity can be calculated using the equation $\rho = RA/l$. Sample A had a calculated resistivity of $\rho = 3.26 \cdot 10^{-3}\ \Omega \cdot \mathrm{cm}$, Sample B had a calculated resistivity of $\rho = 3.21 \cdot 10^{-4}\ \Omega \cdot \mathrm{cm}$, and Sample C had a calculated resistivity of $\rho = 2.79 \cdot$

$10^{-3}\ \Omega \cdot \mathrm{cm}$. Since the annealing process helps to reduce the resistivity of a sample, it is interesting to note that Sample B, which was annealed the longest, had the smallest resistivity. Furthermore, the sample which was not annealed at all, Sample A, had the largest resistivity. As a comparison, the resistivity[2] of bulk silver at 293 K is $\rho = 1.59 \cdot 10^{-6}\ \Omega \cdot \mathrm{cm}$.

4.1.2 Residual Resistance Ratio

Since we know that at low temperatures impurity scatterings contribute to the resistance, another valuable piece of information is the residual resistance ratio (RRR). In metals, the RRR serves as a rough estimate of the level of impurity in a sample.[59] A large RRR indicates a high purity sample, while a small RRR indicates a high level of impurity in the sample.[59] Although I have composite nanotubes, I will simply use the RRR as a tool for comparison of sample quality. I will use it as a more general measure for the amount of disorder. For Samples A and B, I used $RRR = R_{300\,K}/R_{1.8\,K}$. The calculated values were $RRR = 0.30$ for Sample A, and $RRR = 0.79$ for Sample B. For Sample C since the resistance reaches a minimum at 75 K, I used $RRR = R_{300\,K}/R_{75\,K}$ and got $RRR = 1.02$.

In the data, Sample C has the highest RRR indicating the lowest level of disorder and yet from the temperature dependent resistance data it still does not obey the Bloch-Gruneisen formula, but instead strongly resembles that of a dirty metal. In a dirty metal as the temperature initially cools down, the resistance decreases because the phonon vibrations in the lattice decrease. Once below a certain temperature, the resistance begins to increase as the effects of disorder begin to dominate.[60]

In Samples A and B, it appears that the contribution due to disorder is already dominating even at room temperature. In Sample A, which has the lowest RRR the resistance increases at a faster rate than in Sample B.

4.2. Current – Voltage Curves

Semiconductors and metals have very distinct current – voltage curves. Since the nanotubes were made up of both stannic oxide and silver, it seemed useful to study the current – voltage curves. For these measurements, I used a lock-in amplifier with a 1 V rms AC output voltage at 40 Hz and a 10 MΩ limiting resistor, resulting in a current of 0.1 μA. I also used a 100 kΩ limiting resistor and swept the DC voltage from + 5 V to – 5 V. I took measurements at the following temperatures: 1.8 K, 3 K, 4 K, 6 K and 10 K.

Figure 29 shows the current – voltage curves for Sample A. The figure shows that the current – voltage curves at 1.8 K, 3 K and just barely at 4 K have non-linear behavior. However, as the temperature increases, the non-linearity decreases. For the measurements at 6 K and 10 K, the curves are linear, indicating ohmic behavior. From the current – voltage curves, I calculated the inverse slope of each line to get the resistance at that temperature. Since the PPMS resistance values at each of these temperatures had a percent error of less than 0.15 %, the resistance values from the current – voltage measurements were compared to those values. For Sample A, the resistance calculated from the current – voltage curves differed from the PPMS values by 2.2 % or less.

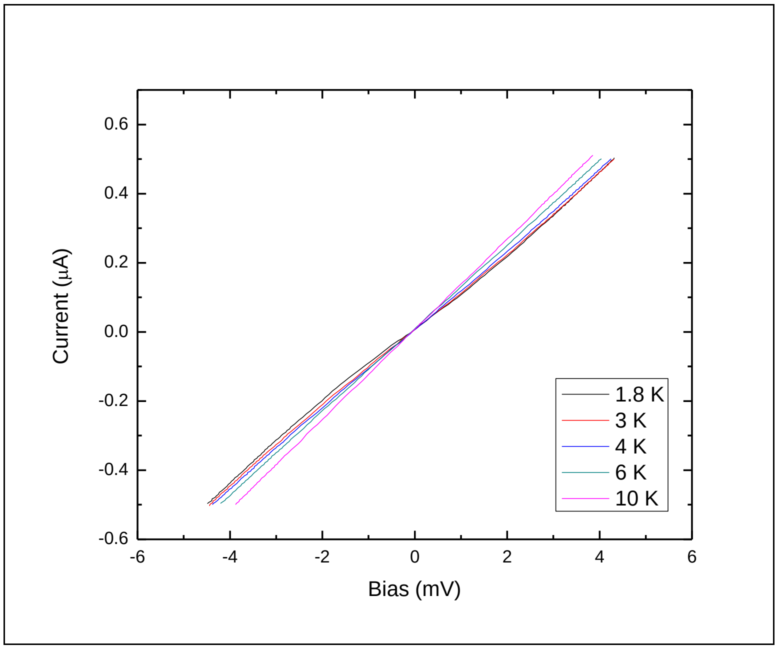

Figure 29. The current – voltage curves for Sample A. Data were taken at 1.8 K, 3 K, 4 K, 6 K, and 10 K.

Since the current – voltage curves were so close together, I also plotted the derivative of the current – voltage curves. Taking the noise into account, if the current – voltage curve was a straight line, the derivative would have an overall horizontal line. Figure 30 shows the derivative of the current – voltage curves for sample A. After 1.8 K, each subsequent curve was offset by 0.15 μA/mV for clarity. For the curves at 1.8 K, 3 K, and just barely at 4 K, there is a slight increase towards the outer edges of the curve. The 6 K and 10 K derivatives confirm that the current – voltage curves are straight lines.

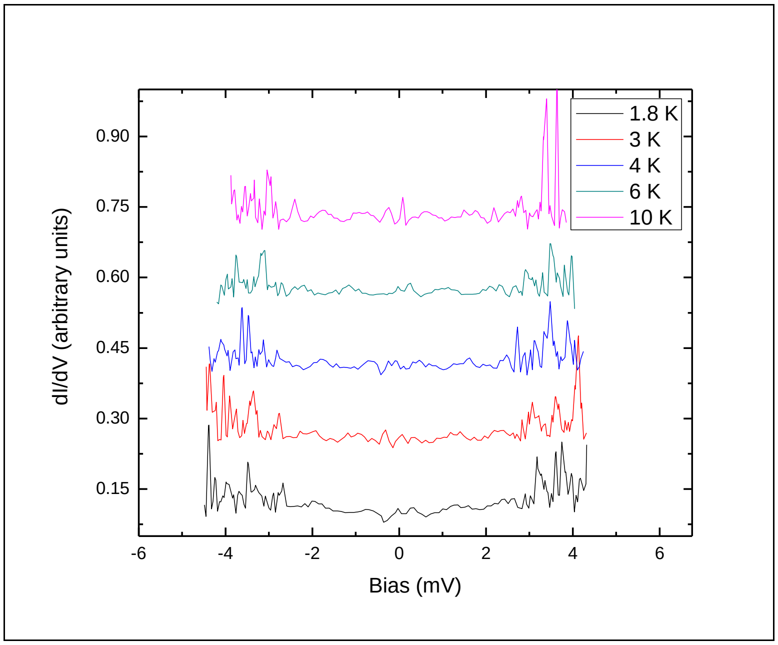

Figure 30. The derivatives of the current – voltage curves for Sample A. After 1.8 K, each subsequent curve was offset by a value of 0.15 µA/mV.

I used the same settings as before to measure the current – voltage curves for Sample B as shown in Figure 31. For Sample B, the current – voltage relationship corresponded to a straight line for all the measured temperatures. Since the PPMS resistance values at each of these temperatures had a percent error of less than 0.27 %, the resistance values from the current – voltage measurements were compared to those values. For Sample B, the resistance calculated from the current – voltage curves differed from the PPMS values by 4.4 % or less.

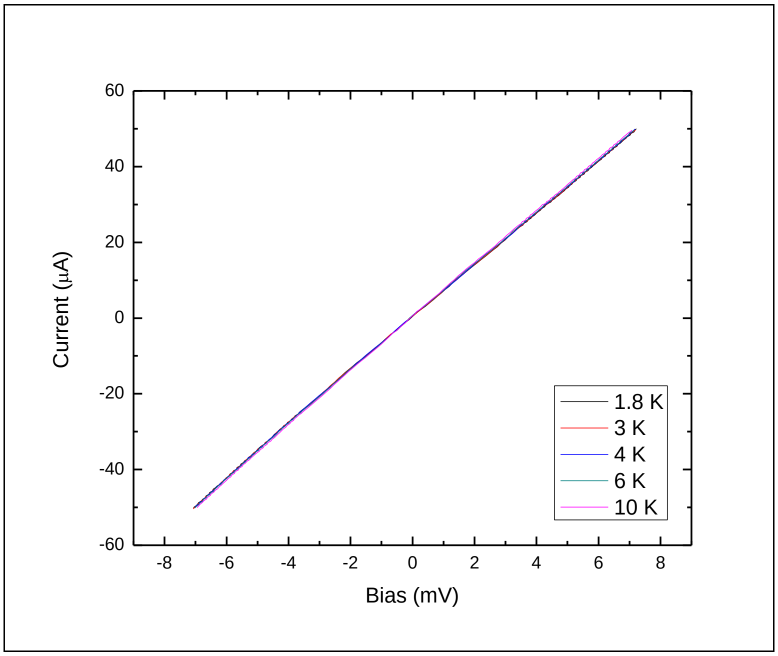

Figure 31. The current – voltage curves for Sample B. Data were taken at 1.8 K, 3 K, 4 K, 6 K, and 10 K.

Figure 32 shows the derivative of the current – voltage curves for sample B. After 1.8 K, each subsequent curve was offset by 6 μA/mV for clarity. At each temperature, the derivatives confirm that the current – voltage curves are straight lines.

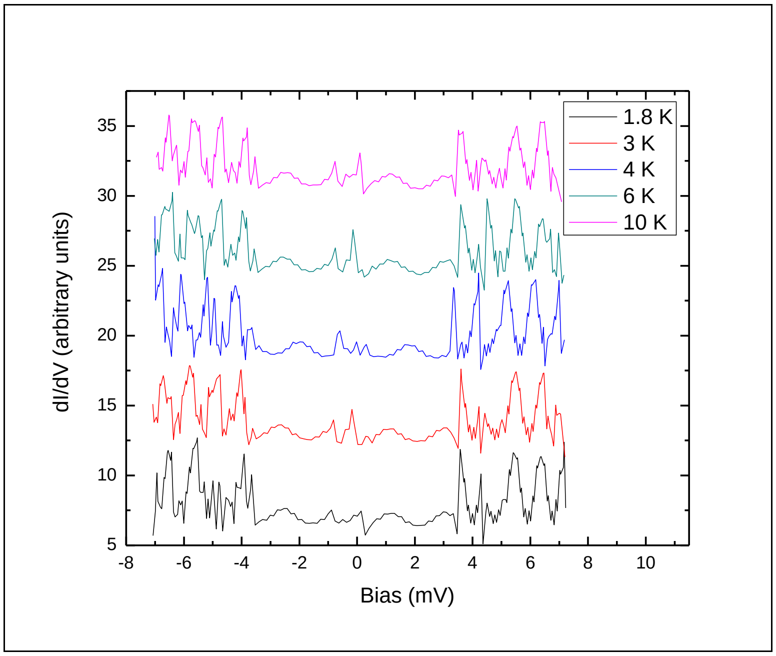

Figure 32. The derivatives of the current – voltage curves for Sample B. After 1.8 K, each subsequent curve was offset by a value of 6 µA/mV.

I used identical settings to measure the current – voltage curves of Sample C, but only have the results for the 1.8 K measurements. As seen in Figure 33, the current – voltage curve result was a straight line even at 1.8 K. If any non-linear behavior were to occur, it would have shown up in the 1.8 K measurement. Since the PPMS resistance value at 1.8 K had a percent error of less than 0.02 %, the resistance from the current – voltage measurement was compared to that value. For Sample C, the resistance calculated from the current – voltage curve differed from the PPMS value by 0.9 %.

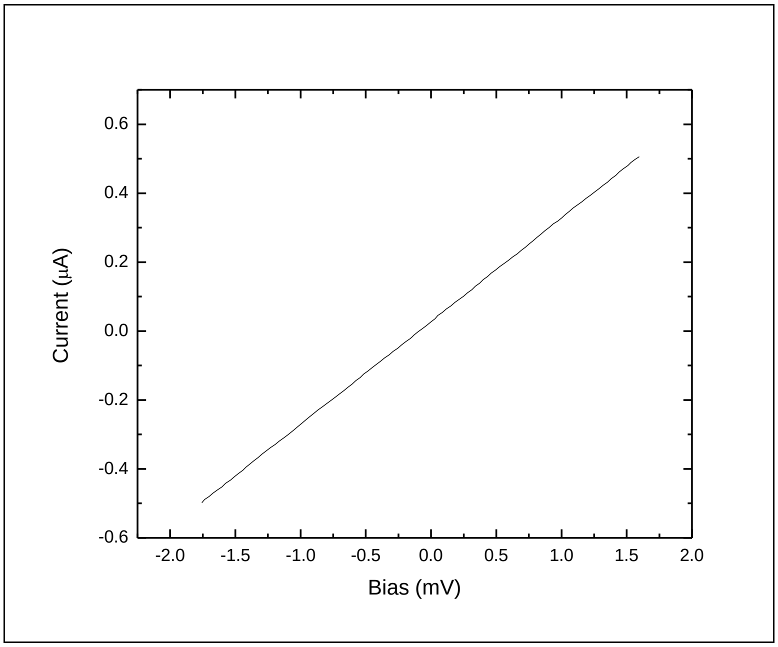

Figure 33. The current – voltage curve for Sample C measured only at 1.8 K.

Figure 34 shows the derivative of the current – voltage curve for sample C. The derivative confirms that the current – voltage curve is a straight line.

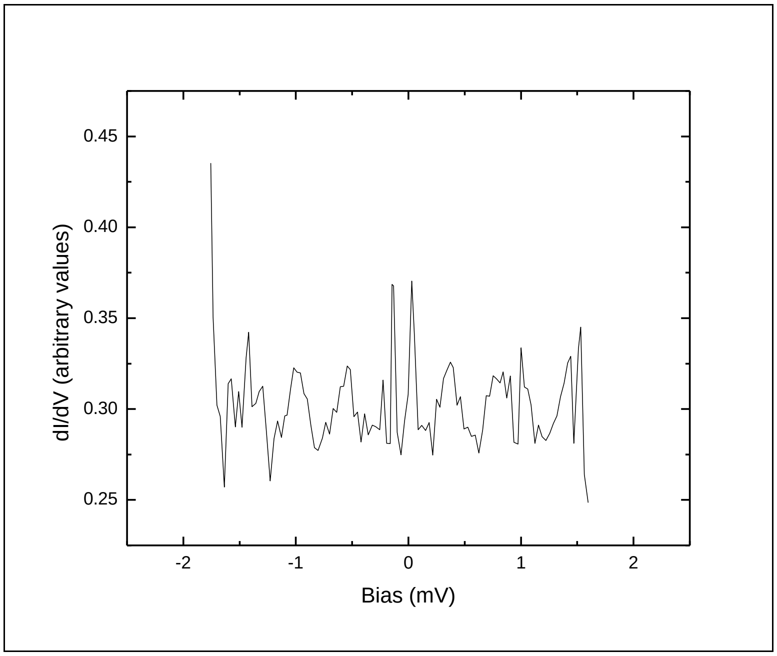

Figure 34. The derivative of the current – voltage curve for Sample C.

The non-linearity of the current – voltage curves for Sample A at temperatures 1.8 K, 3 K, and just a slight amount at 4 K indicate a departure from Ohm's law. At these temperatures the resistance is no longer constant, but instead depends on the current applied. The non-linearity of the current – voltage curves is not very pronounced, and only appears at the lowest temperatures in the sample with the highest level of disorder. This sample, Sample A, was also the sample that was not annealed and is very likely the most granular of the samples. The resistance for Sample A, is an order of magnitude larger than Sample C, and two orders of magnitude larger than Sample B at these temperatures, so it is possible that it is reaching some type of transport limit as it approaches these values. At these temperatures, the enhanced disorder and granularity of the sample as well as electron-electron interaction could be resulting in an Coulomb gap.[8] However, since the non-linearity of the curve is not very pronounced and disappears in annealed samples, it is difficult to make such a conclusion with certainty.

Also, there is no easy way to conclude if the non-linearity effect in Sample A is due to heating or not. However, for all the PPMS resistance measurements I used a 0.1 μA current, which was small enough that it was still in the linear regime. Since the current used for measurements was in the linear regime, sample heating is not an issue for my measurements.

4.3. Comparisons to Previous Work

Although electrical transport measurements of similar composite nanotubes have not been reported elsewhere, I did find experimental results by Wei and Li on similar composite film materials. Wei and Li analyzed 500 nm thick silver-stannic oxide nano-granular films, and studied their resistivity as a function of temperature.[43] Their results are shown in Figure 35.

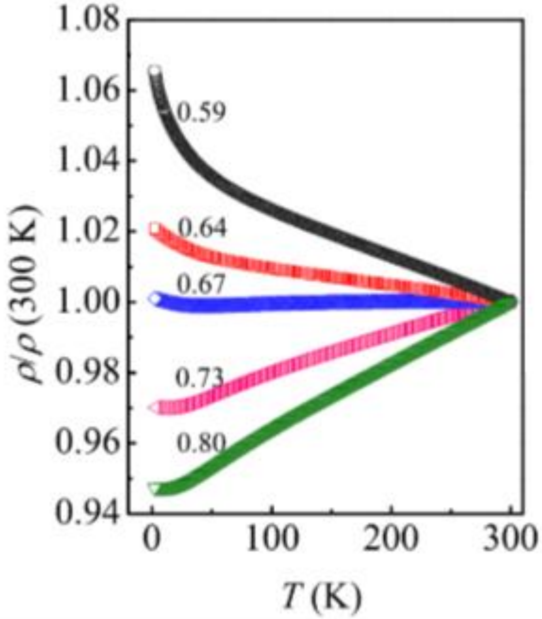

Figure 35. Wei and Li's resistivity as a function of temperature measurements of Ag+SnO_2 nano-granular films,[43] for $0.59 \leq x \leq 0.80$. (Used with permission Y. F. Wei and Z. Q. Li, 2013)

In their plot, the variable x represents the fraction of the total volume occupied by metallic grains. In their analysis of thin films for $x \gtrsim 0.67$, as the temperature decreased, the resistivity also decreased.[43] After the resistivity reached a minimum, it slightly increased with further decreasing temperature.[43] They attributed this behavior to that of a dirty metal in which the conducting paths are formed by the connected silver particles.[43] They also found that for $0.54 \lesssim x \lesssim 0.65$ the temperature coefficients of resistivity for each film were negative in the whole temperature range.[43] They concluded that these samples were governed by tunneling to the second nearest neighboring particles and that most of the conducting paths were broken.[43] In other words, the conduction is governed by hopping mechanisms.

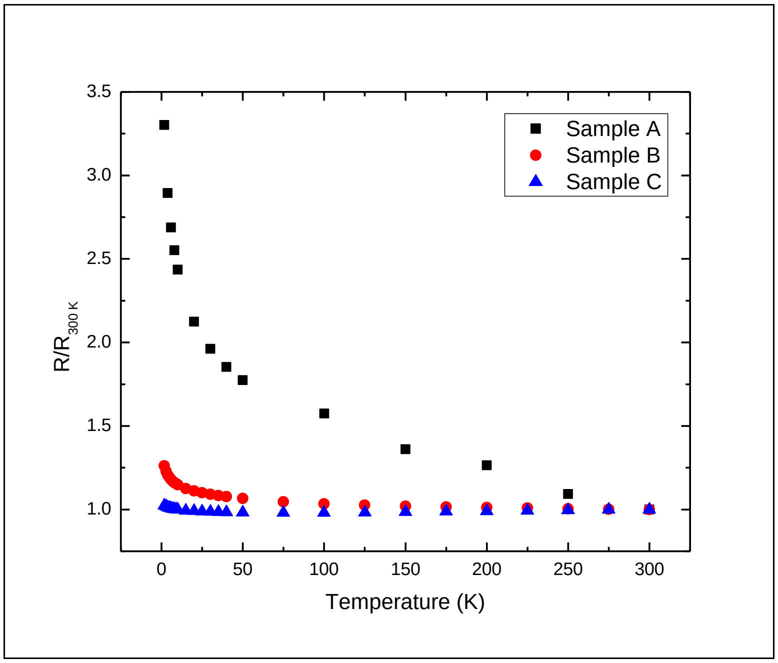

Figure 36. The normalized resistance R/R$_{300\ K}$ of Samples A, B, and C as a function of temperature.

To compare with the results by Wei and Li, I plotted my data as $R/R_{300\ K}$. My results are shown in Figure 36. As seen in the figure, my results are similar to those by Wei and Li, but unfortunately I do not know the specific x values of my nanotubes. Due to the fragility of my samples, as I tried to do additional measurements, all of my samples were damaged. As a result, I was not able to measure the fraction of total volume occupied by silver grains for the nanotubes used in my transport measurements. Although I do not know the exact values of x for the nanotubes I measured, I did analyze two other nanotubes which were made from the same batch. For those nanotubes, the fraction of total volume occupied by silver grains varies between $0.58 \leq x \leq 0.62$. Since I know the x values vary, it does not seem far-fetched that I could also have samples with slightly higher values of x. In fact, Sample A resembles the behavior of their sample $x = 0.59$, Sample B, resembles their sample $x = 0.64$, and Sample C, resembles their sample $x = 0.67$. I am not claiming that those are the x values of the nanotubes, simply pointing out the similarities in behavior. It seems plausible that even though the samples were all made from the same batch, some nanotubes may have a higher concentration of silver than others.

The main difference between their samples and mine is in the total increase of resistance as the sample cools down. None of their resistances increase to greater than 1.07 times its initial value. For the nanotube in my study with the greatest amount of disorder, the resistance increases to about 3.3 times its initial value. This seems consistent with the fact that surface scattering plays a much more dominant role in my thin nanotubes (17 nm wall thickness) than in their 500 nm thick films.

Since Wei and Li concluded that the transport in their silver-stannic oxide thin films was governed by hopping mechanisms, I chose to consider hopping as a transport mechanism for my samples as well.

4.3.1 Nearest-Neighbor Hopping

The equation for nearest-neighbor hopping is the same for any sample dimensionality and is given by[28]

$$\rho(T) = \rho_{NNH} \exp\left(\frac{\Delta E_{NNH}}{k_B T}\right).$$

Since $R \propto \rho$, if nearest-neighbor hopping was the governing transport mechanism in the nanotubes, plotting the natural logarithm of the resistance as a function of the inverse temperature would reveal a linear dependence. Figures 37, 38, and 39 show the ln(R) versus T^{-1} plots for Samples A, B, and C, respectively. None of the samples exhibited a linear section in the natural logarithm of the resistance versus inverse temperature plots, indicating that nearest-neighbor hopping was not likely the transport mechanism governing electrical conduction in the nanotubes.

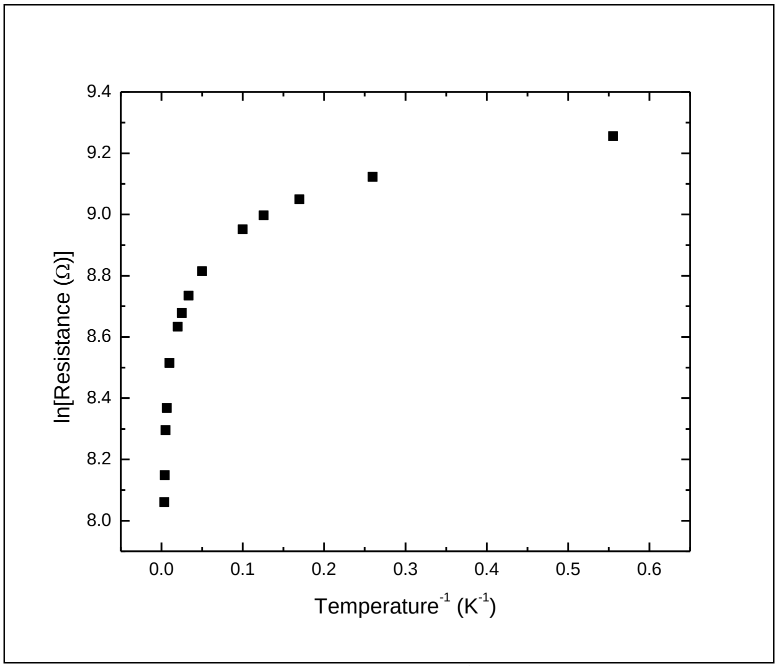

Figure 37. The ln(R) versus T^{-1} plot for Sample A.

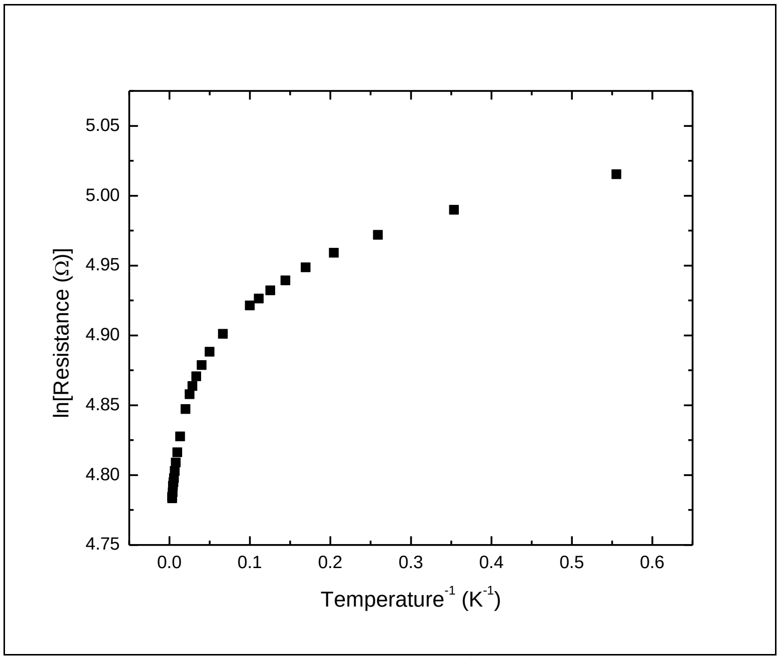

Figure 38. The ln(R) versus T^{-1} plot for Sample B.

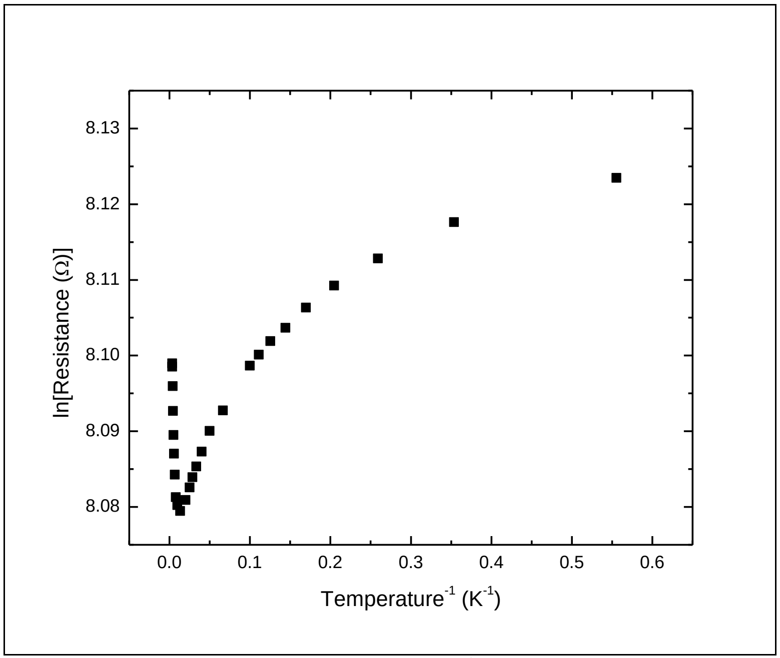

Figure 39. The ln(R) versus T^{-1} plot for Sample C.

4.3.2 Mott Variable-Range Hopping

The equation for Mott variable-range hopping is given by

$$\rho(T) = \rho_{Mott} \exp\left[\left(\frac{T_{Mott}}{T}\right)^{\frac{1}{1+\mathrm{n}}}\right],$$

where $n = 1,2, or$ 3 refers to one, two, or three-dimensional variable-range hopping.[36] Since $R \propto \rho$, if one-dimensional Mott variable-range hopping was the governing transport mechanism in the nanotubes, plotting the natural logarithm of the resistance as a function of the temperature raised to the negative 1/2 power would reveal a linear dependence. Figures 40, 41, and 42 show the ln(R) versus $T^{-1/2}$ plots for Samples A, B, and C, respectively. None of the samples exhibited a linear section in the natural logarithm of the resistance versus temperature raised to the negative 1/2 power plots, indicating that one dimensional Mott variable-range hopping was not likely the transport mechanism governing electrical conduction in the nanotubes.

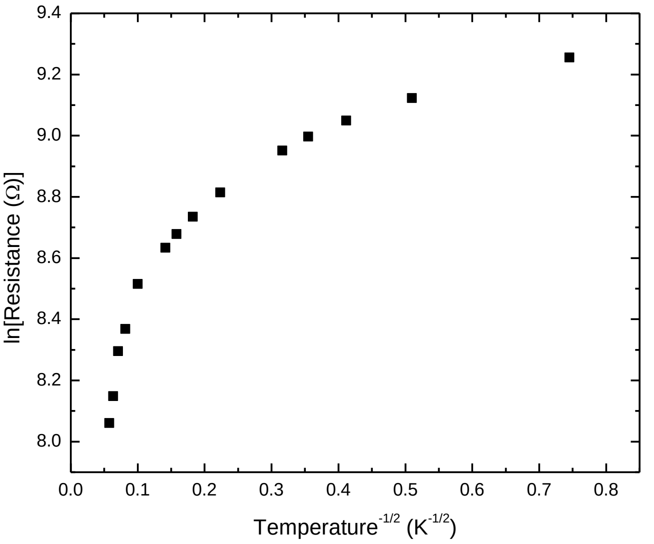

Figure 40. The ln(R) versus $T^{-1/2}$ plot for Sample A.

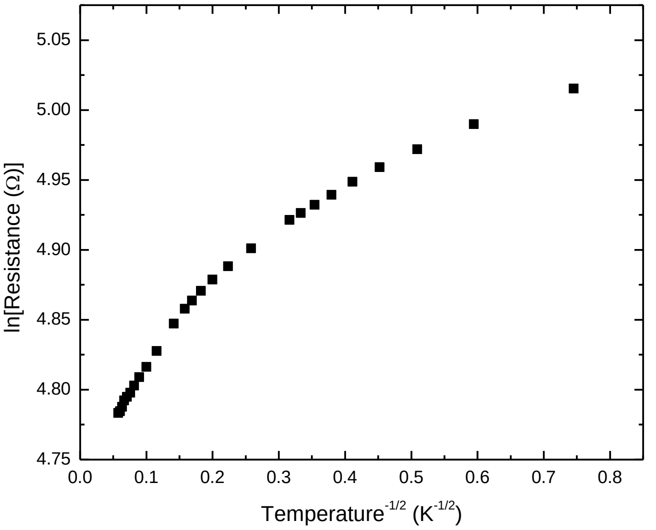

Figure 41. The ln(R) versus $T^{-1/2}$ plot for Sample B.

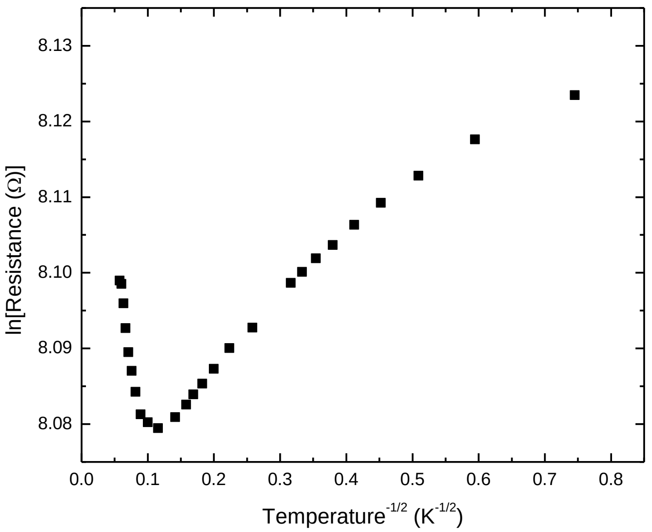

Figure 42. The ln(R) versus $T^{-1/2}$ plot for Sample C.

Based on the same equation, if two-dimensional Mott variable-range hopping was the governing transport mechanism in the nanotubes, plotting the natural logarithm of the resistance as a function of the temperature raised to the negative 1/3 power would reveal a linear dependence. Figures 43, 44, and 45 show the ln(R) versus $T^{-1/3}$ plots for Samples A, B, and C, respectively.

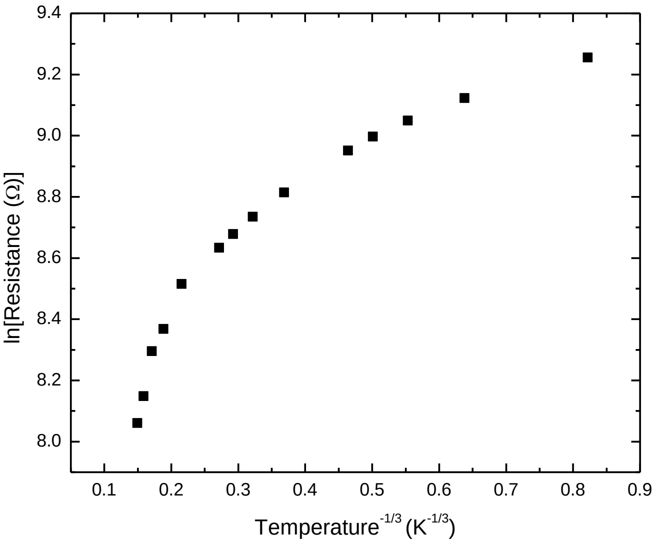

Figure 43. The ln(R) versus $T^{-1/3}$ plot for Sample A.

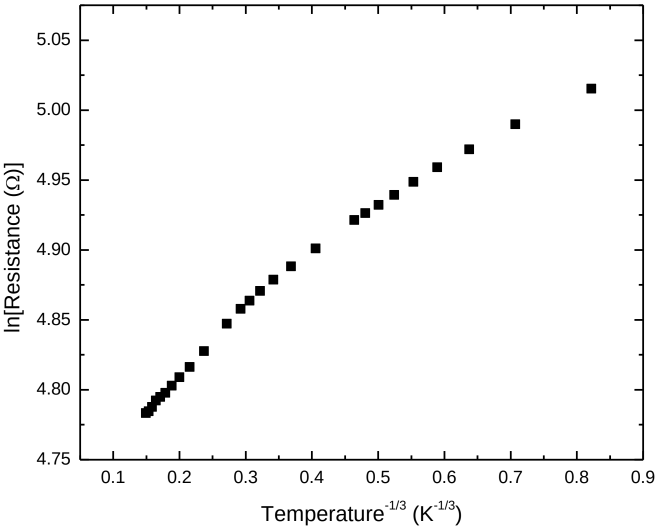

Figure 44. The ln(R) versus $T^{-1/3}$ plot for Sample B.

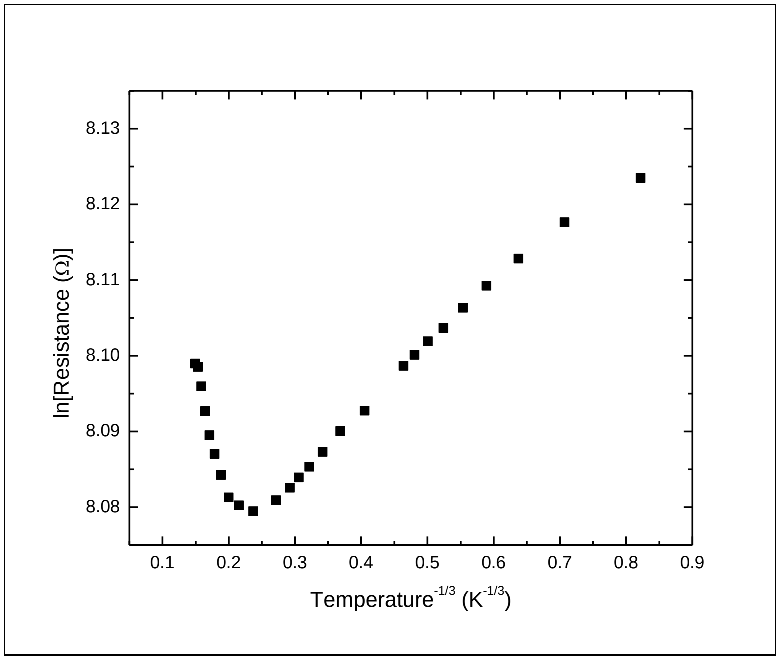

Figure 45. The ln(R) versus $T^{-1/3}$ plot for Sample C.

Sample A did not exhibit a linear section in the natural logarithm of the resistance versus temperature raised to the negative 1/3 power plot, indicating that two-dimensional Mott variable-range hopping was not likely the transport mechanism governing the electrical conduction in that sample. Although Samples B and C seemed to exhibit a linear section in the natural logarithm of the resistance versus temperature raised to the negative 1/3 power plots, the temperature range for that section corresponded to temperatures between 4.9 K and 9 K. Since the temperature range for the linear section was only 4.1 K, two-dimensional Mott variable-range hopping did not seem to be an appropriate fitting equation.

Based on the same equation, if three-dimensional Mott variable-range hopping was the governing transport mechanism in the nanotubes, plotting the natural logarithm of the resistance as a function of the temperature raised to the negative 1/4 power would reveal a linear dependence. Figures 46, 47, and 48 show the ln(R) versus $T^{-1/4}$ plots for Samples A, B, and C, respectively.

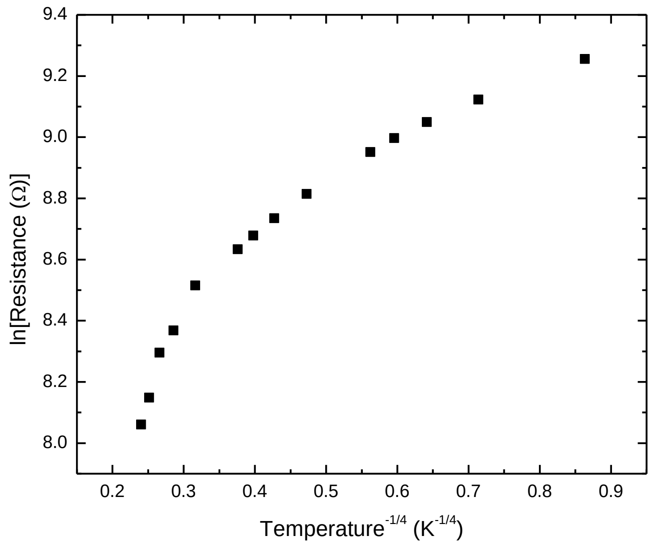

Figure 46. The ln(R) versus $T^{-1/4}$ plot for Sample A.

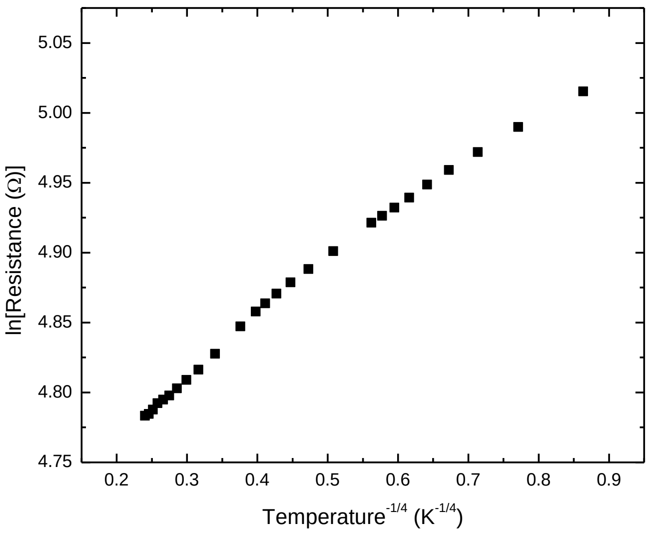

Figure 47. The ln(R) versus $T^{-1/4}$ plot for Sample B.

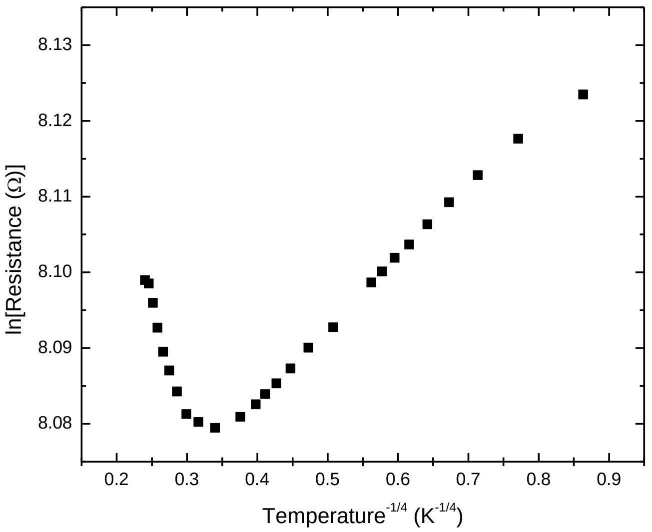

Figure 48. The ln(R) versus $T^{-1/4}$ plot for Sample C.

All three samples seemed to exhibit a linear section in the natural logarithm of the resistance versus temperature raised to the negative 1/4 power plot. This time, the temperature range for the linear section corresponded to temperatures between 10 K and 50 K. The 40 K temperature range seemed to be sufficient enough to attempt a three-dimensional Mott variable-range hopping fit for the data.

Using the parameters of the linear fit corresponding to temperatures between 10 K and 50 K. I plotted the data with the three-dimensional Mott variable-range hopping fit for each of the samples. Figure 49 shows the fitting results for Sample A. At values above 50 K, there is an obvious departure from the Mott variable-range hopping fit. At temperatures below 10 K, the shape of the curve fit is close to that of the data, but the resistance values do not match up. Based on the fitting equation for three-dimensional Mott variable-range hopping fit, $T_{Mott} = 8.2$ K for Sample A. It is at this point that an issue arises. As mentioned earlier, the average hopping length equation[37] is $\bar{R}_{Mott} = \frac{3}{8}\xi\left(\frac{T_{Mott}}{T}\right)^{1/4}$. This indicates that T_{Mott} should be larger than the temperatures for which Mott variable-range hopping is thought to occur in order to make any physical sense. Since T_{Mott} is less than T, the $\left(\frac{T_{Mott}}{T}\right)^{1/4}$ part of the average hopping length equation is less than one. As a result, the average hopping length is less than the localization length, which does not make physical sense. In this case, we are considering that Mott variable-range hopping is occurring at temperatures between 10 K and 50 K, and those temperatures are already above the calculated T_{Mott}. This would indicate that the average hopping length is less than the localization length, which in turn indicates that three-dimensional Mott variable-range hopping is not a likely explanation of the electrical transport data.

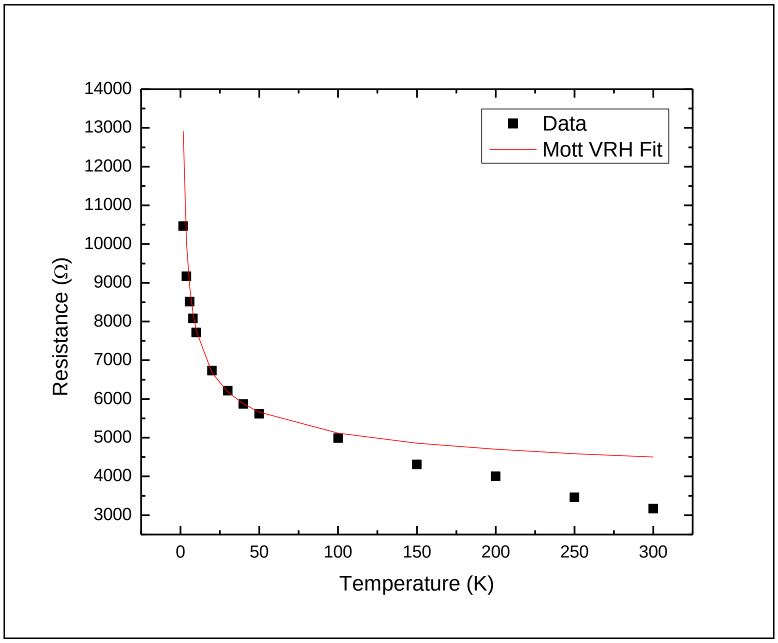

Figure 49. Three-dimensional Mott variable-range hopping fit in the 10 to 50 K range for Sample A.

Using the parameters from the linear fit of Sample B, I plotted the data with the three-dimensional Mott variable-range hopping fit in Figure 50. Similar to the previous sample, at values above 50 K, there is an obvious departure from the Mott variable-range hopping fit. Also, at temperatures below 10 K, the shape of the curve fit is close to that of the data, but the resistance values do not match up. Although the fit seems to follow the data trend a little better than the previous sample, again I end up with an unreasonable value for T_{Mott}, here $T_{Mott} = 0.03\ K$. Based on the same argument as before, the T_{Mott}, corresponding to an average hopping length which is less than the localization length, indicates that three-dimensional Mott variable-range hopping is not a likely explanation of the electrical transport data.

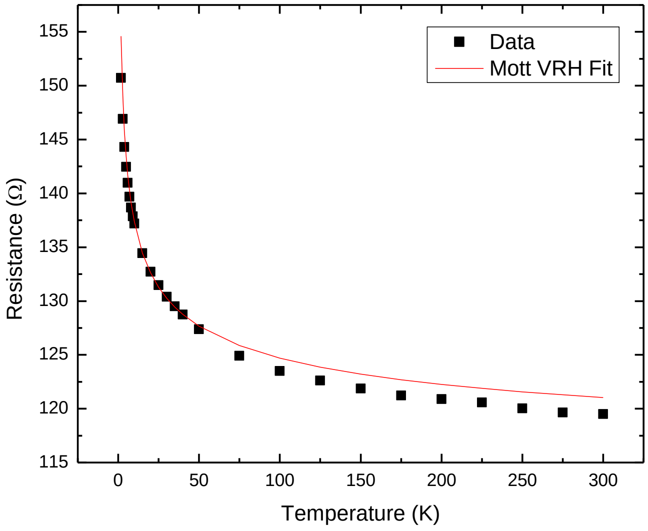

Figure 50. Three-dimensional Mott variable-range hopping fit in the 10 to 50 K range for Sample B.

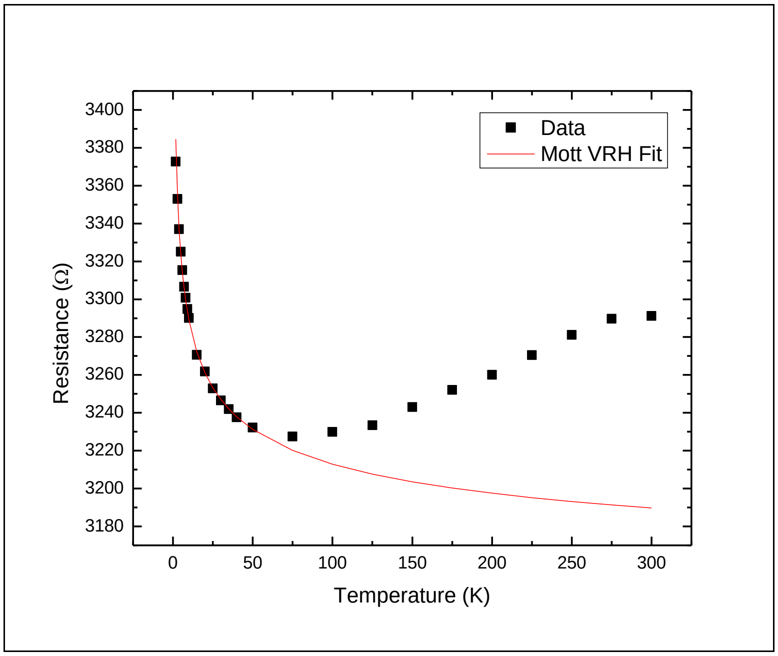

Figure 51. Three-dimensional Mott variable-range hopping fit in the 10 to 50 K range for Sample C.

Using the parameters from the linear fit of Sample C, I plotted the data with the three-dimensional Mott variable-range hopping fit in Figure 51. Similar to the previous two samples, at values above 50 K, there is an obvious departure from the Mott variable-range hopping fit. Also, at temperatures below 10 K, the shape of the curve fit is close to that of the data, but the resistance values do not match up. Again, I end up with a physically unreasonable value for T_{Mott}, here $T_{Mott} = 8.2 \cdot 10^{-5}\ K$. Based on the same argument as before, the T_{Mott}, corresponding to an average hopping length which is less than the localization length, indicates that three-dimensional Mott variable-range hopping is not a likely explanation of the electrical transport data.

Although the resistance versus temperature data appear to resemble the behavior of Mott variable-range hopping, the fits do not correspond to any physically reasonable values, and are therefore not thought to be a viable explanation of the data.

4.3.3 Efros-Shklovskii Variable-Range Hopping

The equation for Efros-Shklovskii variable-range hopping is given by

$$\rho(T) = \rho_{ES} \exp\left[\left(\frac{T_{ES}}{T}\right)^{\frac{3}{3+\mathrm{n}}}\right],$$

where $n = 1{,}2, or$ 3 refers to one, two, or three-dimensional variable-range hopping.[36] Since $R \propto \rho$, if one-dimensional Efros-Shklovskii variable-range hopping was the governing transport mechanism in the nanotubes, plotting the natural logarithm of the resistance as a function of the temperature raised to the negative 3/4 power would reveal a linear dependence. Figures 52, 53, and 54 show the ln(R) versus $T^{-3/4}$ plots for Samples A, B, and C, respectively. None of the samples exhibited a linear section in the natural logarithm of the resistance versus temperature to the negative 3/4 power plots, indicating that one-dimensional Efros-Shklovskii variable-range hopping was not likely the transport mechanism governing electrical conduction in the nanotubes.

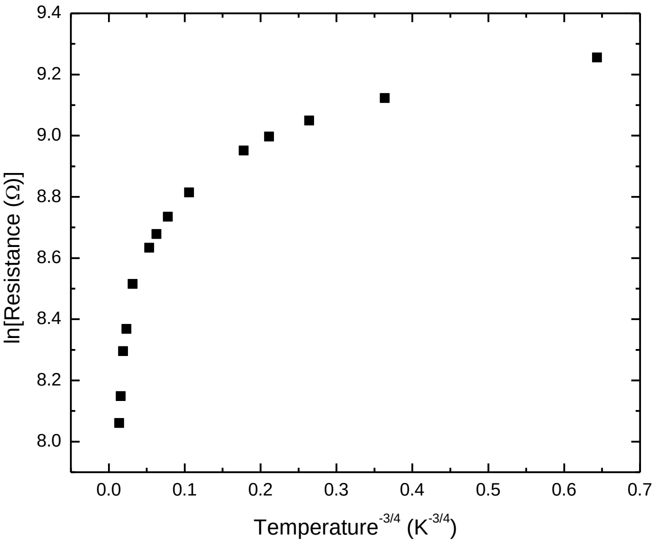

Figure 52. The ln(R) versus $T^{-3/4}$ plot for Sample A.

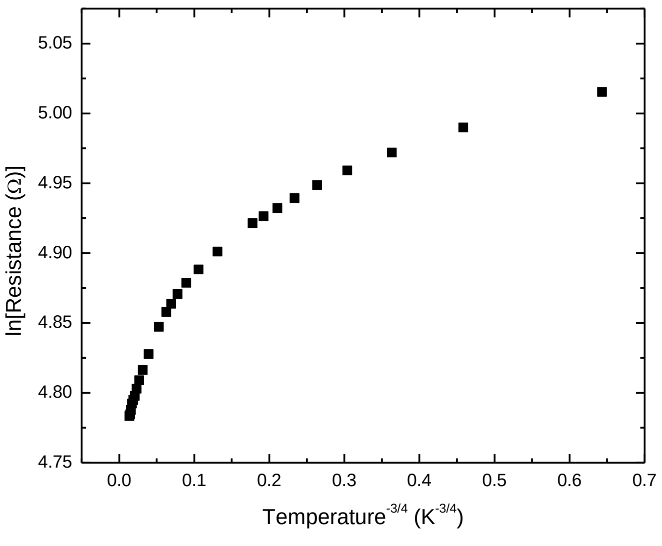

Figure 53. The ln(R) versus $T^{-3/4}$ plot for Sample B.

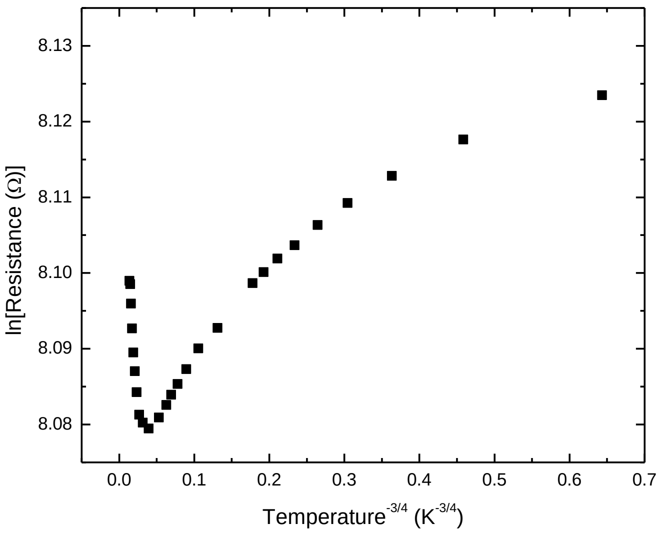

Figure 54. The ln(R) versus $T^{-3/4}$ plot for Sample C.

Based on the same equation, if two-dimensional Efros-Shklovskii variable-range hopping was the governing transport mechanism in the nanotubes, plotting the natural logarithm of the resistance as a function of the temperature raised to the negative 3/5 power would reveal a linear dependence. Figures 55, 56, and 57 show the ln(R) versus $T^{-3/5}$ plots for Samples A, B, and C, respectively. None of the samples exhibited a linear section in the natural logarithm of the resistance versus temperature to the minus 3/5 power plots, indicating that two-dimensional Efros-Shklovskii variable-range hopping was not likely the transport mechanism governing electrical conduction in the nanotubes.

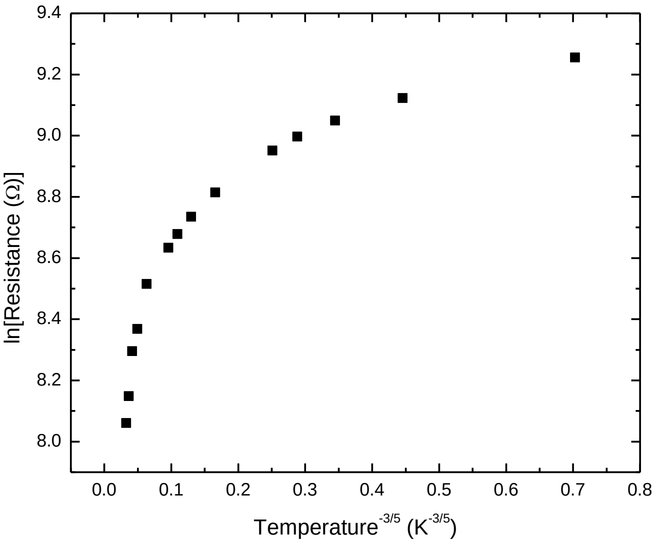

Figure 55. The ln(R) versus $T^{-3/5}$ plot for Sample A.

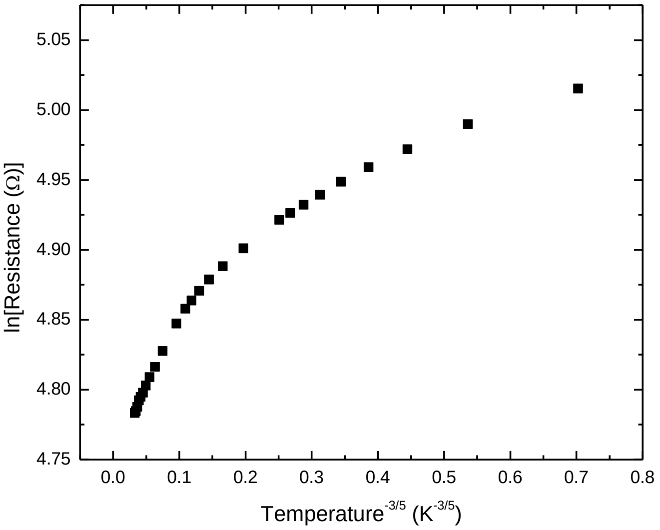

Figure 56. The ln(R) versus $T^{-3/5}$ plot for Sample B.

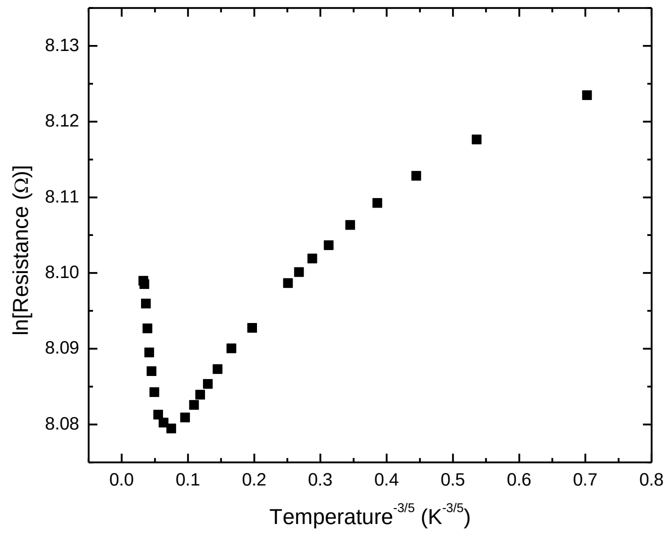

Figure 57. The ln(R) versus $T^{-3/5}$ plot for Sample C.

Based on the same equation, if three-dimensional Efros-Shklovskii variable-range hopping was the governing transport mechanism in the nanotubes, plotting the natural logarithm of the resistance as a function of the temperature raised to the negative 1/2 power would reveal a linear dependence. However, that would correspond to the same plots as those for one-dimensional Mott variable-range hopping since both have a $T^{-1/2}$ dependence. It has already been shown that none of the samples exhibited a linear section in the natural logarithm of the resistance versus temperature to the minus 1/2 power plots, indicating that three-dimensional Efros-Shklovskii variable-range hopping was not likely the transport mechanism governing electrical conduction in the nanotubes.

4.4. Best Fit Equations

Since I could not find a decent fit with any of the preexisting models, I decided to try to fit my data to an equation of the form $R = R_0 \exp[(T_0/T)^S]$. Here R_0 is a temperature independent pre-exponential factor, T_0 is the characteristic temperature, and S is some fractional exponent. Like the model used by Finlayson and Mason,[61] I let the variables R_0, T_0, and S be adjustable parameters in order to find the best fit.

The optimized fit for Sample A is shown in Figure 58. For sample A, $R_0 = 7.7 * 10^{-79}$ Ω, $T_0 = (190)^{1000}$ K, and $S = 0.001$. As seen from the figure, for temperatures below 50 K, the fitting equation is a good fit. I was not able to find a fit for the whole range of the data. In order to assess the quality of the fit, I used a model proposed by Finlayson and Mason to calculate the percent deviation.[61] Here the percent deviation is given by the equation,

$$\%\ \text{deviation} = \left[\frac{1}{n}\sum_{i=1}^{n}\frac{100}{R_i}(R - R_i)^2\right]^{1/2}. \qquad \textbf{(61)}$$

Since the fit deviates from the data above $T = 50$ K, I only calculated the percent deviation for temperatures below 50 K. For Sample A, the percent deviation between the data and the optimized equation for temperatures below 50 K, is 6 %.

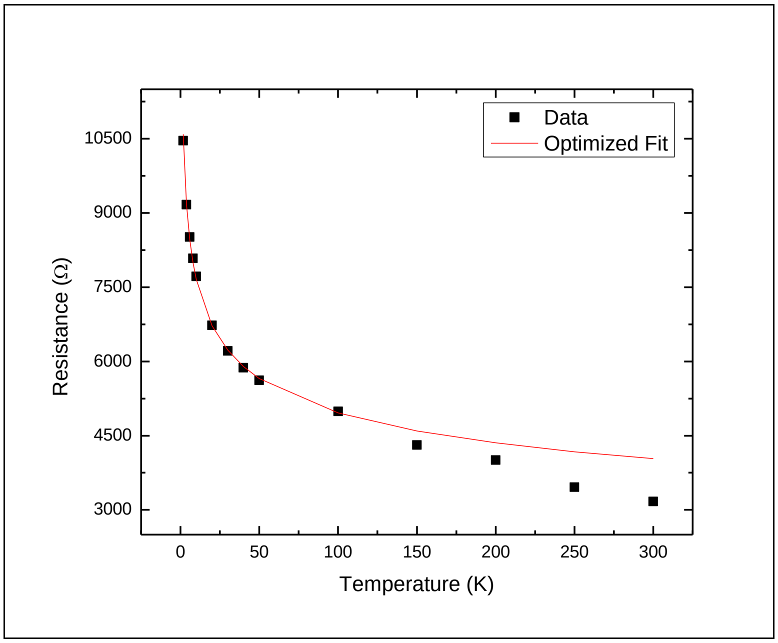

Figure 58. The optimized fit for sample A.

The optimized fit for Sample B is shown in Figure 59. For Sample B, $R_0 = 91\ \Omega$, $T_0 = 9.7 * 10^{-3}$ K, and $S = 0.13$. As seen from the figure, the fitting equation appears to be a good fit across the whole range of temperatures. For this sample, since the fit appears to be a good fit across the whole range of temperatures, I used the whole temperature range to calculate the percent deviation. For Sample B, the percent deviation between the data and the optimized equation, is 0.2 %.

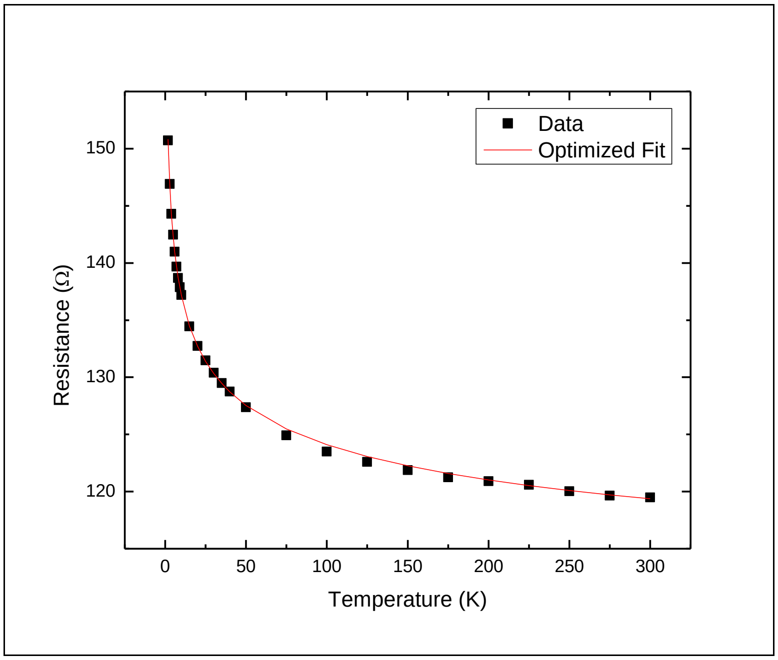

Figure 59. The optimized fit for Sample B.

The optimized fit for Sample C is shown in Figure 60. For Sample C, $R_0 = 3.0\ \text{k}\Omega$, $T_0 = 8.6 * 10^{-7}$ K, and $S = 0.15$. As seen from the figure, the fitting equation appears to be a good fit only for temperatures below 50 K. I was not able to find a good fit across the whole range of the data. Since the fit deviates from the data, I only calculated the percent deviation for temperatures below 50 K. For Sample C, the percent deviation between the data and the optimized equation for temperatures below 50 K, is 0.3 %.

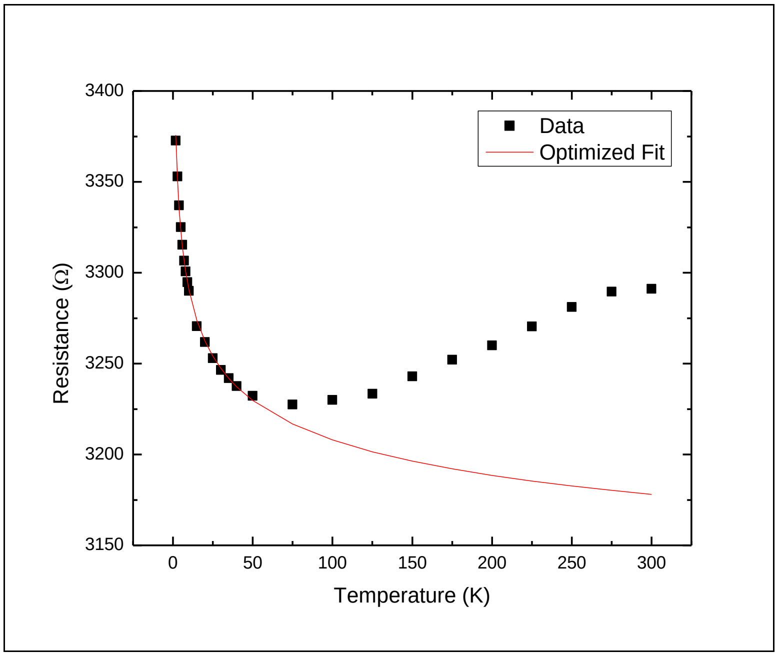

Figure 60. The optimized fit for Sample C.

It should be noted that these fits do not seem to produce reasonable physical parameters, especially the characteristic temperature T_0. They are not likely to be relevant to the transport mechanism. Although there is not currently a transport model with the fitting equations with any of the exponents I have found, the information could be useful in the future.

4.5. Resistance as a Function of the Natural Logarithm of Temperature

As mentioned earlier, due to the fragility of the samples, I only have three complete sets of data. Since each sample shows differing results, more samples are needed to determine a systematic pattern of behavior for these nanotubes. Due to the differences in results for each measurement, it is difficult to say with certainty what amount of error is due to the limited sample size. However, independent of the sample size, there are some similarities in the samples which can be used to draw reasonable conclusions.

In an attempt to understand the temperature dependent resistance data, I plotted the data in various forms. One interesting form was resistance as a function of the natural logarithm of temperature. Figures 61, 62, and 63 show the results for Samples A, B, and C, respectively. The data points representing the resistance from 1.8 K to 10 K seem to have a linear dependence on the natural logarithm of temperature. I plotted the linear fit to show the departure from the linear dependence at temperatures above 10 K. To analyze the linear fits, I considered the coefficient of determination R^2. The coefficient of determination is given by

$$R^2 = \left[\frac{1}{N}\sum \frac{(x_i - \bar{x})(y_i - \bar{y})}{\sigma_x \sigma_y}\right]^2, \quad \textbf{(62)}$$

and indicates how much of the variability in the data is accounted for by the regression model. In the R^2 equation N represents the number of observations used to fit the model, x_i is the x value for observation i, $\bar{x}$ is the average x value, σ_x is the standard deviation of x, and likewise for the y variable. The values for R^2 vary between 0 and 1, with a value close to 1 indicating a good linear fit. A value of 0.99 indicates that 99 % of the variance in the dependent variable is predictable by the model. Between 1.8 K and 10 K, the coefficient of determination was greater than 0.99 for each of the proceeding linear fits, indicating a good fit by the regression model.

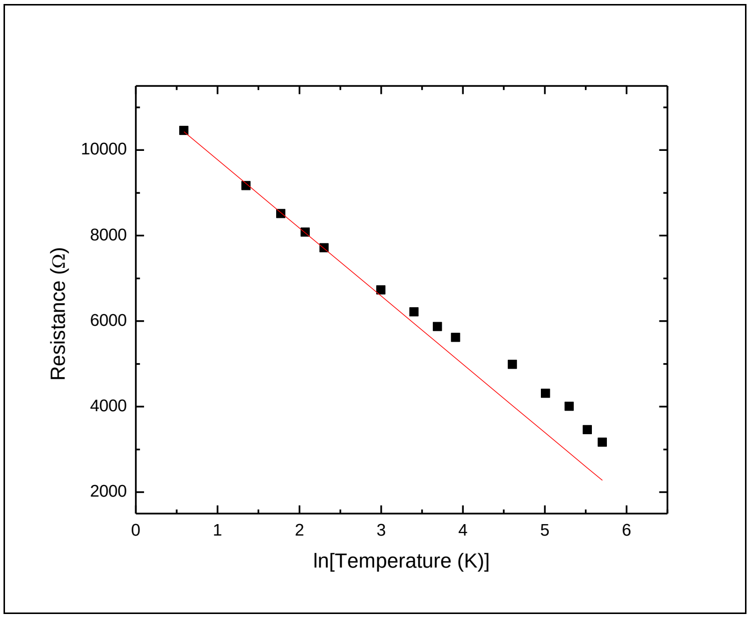

Figure 61. The R versus ln(T) plot for Sample A. The black squares represent the actual data points and the red line is the linear fit connecting the points between 1.8 K and 10 K.

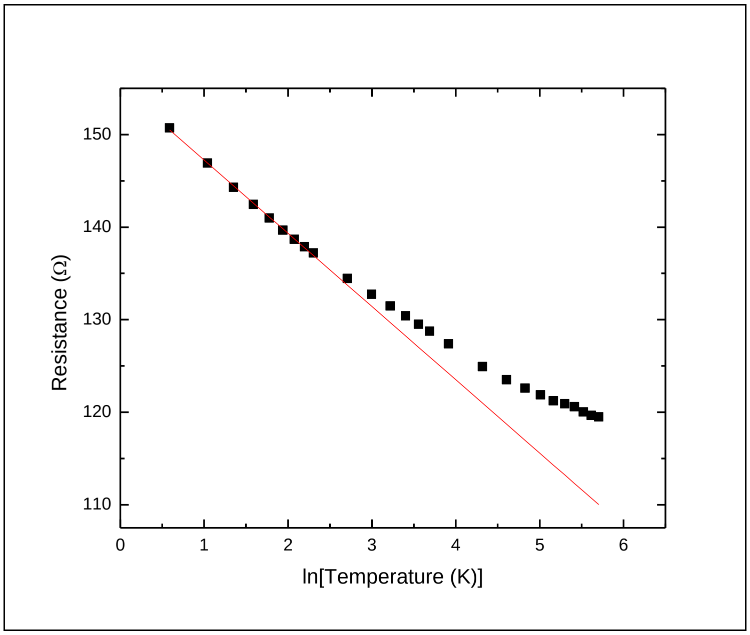

Figure 62. The R versus ln(T) plot for Sample B. The black squares represent the actual data points and the red line is the linear fit connecting the points between 1.8 K and 10 K.

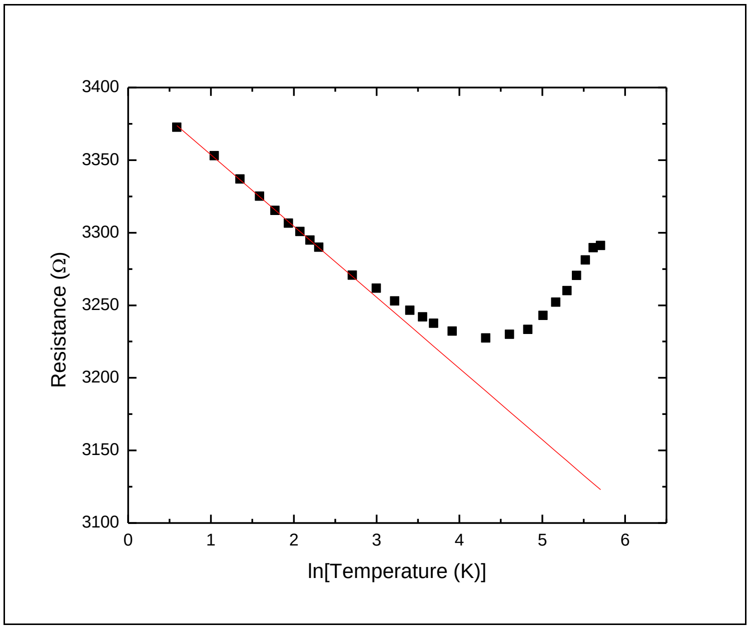

Figure 63. The R versus ln(T) plot for Sample C. The black squares represent the actual data points and the red line is the linear fit connecting the points between 1.8 K and 10 K.

It is interesting that for each of these samples the resistance appears to show a linear dependence on the natural logarithm of temperature for temperatures below 10 K. Also, the sample with lowest RRR value had the steepest slope in the linear fit, while the sample with the highest RRR value had the mildest slope. This indicates that the effect is larger in samples with a higher level of disorder.

There are two mechanisms known to cause a linear dependence on the natural logarithm of temperature, and they are weak localization and electron-electron interactions in two dimensional samples.

In order to distinguish between the weak localization and electron-electron interaction in two-dimensional samples as the origin of the observed ln(T) behavior,[22] the magnetoresistance data need to be analyzed. For weak localization, if the applied magnetic field introduces a flux through the self-intersecting electron paths, the self-interference contribution to the resistivity is destroyed, resulting in a negative magnetoresistance.[22] In two dimensions, a negative magnetoresistance would show up for the perpendicular orientation, but not for the parallel orientation since a parallel field does not introduce a flux through the self-intersecting electron paths. On the other hand, if electron-electron interaction is the mechanism, the effect of a magnetic field is to align the spins to the magnetic field by the Zeeman effect, resulting in a positive, isotropic magnetoresistance.[15,22]

4.6. Resistance versus Magnetic Field

When I mounted the samples into the PPMS, I used the rotating puck mount so that I could rotate the samples in order to align the axis of the nanotube to be either parallel or perpendicular to the direction of the magnetic field. For the following measurements, I swept the magnetic field from +5 T to -5 T. The magnetic field was scanned at a rate of 50 Oe/s, and data were taken in increments of 500 Oe. I also wanted to see how temperature affected the magnetoresistance so data were taken at 1.8 K, 3 K, 4 K, 6 K and 10 K. As mentioned earlier, all the resistance measurements from the PPMS have a percent error of less than 0.5 %. However, due to the propagation of errors, the magnetoresistance plots all have much more noticeable error bars. In some cases, including those error bars would result in practically unreadable plots (see Figure

64). For the sake of clarity, the error bars are not included in any of the following magnetoresistance plots.

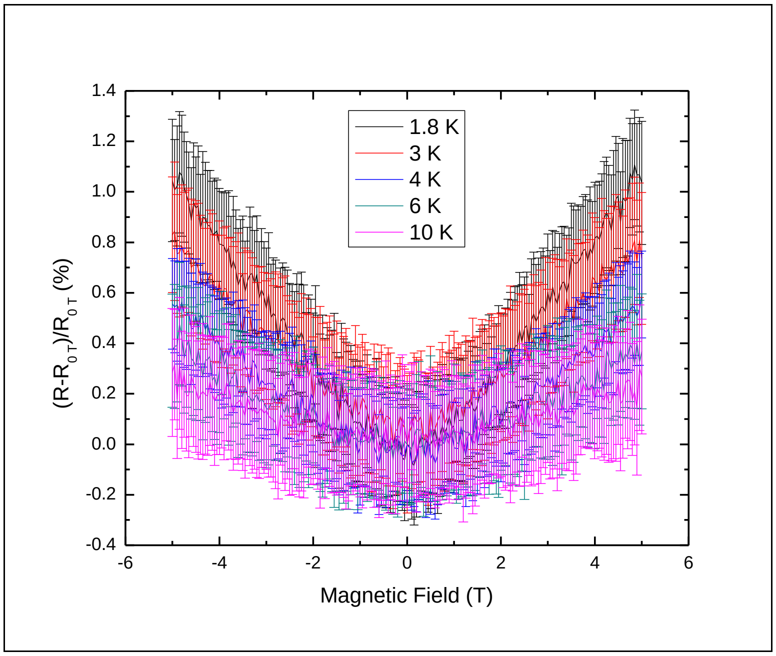

Figure 64. Magnetoresistance versus magnetic field plot for Sample B with error bars. The direction of the magnetic field is parallel to the axis of the nanotube.

4.6.1 Parallel Orientation

For the first set of data, I rotated the nanotube so that the axis of the nanotube was parallel to the direction of the magnetic field. Figure 65 shows the magnetoresistance versus magnetic field results for Sample A. The magnetoresistance is plotted as a percentage, which means it is given by $[(R - R_{0\,T})/R_{0\,T}] * 100$. As seen in the figure, as the temperature decreased, the total change in magnetoresistance increased.

The maximum change in magnetoresistance was 4.4 % at 1.8 K, 2.8 % at 3 K, 2.1 % at 4 K, 1.2 % at 6 K and 0.5 % at 10 K.

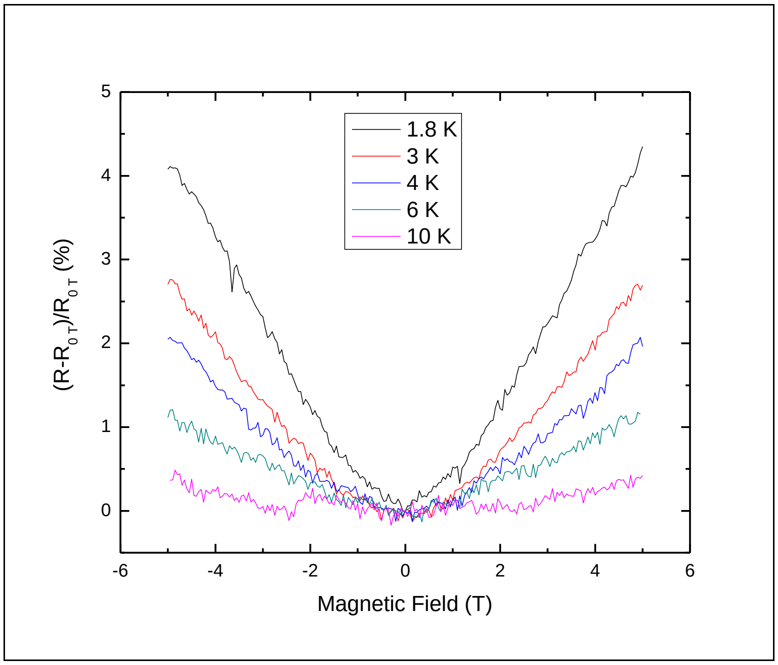

Figure 65. Normalized change in resistance versus magnetic field for Sample A. The axis of the nanotube is parallel to the magnetic field. Data were taken at 1.8 K, 3 K, 4 K, 6 K, and 10 K.

Figure 66 shows the magnetoresistance versus magnetic field results for Sample B. Again, for this measurement the axis of the nanotube is parallel to the magnetic field. For Sample B the maximum change in magnetoresistance was 1.1 % at 1.8 K, 0.84 % at 3 K, 0.59 % at 4 K, 0.48 % at 6 K and 0.32 % at 10 K.

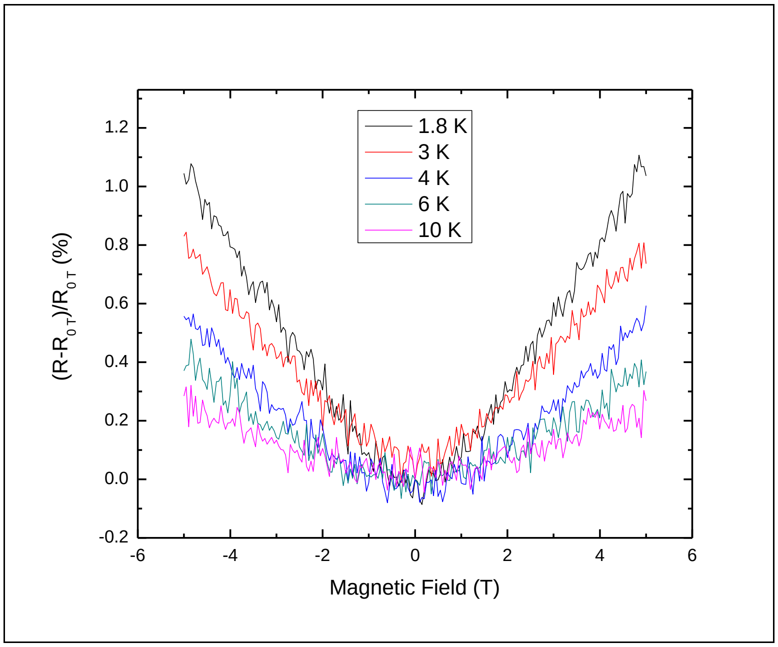

Figure 66. Normalized change in resistance versus magnetic field for Sample B. The axis of the nanotube is parallel to the magnetic field. Data were taken at 1.8 K, 3 K, 4 K, 6 K, and 10 K.

For Sample C, the same settings were used as in previous measurements, and the results are presented in Figure 67. For Sample C, the maximum change in magnetoresistance was 0.63 % at 1.8 K, 0.45 % at 3 K, 0.41 % at 4 K, 0.29 % at 6 K and 0.17 % at 10 K.

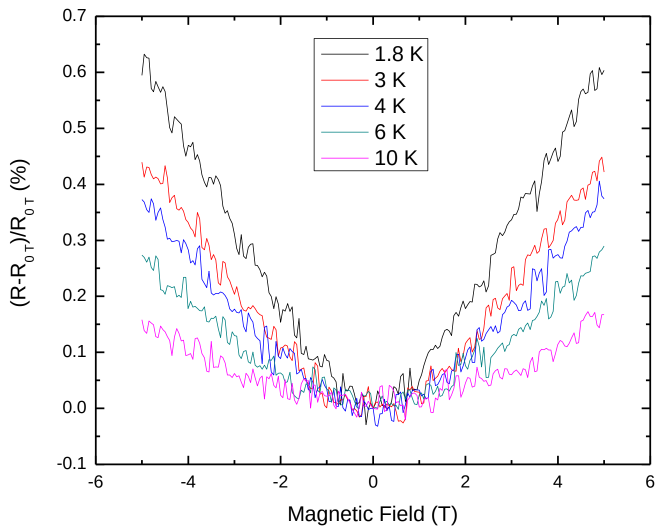

Figure 67. Normalized change in resistance versus magnetic field for Sample C. The axis of the nanotube is parallel to the magnetic field. Data were taken at 1.8 K, 3 K, 4 K, 6 K, and 10 K.

4.6.2 Perpendicular Orientation

For the next set of measurements, I rotated the nanotube so that the axis of the nanotube was perpendicular to the direction of the magnetic field. All the other conditions remained unchanged. Figure 68 shows the magnetoresistance versus magnetic field results for Sample A. From this plot, we see that the results are similar to their parallel counterpart, but the change in magnetoresistance is just slightly larger. For the perpendicular orientation, the maximum change in magnetoresistance was 5.2 % at 1.8 K, 3.2 % at 3 K, 2.5 % at 4 K, 1.5 % at 6 K and 0.86 % at 10 K.

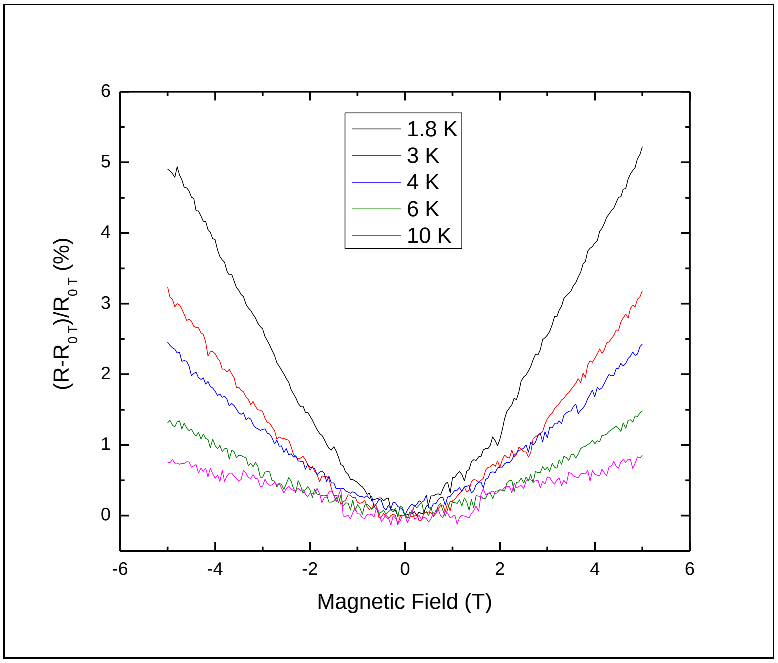

Figure 68. Normalized change in resistance versus magnetic field for Sample A. The axis of the nanotube is perpendicular to the magnetic field. Data were taken at 1.8 K, 3 K, 4 K, 6 K, and 10 K.

The same measurements were carried out on Sample B, and those results are presented in Figure 69. For Sample B the maximum change in magnetoresistance was 1.5 % at 1.8 K, 0.95 % at 3 K, 0.83 % at 4 K, 0.53 % at 6 K and 0.33 % at 10 K.

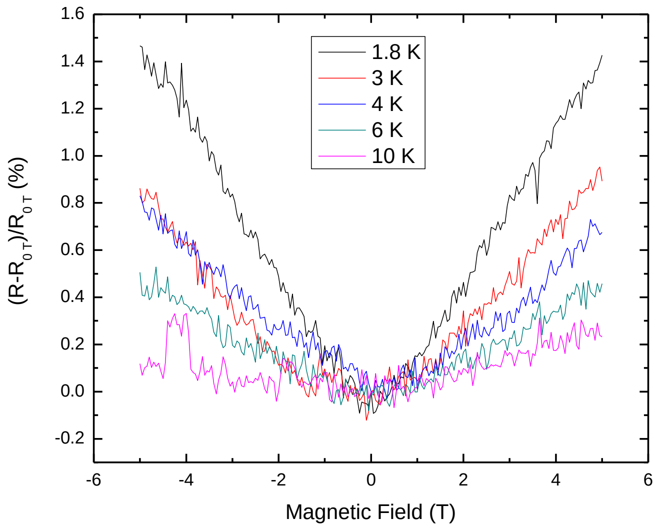

Figure 69. Normalized change in resistance versus magnetic field for Sample B. The axis of the nanotube is perpendicular to the magnetic field. Data were taken at 1.8 K, 3 K, 4 K, 6 K, and 10 K.

Sample C was measured using the same settings as Samples A and B. Those results are shown in Figure 70. For Sample C, the maximum change in magnetoresistance was 0.66 % at 1.8 K, 0.53 % at 3 K, 0.42 % at 4 K, 0.33 % at 6 K and 0.18 % at 10 K.

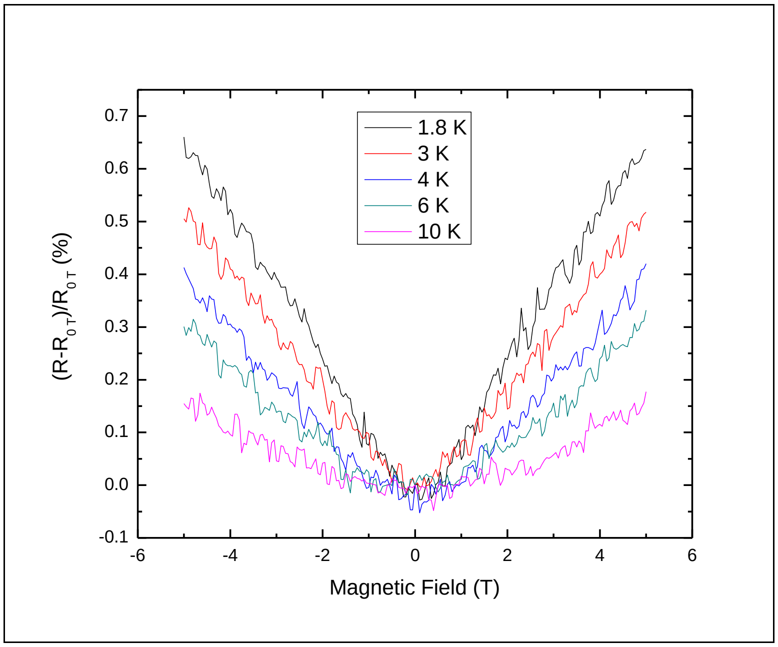

Figure 70. Normalized change in resistance versus magnetic field for Sample C. The axis of the nanotube is perpendicular to the magnetic field. Data were taken at 1.8 K, 3 K, 4 K, 6 K, and 10 K.

There are several similarities in the magnetoresistances of the samples regardless of the nanotube orientation with respect to the direction of the magnetic field. For all three samples, the magnetoresistance is positive in the range from -5 T to +5 T. Also, in each case, the magnetoresistance decreases as the temperature increases. Additionally, the sample with the highest amount of disorder seems to produce the largest magnetoresistance; while the sample with the lowest amount of disorder seems to produce the smallest magnetoresistance.

In the whole range of data, the magnetoresistance is positive, whereas weak localization would result in a negative magnetoresistance. The magnetoresistance exists in both the parallel and perpendicular orientations and appears to have relatively close values. Both of these conditions rule out weak localization as an explanation for the results. Since the magnetoresistance due to electron-electron interaction produces a positive, isotropic magnetoresistance,[15,22] then electron-electron interaction seems to be a better explanation of the results. The limitation to this conclusion is that it only applies to the small temperature range below 10 K, above which the magnetoresistance becomes nearly unmeasurable.

In order for a sample to be considered two dimensional, one of its dimensions must be smaller than the electron-electron interaction length. The electron-electron interaction length is approximately $L_{ee} \sim v_F \tau_{ee} \sim v_F \hbar / k_B T$. As an estimate for my samples, at 10 K, the interaction length is approximately 1 micron; while at 1.8 K, the interaction length is approximately 4 microns long. Since the wall thickness of my nanotube is about 17 nm, my nanotube would be considered a two-dimensional sample, and the natural logarithm of temperature dependence for two-dimensional samples is appropriate.

4.7. Scaled Magnetoresistance

The scaled magnetoresistance is given by the ratio $(R - R_{0\,T})/(R_{5\,T} - R_{0\,T})$, and its purpose is to normalize the magnetoresistance to 1 at 5 T. It is interesting to note that scaling the magnetoresistance, seems to result in all the curves collapsing into a single curve.

4.7.1 Parallel Orientation

In Figures 71, 72, and 73, scaled magnetoresistances are shown for Samples A, B, and C, respectively, with the axis of the nanotube aligned parallel to the direction of the magnetic field. At 10 K, the magnetoresistance is the smallest, and therefore the scaling results in an amplification of the noise. As seen in the figures, all the curves seem to collapse into a single curve for each of the three samples.

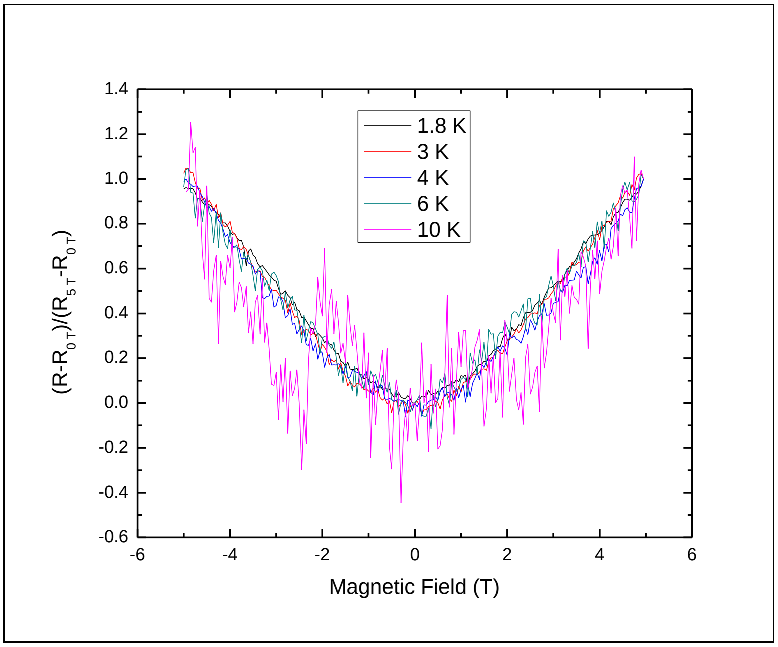

Figure 71. Scaled magnetoresistance versus magnetic field for Sample A. The axis of the nanotube is parallel to the magnetic field. Data were taken at 1.8 K, 3 K, 4 K, 6 K, and 10 K.

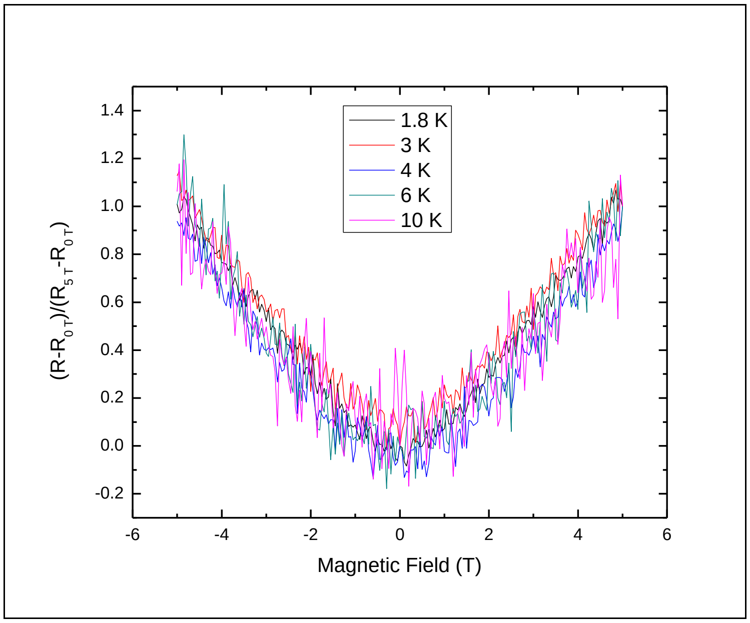

Figure 72. Scaled magnetoresistance versus magnetic field for Sample B. The axis of the nanotube is parallel to the magnetic field. Data were taken at 1.8 K, 3 K, 4 K, 6 K, and 10 K.

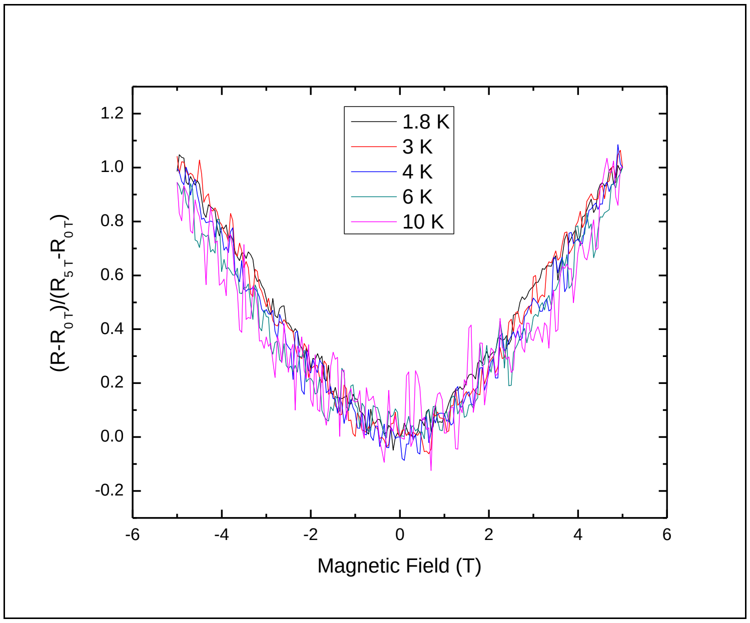

Figure 73. Scaled magnetoresistance versus magnetic field for Sample C. The axis of the nanotube is parallel to the magnetic field. Data were taken at 1.8 K, 3 K, 4 K, 6 K, and 10 K.

4.7.2 Perpendicular Orientation

In Figures 74, 75, and 76, scaled magnetoresistances are shown for samples A, B, and C, respectively with the axis of the nanotube aligned perpendicular to the direction of the magnetic field.

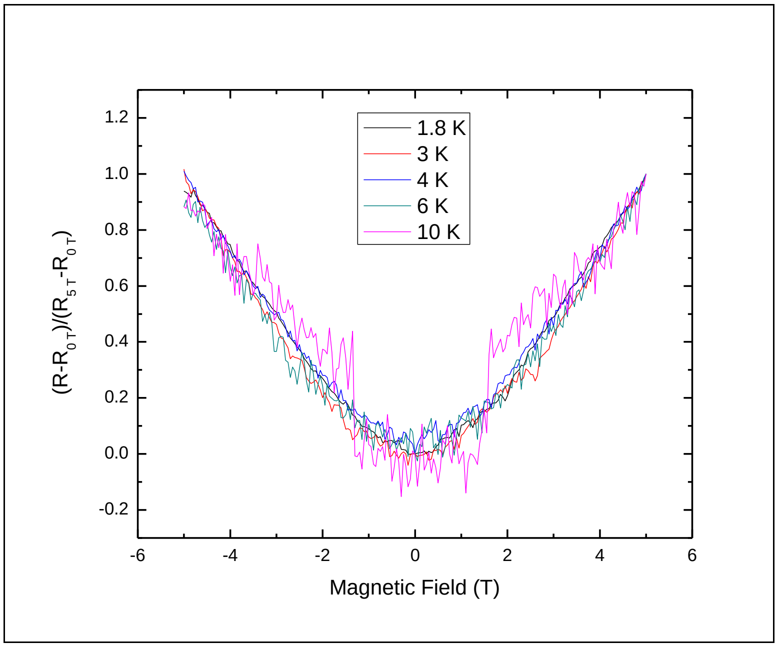

Figure 74. Scaled magnetoresistance versus magnetic field for Sample A. The axis of the nanotube is perpendicular to the magnetic field. Data were taken at 1.8 K, 3 K, 4 K, 6 K, and 10 K.

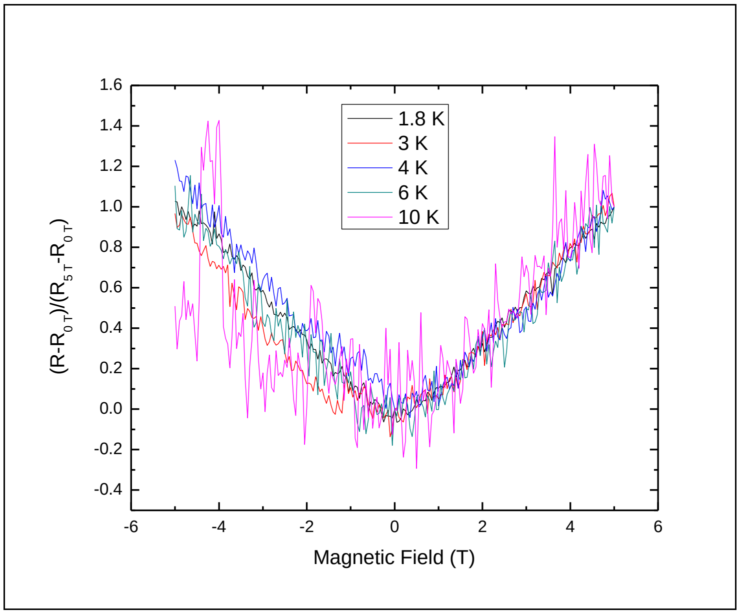

Figure 75. Scaled magnetoresistance versus magnetic field for Sample B. The axis of the nanotube is perpendicular to the magnetic field. Data were taken at 1.8 K, 3 K, 4 K, 6 K, and 10 K.

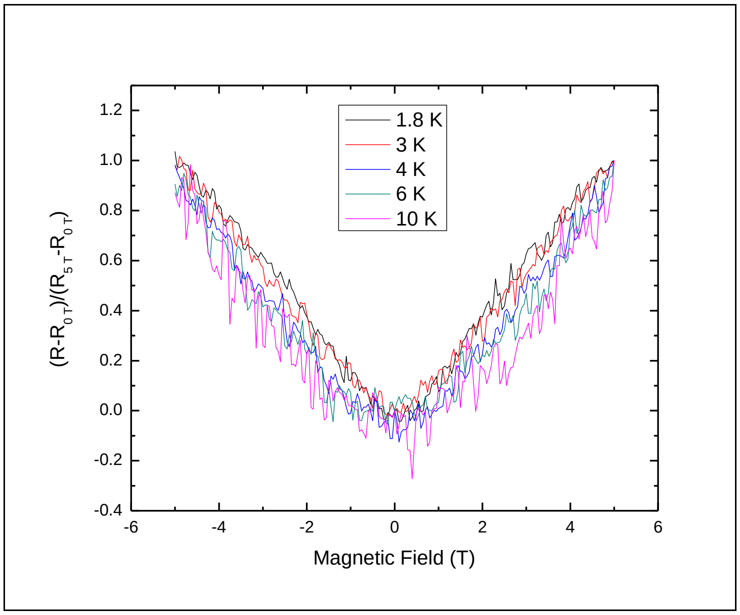

Figure 76. Scaled magnetoresistance versus magnetic field for Sample C. The axis of the nanotube is perpendicular to the magnetic field. Data were taken at 1.8 K, 3 K, 4 K, 6 K, and 10 K.

The scaled magnetoresistance plots in the perpendicular orientation also show a trend in which below 10 K, all the curves appear to collapse into a single curve. This seems to suggest that the magnetoresistance appears to have a contribution which is independent of the temperature. In other words, the magnetoresistance can be expressed as $\mathrm{R}(T, H) = f(T) \cdot g(H)$, where $g(H)$ is given by the scaled function. This is the second significant feature observed in these nanotubes.

Although one may be concerned with the limited number of samples measured in this work thus far, an identical magnetoresistance feature appears in all these samples in a robust manner. The scaled magnetoresistance effect is also observable below 10 K, a temperature at which the natural logarithmic temperature dependence emerges, which may indicate a correlation between the magnetoresistance and the ln(T) resistance dependence. The positive isotropic behavior of the magnetoresistance supports the interpretation of an alignment of the spins by the magnetic field, and not one caused by electrons traveling around a loop. This in turn, supports two-dimensional electron-electron interaction as the origin of the observed linear dependence in the resistance as a function of the natural logarithm of temperature plot. The observation of the separation of the magnetoresistance into $\mathrm{R}(T, H) = f(T) \cdot g(H)$ is particularly interesting, but not yet understood. Is it possible that at higher temperatures $g(H)$ is due to the spin splitting, while the $f(T)$ part is due to the interference between the electrons since $L_{ee} \sim \sqrt{\hbar D / T} = v_F \sqrt{\hbar \tau / T}$, which is not apparently dependent on H?

5. CONCLUSIONS

In conclusion, I have used two different types of porous membranes as templates for nanotube growth. For one of those types of templates, anodized aluminum oxide membranes, I fabricated them myself in order to obtain uniform spacing between the pores and a more ordered structure. I also fabricated insulating, magnetic, metallic and metal-insulator composite nanotubes. Once I obtained silver-stannic oxide composite nanotubes that were long enough for measurement, I connected them for transport measurements using a four-point probe setup to eliminate the contact resistances of the leads.

I have done transport and magnetoresistance measurements on silver-stannic oxide composite nanotubes of various lengths at low temperatures. I measured the resistance as a function of temperature from 300 K down to 1.8 K. At temperatures between 1.8 K and 10 K I found that the resistance had a linear dependence on the natural logarithm of temperature.

At low temperatures I measured the current – voltage curves for each of the samples. Only the sample with the highest level of disorder showed non-linear curves at temperatures below 4 K. The non-linearity of the current – voltage curves was not very pronounced and disappeared at temperatures above 4 K. The other samples with lower levels of disorder had linear current – voltage curves for all the temperatures measured.

I also did magnetoresistance measurements on the nanotubes at 1.8 K, 3 K, 4 K, 6 K and 10 K. All of the samples had positive magnetoresistance which appeared to be independent of the angle between the axis of the nanotube and the direction of the magnetic field. At these low temperatures, scaling the magnetoresistance resulted in magnetoresistance values that seem to collapse into a single curve independent of temperature.

Although the two-dimensional weak localization and two-dimensional electron-electron interactions both produce a linear dependence on the natural logarithm of temperature for resistance measurements, I was able to rule out weak localization due to the positive and isotropic magnetoresistance results.

I also tried Mott variable-range hopping fits for temperatures between 10 K and 50 K, but those mechanisms were ultimately ruled out because the results lead to unrealistic physical parameters. At temperatures above 50 K, the resistance as a function of temperature seems to vary depending on the amount of disorder in the sample.

As far as future work is concerned, it would be useful to know the fraction of the total volume occupied by the silver grains in my nanotubes. Also, other experiments could be done in order to confirm the existence of electron-electron interactions. Tunneling experiments could be carried out to analyze the density of states. A density of states minimum would be found at the Fermi level if the effect of electron-electron interactions dominates conduction at low temperatures. It would also be interesting to study a wide array of silver concentrations in the nanotubes, to see how the transport measurements are affected.

REFERENCES

[1] C. Kittel, *Introduction to Solid State Physics*, 8 ed. (Wiley, Hoboken, NJ, 2005).

[2] R. A. Matula, J. Phys. Chem. Ref. Data **8** (4), 1147 (1979).

[3] F. Bloch, Z. Phys. **59**, 208 (1930).

[4] E. Gruneisen, Ann. Phys. **16** (5), 530 (1933).

[5] N. W. Ashcroft and N. D. Mermin, *Solid State Physics*. (Holt, Rinehart and Winston, New York, 1976).

[6] P. W. Anderson, E. Abrahams, and T. V. Ramakrishnan, Phys. Rev. Lett. **43** (10), 718 (1979).

[7] H. Ibach and H. Luth, *Solid State Physics: An Introduction to Principles of Materials Science*, 4 ed. (Springer, New York, 2009).

[8] V. F. Gantmakher, *Electrons and Disorder in Solids*. (Clarendon Press, Oxford, 2005).

[9] R. Webb and S. Washburn, Phys. Today **41** (12), 46 (1988).

[10] D. K. Ferry, S. M. Goodnick, and J. Bird, *Transport in Nanostructures*, 2nd ed. (Cambridge University Press, New York, 2009).

[11] P. B. Allen, in *Quantum Theory of Real Metals*, edited by J. R. Chelikowsky and S. G. Louie (Kluwer Academic Publishers, Norwell, Massachusetts, 1996), pp. 219-250.

[12] B. L. Altshuler and A. G. Aronov, in *Electron-Electron Interactions in Disordered Systems*, edited by A. L. Efros and M. Pollack (North-Holland, New York, 1985).

[13] A. V. Germanenko, Low Temp. Phys. **35** (1), 24 (2009).

[14] T. Schapers, in *Nanotechnology*, edited by R. Waser (Wiley-VCH, Weinheim, 2008), Vol. 3.

[15] I. Zvyagin, in *Charge Transport in Disordered Solids with Applications in Electronics*, edited by S. Baranovski (Wiley, Chichester, England, 2006), pp. 1-47.

[16] L. P. Gorkov, A. I. Larkin, and D. E. Khmelnitshkii, JETP Lett. **30** (4), 228 (1979).

[17] L. Van den dries, C. Van Haesendonck, Y. Bruynseraede, and G. Deutsher, Phys. Rev. Lett. **46** (8), 565 (1981); G. J. Dolan and D. D. Osheroff, Phys. Rev. Lett. **43** (10), 721 (1979).

[18] G. Bergmann, Phys. Rep. **107** (1), 1 (1984).

[19] Z. Ovadyahu and Y. Imry, Phys. Rev. B **24** (12), 7439 (1981).

[20] H. Ibach and H. Luth, (Springer Berlin Heidelberg, 2009).

[21] B. Kramer and A. MacKinnon, Rep. Prog. Phys. **56**, 1469 (1993).

[22] P. A. Lee and T. V. Ramakrishnan, Rev. Mod. Phys. **57** (2), 287 (1985).

[23] D. J. Bishop, R. C. Dynes, and D. C. Tsui, Phys. Rev. B **26** (2), 773 (1982).

[24] S. Bansal, S. C. Kashyap, and D. K. Pandya, J. Alloys Compounds **646**, 483 (2015).

[25] B. L. Altshuler, A. G. Aronov, and P. A. Lee, Phys. Rev. Lett. **44** (19), 1288 (1980).

[26] B. L. Altshuler and A. G. Aronov, Solid State Comm. **38**, 11 (1981).

[27] B. L. Altshuler, A. G. Aronov, and D. E. Khmelnitsky, J. Phys. C: Solid State Phys. **15**, 7367 (1982).

[28] A. Yildiz, N. Serin, T. Serin, and M. Kasap, Jpn. J. Appl. Phys **48**, 111203 (2009).

[29] C. J. Adkins, J. Phys.: Condens. Matter **1** (7), 1253 (1989).

[30] N. F. Mott, J. Non-Cryst. Solids **1**, 1 (1968).

[31] B. I. Shklovskii and A. L. Efros, *Electronic Properties of Doped Semiconductors*. (Springer, New York, 1984).

[32] A. Yildiz, S. B. Lisesivdin, M. Kasap, and D. Mardare, Optoelect. Adv. Mater. **1** (10), 531 (2007).

[33] M. Pollack, Discuss. Faraday So. **50**, 13 (1970).

[34] Y. Z. Long, J. L. Duvail, Z. J. Chen, A. Z. Jin, and C. Z. Gu, Chin. Phys. Lett. **25** (9), 3474 (2008).

[35] A. L. Efros and B. I. Shklovskii, J. Phys. C: Solid State Phys. **8**, 49 (1975).

[36] E. R. Viana, J. C. Gonzalez, G. M. Ribeiro, and A. G. de Oliveira, Phys. Status Solidi RRL **6** (6), 262 (2012).

[37] R. Rosenbaum, Phys. Rev. B. **44** (8), 3599 (1991).

[38] R. Rosenbaum, N. V. Lien, M. R. Graham, and M. Witcom, J. Phys.: Condens. Matter **9**, 6247 (1997).

[39] H. Liu, A. Pourret, and P. Guyot-Sionnest, ACS Nano **4** (9), 5211 (2010).

[40] R. Kassing and W. Kulisch, in *Functional Properties of Nanostructured Materials*, edited by R. Kassing, P. Petkov, W. Kulisch et al. (Springer, Netherlands, 2006), pp. 3-26.

[41] P. Sheng, Phil. Mag. B **65** (3), 357 (1992).

[42] B. Abeles, P. Sheng, M. D. Coutts, and Y. Arie, Adv. Phys. **24**, 407 (1975).

[43] Y. F. Wei and Z. Q. Li, Appl. Phys. Lett. **102**, 131911 (2013).

[44] J. D. Edwards and F. Keller, Trans. Electrochem. Soc. **79**, 135 (1941).

[45] F. Keller, M. S. Hunter, and D. L. Robinson, J. Electrochem. Soc. **100** (9), 411 (1953).

[46] H. Masuda and K. Fukuda, Science **268**, 1466 (1995).

[47] H. Imai, Y. Takei, K. Shimizu, M. Matsuda, and H. Hirashima, J. Mater. Chem. **9** (12), 2971 (1999).

[48] W. Lee, R. Scholz, K. Nielsch, and U. Gosele, Angew. Chem. Int. Ed. **44** (37), 6050 (2005).

[49] B. Bercu, I. Enculescu, and R. Spohr, Nucl. Inst. Meth. Phys. Res. B **225**, 497 (2004).

[50] V. P. Menon and C. R. Martin, Anal. Chem. **67** (13), 1920 (1995).

[51] J. H. Mooij, Phys. Stat. Sol. A **17**, 521 (1973).

[52] A. Bid, A. Bora, and A. K. Raychaudhuri, Phys. Rev. B **74**, 035426 (2006).

[53] J. W. Moore, C. L. Stanitski, and P. C. Jurs, *Chemistry: The Molecular Science*, 2nd ed. (Thompson Brooks/Cole, Belmont, CA, 2005).

[54] A. F. Khan, M. Mehmood, A. M. Rana, and M. T. Bhatti, Appl. Surf. Sci. **225**, 8562 (2009).

[55] E. J. Park, S. W. Lee, I. C. Bang, and H. W. Park, Nanoscale Res. Lett **6**, 223 (2011).

[56] T. Dey, P. Khuntia, A. V. Mahajan, N. Kumar, and A. Sundaresan, Europhys. Lett. **96** (6), 67008 (2011).

[57] T. Krishnakumar, R. Jayaprakash, V. N. Singh, B. R. Mehta, and A. R. Phani, J. Nano Res. **4**, 91 (2008).

[58] N. P. Klochko, K. S. Klepikova, G. S. Khrypunov, O. V. Pirohov, and V. A. Novikov, Semi. Phys., Quant. Elec. & Optoelec. **17** (4), 358 (2014).

[59] J. D. Splett, D. F. Vechia, and L. F. Goodrich, J. Res. Natl. Inst. Stand. Technol. **116** (1), 489 (2011).

[60] A. M. Finkelshtein, Sov. Phys. JETP **57**, 97 (1983).

[61] D. M. Finlayson and P. J. Mason, J. Phys. C: Solid State Phys. **19**, L299 (1986).